Czech Technical University in Prague
Faculty of Nuclear Sciences and Physical Engineering

Dissertation

Numerical and machine learning methods for medical image processing

Prague 2022 Kateřina Škardová

This thesis is submitted to the Faculty of Nuclear Sciences and Physical Engineering, Czech Technical University in Prague, in partial fulfilment of the requirements for the degree of Doctor of Philosophy (Ph.D.) in Mathematical Engineering.

Bibliografický záznam

Autor	Ing. Kateřina Škardová, České vysoké učení technické v Praze, Fakulta jaderná a fyzikálně inženýrská, Katedra matematiky
Název práce	Numerické metody a metody strojového učeni pro zpracování obrazových medicinských dat
Studijní program	Aplikace přírodních věd
Studijní obor	Matematické inženýrství
Školitel	Doc. Ing. Tomáš Oberhuber, Ph.D., České vysoké učení technické v Praze, Fakulta jaderná a fyzikálně inženýrská, Katedra matematiky
Akademický rok	2022
Počet stran	114
Klíčová slova	registrace obrazu, optický tok, distanční funkce, korekce rozostření obrazu, odhad parametrů, strojové učení, MRI, Blochovy rovnice

Bibliographic Entry

Author	Ing. Kateřina Škardová, Czech Technical University in Prague, Faculty of Nuclear Sciences and Physical Engineering, Department of Mathematics
Title of dissertation	Numerical and machine learning methods for medical image processing
Degree programme	Application of Natural Sciences
Field of study	Mathematical Engineering
Supervisor	Doc. Ing. Tomáš Oberhuber, Ph.D., Czech Technical University in Prague, Faculty of Nuclear Sciences and Physical Engineering, Department of Mathematics
Academic year	2022
Number of pages	114
Keywords	image registration, optical flow, distance function, image deblurring, parameter estimation, machine learning, MRI, Bloch equations

Abstrakt

Tato práce se zabývá využitím matematických metod při zpracování medicínských obrazových dat. Je zde demonstrováno použití numerických metod i jejich kombinace s metodami strojového učení. Práce se zabývá třemi tématy – registrací obrazu, odstraňováním rozmazání obrazu a odhadem parametrů na základě obrazových dat.

V práci jsou popsány dva přístupy k registraci obrazu. Jeden z nich řeší problém registrace obrazů s proměnlivou intenzitou, druhý je vhodný pro další analýzu získaného deformačního pole. První metoda se používá k registraci snímků ze sekvence MOLLI. Výsledky jsou porovnány se standardní registrační metodou. Druhá metoda je použita ve dvou variantách – s využitím klasické podobnostní funkce založené na intenzitě a s využitím obrazového modelu. V první variantě je metoda použita pro registraci MRI snímků srdce a následný výpočet torze levé komory, druhá varianta je testována na syntetických tagovaných snímcích.

V další části práce je problém korekce rozostření obrazu formulován jako minimalizační problém s vazbou danou parciální diferenciální rovnicí. Je odvozen adjungovaný problém a je ukázáno, jak lze jeho řešení použít k řešení primárního minimalizačního problému.

Nakonec je popsána metoda odhadu parametrů tkáně na základě obrazových dat. Metoda je použita k odhadu relaxačního času T_1 z obrazových řad MOLLI. Je provedena studie na reálných datech MRI a výsledky jsou porovnány s existující metodou pro odhad T_1.

Abstract

This thesis deals with the use of mathematical methods in the medical image data processing. The use of numerical methods as well as their combination with machine learning methods is demonstrated. Three topics are addressed in the thesis – image registration, image deblurring, and parameter estimation based on image data.

The thesis describes two approaches to image registration. One of which addresses the problem of registering images with varying image intensity, and the other is suitable for further analysis of the acquired deformation field. The first method is used to register images from the MOLLI sequence. The results are compared with the standard registration method. The second method is used in two variants – using a classical intensity-based similarity function and an imaging model. In the first variant, the method is used for the registration of cardiac MRI images and subsequent calculation of the left ventricular torsion, the second variant is tested on synthetic tagged images.

Next, the problem of image deblurring is formulated as a PDE-constrained minimization problem. The adjoint problem is derived and it is shown, how its solution can be used to solve the primary minimization problem.

Finally, a method for tissue parameter estimation based on image data is described. The method is used to estimate the T_1 relaxation time from MOLLI image series. A study on real MRI data is performed and the results are compared with the existing method for T_1 estimation.

Acknowledgements

First of all, I would like to thank my supervisor Tomáš Oberhuber for his patience and constant support during my Ph.D. studies. I appreciated his vast knowledge of numerical mathematics and all the great ideas he kept coming up with to improve my work, even at times when we seemed to have reached a dead end in our research.

I am grateful to Radomír Chabiniok for providing invaluable medical background for my work. Thanks to him I understood that there should indeed always be a "relevant clinical question" at the beginning of any research project concerning the application of mathematics in medicine.

I would also like to express my gratitude to all the collaborators from the many departments – FNSPE, IKEM, Inria, École Polytechnique, and UT Southwestern Medical Center – who participated in the research projects I was involved in. I always appreciated the supportive working and learning environment they created for me as a starting researcher.

Finally, I would like to thank my family and especially my husband who supported me during my Ph.D. studies and never let me give up.

My work related to the topic of my thesis was supported by:

- Application of advanced supercomputing methods for mathematical modeling of natural processes, project of the Student Grant Agency of the Czech Technical University in Prague No. SGS17/194/OHK4/3T/14
- Development and application of advanced methods for mathematical modeling of natural and industrial processes using high-performance computing, project of the Student Grant Agency of the Czech Technical University in Prague No. SGS20/184/OHK4/3T/14
- Centre for Advanced Applied Sciences, project of The Ministry of Education, Youth and Sports of the Czech Republic under the OP RDE No. CZ2.11/0/0/16_019/0000778
- Research Center for Informatics, project of The Ministry of Education, Youth and Sports of the Czech Republic under the OP RDE CZ2.11/0/0/16_019/0000765
- Analysis of flow character and prediction of evolution in endovascular treated arteries by magnetic resonance imaging coupled with mathematical modeling, project of The Ministry of Health of the Czech Republic No. NV19-08-00071

Publications Related to the Thesis

Journal papers

- Škardová, K., Oberhuber, T., Tintěra, J., and Chabiniok, R. (2021). *Signed-distance function based non-rigid registration of image series with varying image intensity.* Discrete & Continuous Dynamical Systems - S, 14(3):1145–1160.

  – Chapter 2

- Castellanos, D. A., Škardová, K., Bhattaru, A., Berberoglu, E., Greil, G., Tandon, A., Dil- lenbeck, J., Burkhardt, B., Hussain, T., Genet, M., and Chabiniok, R. (2021). *Left ventricular torsion obtained using equilibrated warping in patients with repaired tetralogy of Fallot.* Pediatric Cardiology, 42(6):1275–1283.

  – Chapter 4

Conference papers

- Škardová, K., Rambausek, M., Chabiniok, R., and Genet, M. (2019). *Mechanical and imaging models-based image registration. In ECCOMAS Thematic Conference on Computational* Vision and Medical Image Processing, pages 77–85. Springer.

  – Chapter 3

Book chapters

- Chabiniok, R., Škardová, K., Galabov, R., Eichler, P., Gusseva, M., Janoušek, J., Fučík, R., Tintěra, J., Oberhuber, T., Hussain, T. (2021). *Translational Cardiovascular Modeling: Tetralogy of Fallot and Modeling of Diseases.* In Modeling Biomaterials (pp. 241-276). Birkhäuser, Cham.

Submitted publications

- Škardová, K., Galabov, R., Fricková, K., Pevný T., Tintěra, J., Oberhuber, T., Chabiniok, R., (2022). *Combining machine learning and mathematical modeling in estimation of T1 relaxation time from cardiac magnetic resonance imaging data.* Submitted to Heliyon.

  – Chapter 6

Author's declaration

I confirm having prepared the thesis on my own and having listed all used sources of information in the bibliography.

Prague, December 14 2022 Kateřina Škardová

Contents

Introduction 1

Incorporating mathematical models into real clinical applications provides an opportunity to address clinical problems that the currently available resources cannot adequately solve. Book chapter [15] presents some examples of mathematical models employed in the assessment and treatment of cardiovascular pathologies. The discussed methods include mathematical models of the heart with physiological and biophysical basis, simulations of flow in vessels, advanced acquisition and processing pipelines for clinical data, and creating personalized models by the means of model-data fusion. Ultimately, it is the process of translating patient-specific modeling into patient care that contribute to an accurate diagnosis or optimal clinical management.

1.1 The focus of thesis

This work revolves around medical image data processing. As will be explained in this chapter, in the field of medical image analysis, the notion of image processing encompasses a very broad class of problems. Most of the chapters focus on processing cardiac magnetic resonance imaging (MRI) data. Although some of the presented methods are problem-specific as they exploit very specific properties of a particular MRI sequence, others are directly applicable to other types of medical image data.

When referring to image processing in general, we usually consider tasks such as image registration, image enhancement, or pattern recognition. These tasks are not exclusive to medical image analysis and need to be handled in many domains of human activity. Four chapters of this work address these more classical types of image-processing tasks. Two approaches to image registration, designed for different types of image data, are presented in Chapters 2 and 3. In Chapter 4, an incorporation of existing image registration method into the procedure of extracting motion features is presented. The problem of image enhancement, specifically deblurring is addressed in Chapter 5. This chapter focuses on a mathematical formulation of the problem and derivation of its solution.

As mentioned above, in the field of medical imaging, image processing includes also a variety of tasks specific to this domain. In principle, the intensity of a voxel in a magnetic resonance (MR) image is determined by some characteristic of the imaged tissue. Therefore, MR can be used to non-invasively assess not only the shape, position, or motion of organs but also the properties of the tissue. Depending on the clinical question, suitable MR imaging sequence can be selected that encodes the relevant tissue parameter into the output image. The set of imaged properties can be as diverse as velocity, the amount of absorbed contrast agent, or time constants of magnetic resonance phenomena of the examined tissue. Determining a given tissue characteristic from image data can sometimes be straightforward. However, sometimes, it may be rather non-trivial.

The problem of estimating tissue parameters from image data can be viewed as an inverse problem of the underlying model. In mathematics, an inverse problem is a process of determining causal parameters that were used in a system to produce the set of given observations. The underlying model can describe, for instance, directly the imaging sequence (the model of physical phenomenon – nuclear magnetic resonance effect – in Chapter 6). In other applications, it may be the model of physiological process (e.g., properties of contracting heart as in Chapter 4) or model describing the flow in large vessels (e.g. submitted article [22]) or the microcirculation (submitted article [26]).

In our case, the imaging sequence plays the role of the system, and the images obtained using this sequence as the observations. In the example of the model of imaging sequence, the forward problem consists in generating a signal (image intensity) for a given set of tissue parameters, and the inverse problem in determining the parameters based on the observed signal:

$$\text{Tissue parameters} \xrightarrow{\text{Forward problem}} \text{Image intensity}$$
$$\text{Tissue parameters} \xleftarrow{\text{Inverse problem}} \text{Image intensity}$$

In order to mathematically solve either the direct or the inverse problem, a mathematical model of the system – in our case, the imaging sequence – is required. For more complex imaging sequence it can be challenging to balance the sufficient descriptiveness of the mathematical model and the number of free parameters that need to be optimized. In Chapter 6, we demonstrate an approach to this type of problem in the example T_1 relaxation time estimation based on image series acquired by a specific type of MR imaging sequence.

In the remaining part of this chapter, we provide deeper background to the two key topics of this, which where mentioned above – image registration and tissue parameter estimation.

1.2 Image registration

Image registration is one of the key image-processing tasks in medical imaging. It is defined as the process of determining the displacement between two images of the same object and removing this displacement to align the object. It is used to resolve misalignment caused by the movement of the imaged object during image acquisition, which may occur due to respiratory or cardiac movements of the patient. Alternatively, registration may be required when integrating image data acquired by different types of medical imaging techniques, the so-called multimodal images. In this case, the problem of different spatial resolutions and modalities of the images must also be addressed.

Registration of the image series is often the first step in any subsequent voxel-wise analysis. For example, when estimating a tissue parameter based on image series, i.e. when the parameter is a function of the time-dependent image intensity. An example of such a problem is the estimation of T_1 relaxation time from the MOLLI (Modified Look-Locker inversion recovery, [53]) image series, addressed in Chapter 2.

Sometimes, however, the target of the analysis may be the extraction of the motion. This is particularly relevant in cardiac magnetic resonance imaging, where the examination of cardiac motion patterns can be used for diagnostic or prognostic purposes. Several MR imaging techniques, such as cardiac MRI tagging and MRI cine sequences, were specifically designed for myocardial deformation analysis. The image registration method proposed specifically to track motion in the tagged MRI images is presented in Chapter 3. Compared with the global features of cardiac function such as ejection fraction, local features such as myocardial strain and torsion can provide information about dysfunction in a segment of the myocardium, even when the global features

are preserved within normal values. The use of image registration method in the task of torsion estimation is illustrated in Chapter 4.

Most classical image registration methods consist of defining a suitable measure of similarity between the two images and subsequently minimizing a loss function based on this similarity measure. One way in which registration methods can be divided is based on which parts of the images are taken into account when assessing the similarity between images [50, 56]. The similarity might be evaluated based on comparing properties of all voxels, sets of landmark points, contours, or surfaces. In the landmark based approach, the landmarks can be detected automatically or manually. In cardiac MRI images, this approach may be problematic, as there are usually only a few suitable anatomical landmarks and their accurate location may be difficult, especially in the case of multimodal image registration. In the contour-based methods, the similarity of images is evaluated based on the contours of objects detected in both images. In [20], the B-spline method was used to register segmented left ventricle contours. Finally, in the voxel-based methods, the similarity measure is defined based on the comparison of image properties in all voxels of the images. A classical example of such methods is the optical flow method. In [35], the similarity measure for the optical flow method was defined based on the comparison of image intensity and gradient orientation.

Selecting the image features used in the registration method is yet another important aspect in the definition of the suitable similarity measure. Some of the most basic features may be the image intensity and the gradient of the intensity. The appropriate choice is especially important when registering images obtained by different modalities. In such cases, the similarity cannot be evaluated based on the image intensity and more complex features must be used, such as in Chapter 2.

From a mathematical point of view, image registration is an ill-posed problem – there may be many displacement fields that would lead to the same result when applied to an image, but not all of them are admissible. Therefore, a variational approach is often used to formulate the problem of finding the optimal deformation field, and the image similarity term is complemented by regularization terms. The regularization should contain the additional conditions that the deformation field should satisfy in order to be feasible.

The basic regularization conditions usually enforce a reasonable magnitude of the displacements and smooth changes of displacements in adjacent voxels. More complex regularization conditions may involve knowledge of the physiological and physical properties of the object. Such added constraints will typically also affect the magnitude and smoothness of the displacements but in a more problem-specific manner. Finally, in some cases, the regularization terms may include prior knowledge about the expected type of deformation. Finding the optimal displacement field can then be reduced to finding the parameters of the considered type of transformation.

1.3 Tissue parameter estimation based on medical image data

Lately, both mathematical models and machine learning (ML) methods were used to estimate tissue parameters from a series of MRI images.

Mathematical models with a biophysical background may allow estimating material parameters representing the physical properties of the tissue (e.g. passive myocardial stiffness and contractility using cine or tagged MRI [1, 14, 32, 33, 39, 83], the density of microvessel network in the myocardium using perfusion MRI [17], Young's modulus or relative pressures using cine and phase-contrast MRI [5, 10, 21].

The estimation of the tissue parameters based on the measured data are often ill-posed. The character of the problem depends on the specific combination of mathematical model and measured data. In some cases, only 2D measurements are available, while the mathematical

model of the 3D system is used. Also, some quantities used as parameters in the model are not measured at all. Typically, the more complex the mathematical model, the higher are the risks of the measurements not containing an adequate amount of information. Therefore, succeeding in estimating parameters in such complex models may depend also on defining an initial guess for the parameters. Providing a sufficiently good initial guess may prevent the estimation procedure from finding local minima and also accelerate the computation-intensive numerical optimization. Obtaining such an initial estimate can be a difficult task in itself.

ML has recently been used in a number of tasks in medical image processing, such as image classification, registration, or segmentation. These ML methods are frequently based on Neural Networks (NN) and their variants, such as Convolutional Neural Networks (CNN). CNN was used for brain tumor segmentation in [60], a cascade of CNNs was used for image reconstruction from undersampled k-space measurements in [67]. [4] used an ensemble of several deep NNs trained on synthetic data for denoising contrast-enhanced MR images. Application of ML in the cardiovascular system was reviewed in [69] and book [51] provides an overview of current methods of computational modeling and artificial intelligence in cardiac applications. [55] used a method, which incorporated the knowledge of typical organ shape within CNN, for the segmentation of myocardium. [43] used ML for domain adaptation in a cohort of congenital heart diseases, to give some examples from this fast-growing research area.

It has been shown that ML methods can effectively 'learn' even complex systems when a large number of pairs of inputs and outputs for the system are provided. However, in the field of medical image analysis, obtaining such dataset may not always be possible. In addition to the fact that in some cases the data is simply not obtained in sufficient quantities, it can also be time expensive to assess the desired output or the so-called ground truth. Insufficient training dataset can cause overfitting, where the model prediction is overly fitted to a particular dataset. In those applications, where acquiring a sufficient amount of real samples would be technically impossible or very costly, data augmentation can be used. This technique expands the training dataset by synthetic data, which are created based on the original data, e.g. in the case of image data, by applying elastic deformations, blurring, or other modifications [76].

Alternatively, we can see this as an opportunity to combine both approaches. If the given system can be represented by a mathematical model, additional training data may be generated using the model itself [13]. As opposed to the augmentation of existing data, the mathematical model can be used to supplement also the outlying measurements. One more reason to consider combining both approaches is the potential to increase the interpretability and reliability of the results, as it is known that the actual physical or biological character of the system can become completely neglected when using the ML methods alone.

The presented challenges are addressed in Chapter 6 in the example of specific parameters estimation problem.

Signed-distance function based registration of images with varying image intensity

2

This chapter is based on work [77]:

Škardová, K., Oberhuber, T., Tintěra, J., and Chabiniok, R. (2021). **Signed-distance function based non-rigid registration of image series with varying image intensity**. Discrete & Continuous Dynamical Systems - S, 14(3):1145–1160.

2.1 The MOLLI image series

In this section, we describe the main features of the MOLLI image series and how these images are used to assess the T_1 relaxation time and extracellular volume fraction (ECV). We only focus on the aspects of the MOLLI image series, that addresses in the image registration method described in this chapter. More details of the MOLLI sequence and T_1 relaxation time are provided in Chapter 6.

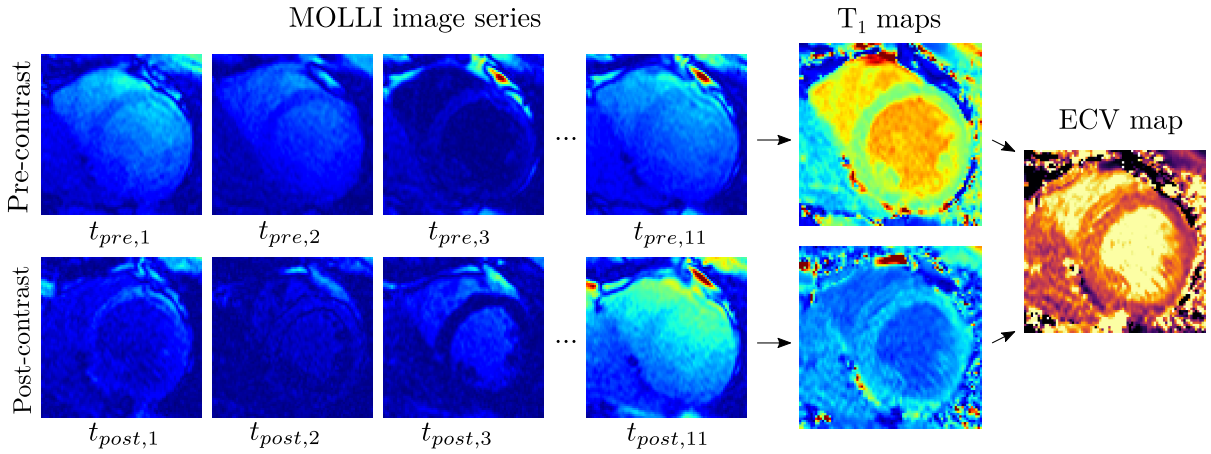

Figure 2.1: Diagram of obtaining the T_1 maps and subsequently the *ECV* map from the MOLLI image series.

The processing of the MOLLI image series is shown in Figure 2.1. We work with the MOLLI image series consisting of 11 images of myocardium acquired at different times. The images are

used to compute a map where the intensity of each pixel represents the T_1 relaxation time within the pixel. The computation is performed pixel-wise and therefore the myocardium needs to be in the same position in all images of the series.

In order to obtain ECV, the image series needs to be acquired before and after administering a contrast agent. The contrast agent affects the relaxation times and therefore we obtain two different T_1 maps. These two maps are subsequently compared to obtain a map where each pixel's intensity corresponds to the ECV. The ECV is computed using the following formula:

$$ECV = (1-h) \cdot \frac{\frac{1}{T_{1,post,myo}} - \frac{1}{T_{1,pre,myo}}}{\frac{1}{T_{1,post,blood}} - \frac{1}{T_{1,pre,blood}}},$$

where h denotes the hematocrit – a patient-specific constant that represents the cellular fraction of blood. In order to compare $T_{1,pre,myo}$ and $T_{1,post,myo}$ correctly in each point of the myocardium, the myocardium should be in the same position in both T_1 maps.

The diagram in Figure 2.1 also shows the main characteristics of the MOLLI image series – the changing image intensity. This feature of the images needs to be taken into consideration when registering them.

2.2 The proposed method

In this chapter, we address the problem introduced above – registration of two images of the same object with different image intensities acquired at different times. These images are referred to as source and target images. To deal with this property of the image data, we propose an image registration method based on representing the objects by their signed-distance functions. The principle of the method is shown in Figure 2.2.

In the first step, the object of interest – the myocardium – is segmented in both images. In the next step, the segmented objects are represented by their signed distance function (SDF). The SDF contains information about the position and shape of the myocardium but omits the original image intensities. Subsequently, the displacement field between the two SFDs is determined. This is done by estimating the optical flow $\boldsymbol{u}$. In the last step, the optical flow $\boldsymbol{u}$ is applied to the original source image. The myocardium in the resulting image should be aligned with the myocardium in the target image.

Each of the steps is described in detail in the following sections. First, the segmentation of the myocardium of described within Section 2.3. Namely, the level-set method used for detecting myocardium contours is described in Sections 2.3.1 and 2.3.2. Subsequently, the computation of the signed-distance function is described in Section 2.3.3. Finally, the representation of the myocardium, based on the detected contours, is described in Section 2.3.4

The optical flow method is introduced in Section 2.4. The numerical solution of the problem is described in Section 2.5. Finally, the experimental results and comparison of the proposed method with two other registration approaches are presented in Section 2.6.

2.3 Segmentation of the myocardium

In this work, the myocardium is segmented using the level-set method for the edge detection. The result of this method is a closed smooth curve corresponding with the myocardium edge. The outer (epicardial) and subsequently the inner (endocardial) edge of the myocardium is detected and the myocardium is then defined as the area between these two curves.

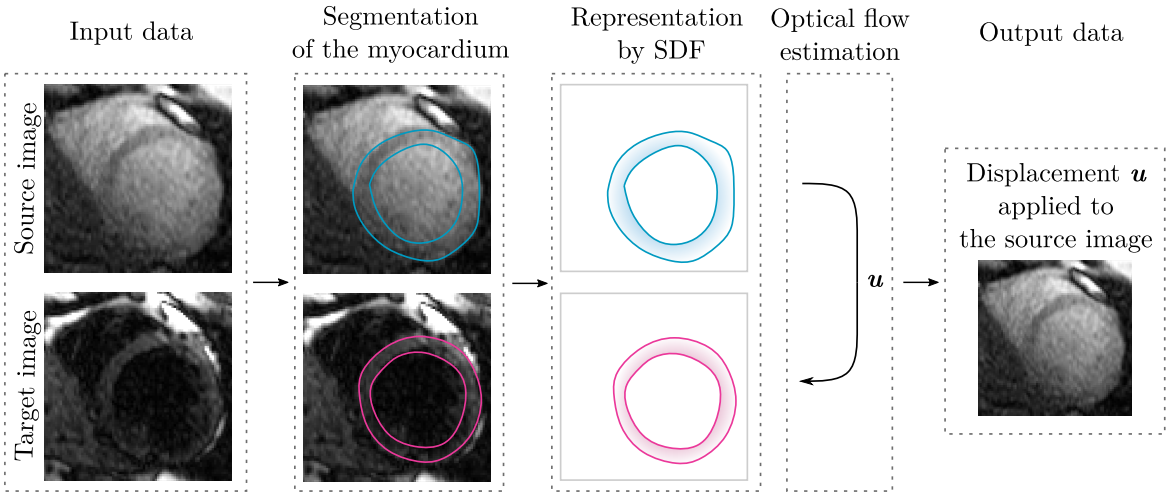

Figure 2.2: Principle of the proposed image registration method.

2.3.1 Mean-curvature driven motion of level sets

The level-set methods are based on implicit description of surfaces. In 2D domain Ω, we consider a dynamic simple closed curve $C(\theta)$, where θ denotes the time used to track the evolution of the curve. In the implicit description, C is viewed as a zero level set of a corresponding level-set function $\psi(\boldsymbol{x}, \theta)$, such that $\psi(\boldsymbol{x}, \theta) = 0$ for all $\boldsymbol{x}$ that lie on the curve C. That is $C(\theta) = \{\boldsymbol{x}$, such that $\tilde{\psi}(\boldsymbol{x}, \theta) = 0\}$ [57].

We assume that the level-set function takes positive values on the exterior of curve $C(\theta)$ – denoted as $C(\theta)_{ext}$ – and negative values in the interior – denoted as $C(\theta)_{int}$, i.e.:

$$\begin{aligned} \psi(\boldsymbol{x}, \theta) &= 0, \quad \forall \boldsymbol{x} \in C(\theta), \forall \theta \in [0, T^1_{fin}], \\ \psi(\boldsymbol{x}, \theta) &< 0, \quad \forall \boldsymbol{x} \in C(\theta)_{int}, \forall \theta \in [0, T^1_{fin}], \\ \psi(\boldsymbol{x}, \theta) &> 0, \quad \forall \boldsymbol{x} \in C(\theta)_{ext}, \forall \theta \in [0, T^1_{fin}], \end{aligned} \tag{2.1}$$

where $[0, T^1_{fin}]$ is the time interval in which the evolution takes place.

This representation may be convenient for multiple reasons. First, the position of any point $\boldsymbol{y}$ with respect to the curve C at a given time θ can be assessed by evaluating the sign of $\psi(\boldsymbol{y}, \theta)$. Further, the unit outer normal vector to the curve can be easily obtained as $\boldsymbol{n} = \nabla\psi / \|\nabla\psi\|$, assuming ψ is differentiable at a given point. Last but not least, no explicit handling is needed to keep track of the curve splitting and merging during its evolution in time. Let us now consider the task of edge detection using such implicitly described curve C.

Let us assume, the object whose boundary we want to detect lies inside the initial curve $C_{init}(\boldsymbol{x})$ represented by the level-set function $\psi_{init}(\boldsymbol{x})$. We may use $\psi_{init}(\boldsymbol{x})$ as an initial condition for the evolution of the curve, that is $\psi(\boldsymbol{x}, 0) = \psi_{init}(\boldsymbol{x})$. We aim for such evolution of ψ that adapts the contour C of the object.

The curve should therefore primarily move inward. If the curve moves in the direction of an inner normal vector with velocity $\boldsymbol{v} = -v\nabla\psi / \|\nabla\psi\|$, where v is the velocity magnitude, the following equation holds for the corresponding level set function [71]:

$$\frac{\partial \psi}{\partial \theta} - \|\nabla\psi\| v = 0 \quad \forall \boldsymbol{x} \in C(\theta), \forall \theta \in [0, T^1_{fin}]. \tag{2.2}$$

In this work, we use the so-called mean curvature flow – each point of the curve moves inward with a velocity proportional to the boundary mean curvature at that point. In the terms of

equation (2.2), such evolution is ensured by setting velocity magnitude v to a mean curvature of the curve C [23], i.e. $v = \nabla \cdot \left(\frac{\nabla\tilde{\psi}}{\|\nabla\tilde{\psi}\|}\right)$. By substituting for v in equation (2.2), the level-set formulation of the mean-curvature flow is obtained:

$$\frac{\partial\psi}{\partial\theta} - \|\nabla\psi\|\nabla \cdot \left(\frac{\nabla\psi}{\|\nabla\psi\|}\right) = 0 \quad \forall \boldsymbol{x} \in C(\theta), \forall\theta \in [0, T^1_{fin}]. \tag{2.3}$$

For the numerical stability and existence of solution at points with zero gradients of ψ , $\|\nabla\psi\|$ is regularized as $\|\nabla\tilde{\psi}\|_\epsilon = \sqrt{\epsilon^2 + \|\nabla\tilde{\psi}\|^2}$ [23, 62]. The final form of the equation reads:

$$\begin{aligned} \frac{\partial\psi}{\partial\theta} - \|\nabla\psi\|_\epsilon\nabla \cdot \left(\frac{\nabla\psi}{\|\nabla\tilde{\psi}\|_\epsilon}\right) = 0 \qquad & \text{on } \Omega \times (0, T^1_{fin}], \\ \psi(x,0) = \psi_0(x) \qquad & \text{on } \Omega, \\ \nabla\psi(\boldsymbol{x},\theta) \cdot \boldsymbol{n} = 0 \qquad & \text{on } \partial\Omega \times (0, T^1_{fin}]. \end{aligned} \tag{2.4}$$

2.3.2 Edge detection using mean-curvature flow

In this section, we discuss, how the mean-curvature-driven evolution of curve C, described by equation (2.2) can be modified for the purpose of edge detection. In image processing, edges are typically characterized by a significant change of the image intensity.

Let us represent the image by image intensity function $I : \Omega \to \mathbf{R}$, where Ω denotes the image domain. Sudden changes in image intensity can then be identified based on the norm of the image function gradient. In order to adapt the curve C to the edge of the object, its mean-curvature-driven evolution (described by (2.3)) should stop when it approaches a point with a large gradient of the image function I. For this, equation (2.3) is modified in the following way [11]:

$$\begin{aligned} \frac{\partial\psi}{\partial\theta} = \|\nabla\psi\|_\epsilon g_0 \nabla\left(\frac{\nabla\psi}{\|\nabla\psi\|_\epsilon}\right) + \nabla\psi \cdot \nabla g_0 \qquad & \text{on } \Omega \times (0, T^2_{fin}], \\ \psi(x,0) = \psi_0(x) \qquad & \text{on } \Omega, \\ \nabla\psi \cdot \boldsymbol{n} = 0 \qquad & \text{on } \partial\Omega \times (0, T^2_{fin}], \end{aligned} \tag{2.5}$$

where function $g_0 = g_0(\|\nabla I\|)$ tends to zero for growing values of the image gradient norm. We use the function:

$$g_0(\|\nabla I\|) = 1/(1 + K\|\nabla I\|^2), \tag{2.6}$$

as proposed in [61]. The function g_0 controls the sensitivity to variations of image intensity by the parameter K.

The second added term $\nabla\psi \cdot \nabla g_0$, i.e. derivative of ψ in direction of ∇g_0, has a corrective effect in the evolution of the curve. The diagram in Figure 2.3 shows an illustrative curve C and an object, whose edge is to be detected, but it is not fully inside the curve. In the case of point $\boldsymbol{b}$, the additional term $\nabla\psi \cdot \nabla g_0$ will take on negative value and therefore contribute to getting point $\boldsymbol{b}$ inside curve C. In the case of point $\boldsymbol{a}$, the term $\nabla\psi \cdot \nabla g_0$ will take on positive value and therefore reinforce the movement of curve C in the inward direction towards the edge of the object. We note, that this only holds for points sufficiently close to the edge of the object and curve C.

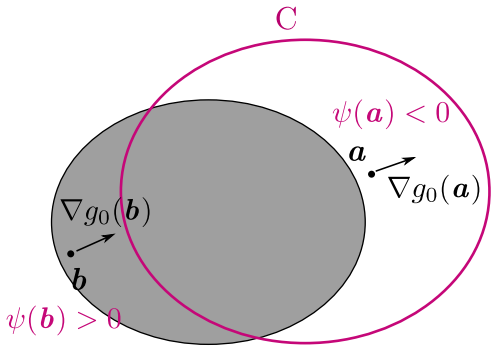

Figure 2.3: The diagram of the direction of ∇g_0 in the point $\boldsymbol{b}$ inside the object and point $\boldsymbol{a}$ outside the object whose edge is to be detected by curve C.

2.3.3 Signed-distance function

Level-set functions, obtained as a result of the level-set equation for the edge detection (2.5), represent the detected contour of the myocardium. This representation is however not suitable for the subsequent processing, as one contour might be represented by several level-set functions.

Therefore, we construct function ϕ, which has the same zero level set and additionally has the properties of the signed-distance function (i.e. $\|\nabla\phi(\boldsymbol{x})\| = 1$). Only one signed-distance function exists for each detected contour and therefore it is a representation suitable for comparing the contours. Function $\tilde{\phi}$ with the characteristics described above is obtained by solving the following equation [70]:

$$\begin{aligned} \frac{\partial\phi}{\partial\theta} &= S(\psi)\,(1 - \|\nabla\phi\|) && \text{on } \Omega \times (0, T^3_{fin}], \\ \phi(x, 0) &= \psi(x) && \text{on } \Omega, \\ \nabla\phi \cdot \boldsymbol{n} &= 0 && \text{on } \partial\Omega \times (0, T^3_{fin}], \end{aligned} \tag{2.7}$$

where function S is defined as smoothed sign function $S(\psi) = \psi/\sqrt{\psi^2 + \varepsilon^2}$. We note that the original level-set function $\psi(\boldsymbol{x})$ function serves as the initial estimate to evaluate the smoothed sign function S.

The shape representation by the signed-distance function is convenient as it distributes the information about contour C into the whole area Ω and thus enables the use of the optical flow registration method.

2.3.4 Representation of the myocardium

As mentioned above, equation (2.5) is solved twice in order to detect both contours of the myocardium. We assume that the position of the initial curve for the outer edge segmentation is provided by the user, as well as the value of constant K and the estimation of myocardium thickness d_{myo}.

First, equation (2.5) is solved for the outer (endocardial) edge detection. The detected curve C_{endo} is represented by the zero level set of function $\psi_{endo}(\boldsymbol{x}) = \psi(\boldsymbol{x}, T^2_{fin,endo})$. To acquire unique representation by SDF, equation (2.7) is solved with initial condition $\psi_{endo}(\boldsymbol{x})$. As a result, the signed distance function $\phi_{endo}(\boldsymbol{x}) = \phi(\boldsymbol{x}, T^3_{fin,endo})$ is obtained.

Second, equation (2.5) is solved for the inner (epicardial) contour detection. The initial condition is determined based on $\phi_{endo}(\boldsymbol{x})$. The zero level set is moved inward by the estimated myocardium thickness: $\psi_0(\boldsymbol{x}) = \phi_{endo}(\boldsymbol{x}) + d_{myo}$. The detected curve C_{epi} is then represented by the zero level set of function $\psi_{epi}(\boldsymbol{x}) = \psi(\boldsymbol{x}, T^2_{fin,epi})$. Subsequently, the signed distance function $\phi_{epi}(\boldsymbol{x}) = \phi(\boldsymbol{x}, T^3_{fin,epi})$ is obtained as a solution of (2.7), solved with initial condition $\psi_{epi}(\boldsymbol{x})$. Finally, the two contours are combined in a single level-set representation of the myocardium:

$$\psi_{myo}(\boldsymbol{x}) = \begin{cases} -\phi_{epi}(\boldsymbol{x}) & \text{for } \boldsymbol{x} : \phi_{epi}(\boldsymbol{x}) < 0, \\ \phi_{endo}(\boldsymbol{x}) & \text{for } \boldsymbol{x} : \phi_{epi}(\boldsymbol{x}) \geq 0. \end{cases} \tag{2.8}$$

The resulting level-set function $\psi_{myo}(\boldsymbol{x})$ takes on negative inside the myocardium and positive values outside the myocardium, as illustrated in simplified Figure 2.4.

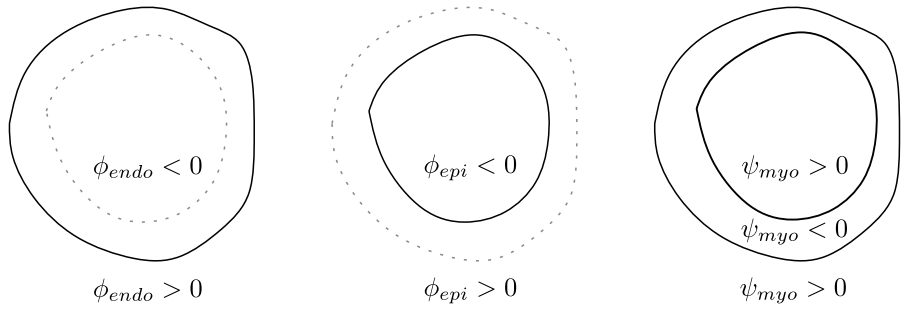

Figure 2.4: Representation of the myocardium by a single level-set function ψ_{myo}.

The final representation $\phi_{myo}(\boldsymbol{x}) = \phi(\boldsymbol{x}, T^3_{fin,myo})$ is obtained by solving equation (2.7) with initial condition $\psi_{myo}(\boldsymbol{x})$.

2.4 Optical flow based registration

Optical flow [38] is a vector field capturing the displacements occurring in the images of the same scene taken at times t and $t + \Delta t$. Let us represent the input image series by a time-dependent image function $I : \Omega \times T \to \mathbb{R}$, where T represents the time interval during which the images were taken and Ω is the spatial domain of the image.

For such image series represented by I, the optical flow is defined as a vector field $\boldsymbol{u}(\boldsymbol{x}, t) = (u_1(\boldsymbol{x}, t), u_2(\boldsymbol{x}, t), t)$, where $u_i(\boldsymbol{x}, t) : \Omega \times T \to \mathbb{R},\ i \in \{1, 2\}$ denote the displacements in directions of axes x and y, respectively.

To determine the optical flow, a rule for finding the correspondence between the points on images taken at time t and $t + \Delta t$ is needed. In most optical flow-determining algorithms, the correspondence is found based on a constancy assumption, which states that a certain value remains unchanged in time. The assumption frequently used for a single-modality registration is the *brightness constancy assumption*, according to which the intensity of each point remains the same in all images of the given series, i.e.:

$$I(x(t), y(t), t) = D, \quad \forall \boldsymbol{x} \in \Omega, \forall t \in T. \tag{2.9}$$

In the proposed method, the optical flow is applied to the series of signed-distance functions to avoid the problem with varying image intensities. Let us assume the SDF $\phi_{myo}(\boldsymbol{x})$ representing the myocardium is constructed in a way described in Section 2.3.4 in each frame of the input

image series. This way we obtain time dependent signed-distance function $\phi_{myo}(\boldsymbol{x}, t)$. From this point on, the index that links the SDF to the myocardium is dropped, and the SDF will be denoted by $\phi(\boldsymbol{x}, t)$

The constancy assumption is applied to the signed-distance function $\phi(x, t)$ the same way as it was applied to the image function $I(\boldsymbol{x}, t)$ in (2.9):

$$\phi(x(t), y(t), t) = D, \quad \forall \boldsymbol{x} \in \Omega, \forall t \in T. \tag{2.10}$$

Given how the function $\phi(x, t)$ is defined, the equation (2.10) states, that distance of any given point from the contours of the myocardium remains constant in time.

When registering the images within the MOLLI image series, we should be aware that the images are not chronologically ordered, as discussed in detail in Chapter 6. Therefore, the image series can be divided into two-image subsequences, each containing the target and source image, without loss of any information. Further, the time dimension is neglected and $\Delta t = 1$ is used in each subsequence, for simplicity.

As a derivative of equation (2.10), we obtain:

$$\frac{\mathrm{d}\phi}{\mathrm{d}t} = \frac{\partial \phi}{\partial x} u_1 + \frac{\partial \phi}{\partial y} u_2 + \frac{\partial \phi}{\partial t} = 0, \quad \forall \boldsymbol{x} \in \Omega, \tag{2.11}$$

where u_1 and u_2 denote x- and y-component of the displacements.

Equation (2.11) is not solved directly. Instead, we apply a more convenient variational approach, which allows for the incorporation of regularisation terms. We reformulate the requirements stated on the vector field $\boldsymbol{u}$ in (2.11) as a minimization problem:

$$\min_{\boldsymbol{u}} \int_{\Omega} \left(\frac{\partial \phi}{\partial x} u_1 + \frac{\partial \phi}{\partial y} u_2 + \frac{\partial \phi}{\partial t} \right)^2 \mathrm{d}\boldsymbol{x}. \tag{2.12}$$

We proceed to define the regularisation terms: the assumption of smoothness and the assumption of minimal magnitude. These two assumptions, together with the constancy assumption, force the zero displacements into the areas with the constant values function ϕ. The final functional has the following form:

$$E(u_1, u_2) = \alpha \underbrace{\int_{\Omega} \left(\frac{\partial \phi}{\partial x} u_1 + \frac{\partial \phi}{\partial y} u_2 + \frac{\partial \phi}{\partial t} \right)^2 \mathrm{d}\boldsymbol{x}}_{E_{constancy}} + \beta \underbrace{\int_{\Omega} q\left(\|\nabla u_1\|^2 + \|\nabla u_2\|^2 \right) \mathrm{d}\boldsymbol{x}}_{E_{smoothness}} + \gamma \underbrace{\int_{\Omega} \|\boldsymbol{u}\| \ \mathrm{d}\boldsymbol{x}}_{E_{magnitude}}, \tag{2.13}$$

where $q\left(\|\nabla u_1\|^2 + \|\nabla u_2\|^2 \right) = \sqrt{\epsilon + \|\nabla u_1\|^2 + \|\nabla u_2\|^2}$. The terms of functional (2.13) will be referred to as $E_{constancy}$, $E_{smoothness}$ and $E_{magnitude}$, respectively.

The domain of functional $E(u_1, u_2)$ is $W = W^{1,2}(\Omega) \times W^{1,2}(\Omega)$, where $W^{1,2}(\Omega)$ is the Sobolev space $W^{1,2}(\Omega) = \{u | u, D_x u, D_y u \in L^2(\Omega)\}$ [40]. The functions minimizing functional E on its domain are denoted as (u_1^*, u_2^*).

Functional $E(u_1, u_2)$ is convex and therefore satisfies the equation

$$\mathrm{d}E((u_1^*, u_2^*); (\theta_1, \theta_2)) = 0, \quad \forall (\theta_1, \theta_2) \in W, \tag{2.14}$$

where $\mathrm{d}E(u_1^*, u_2^*)$ is the Fréchet derivative of the functional E at the point (u_1^*, u_2^*) [63]. Equation (2.14) is the necessary and sufficient condition for the functions (u_1^*, u_2^*) to be minimizers of the functional $E(u_1, u_2)$[63].

Using the *fundamental lemma of calculus of variations* [28] it can be proven that the minimizing functions (u_1^*, u_2^*) have to satisfy the following set of equations:

$$\alpha\left(\frac{\partial\phi}{\partial x}u_1^* + \frac{\partial\phi}{\partial y}u_2^* + \frac{\partial\phi}{\partial t}\right)\frac{\partial\phi}{\partial x} - \beta\nabla\cdot\left(q'(\|\nabla u_1^*\|^2 + \|\nabla u_2^*\|^2)\nabla u_1^*\right) + \gamma u_1^* = 0, \quad \forall \boldsymbol{x}\in\Omega, \tag{2.15}$$
$$\alpha\left(\frac{\partial\phi}{\partial x}u_1^* + \frac{\partial\phi}{\partial y}u_2^* + \frac{\partial\phi}{\partial t}\right)\frac{\partial\phi}{\partial y} - \beta\nabla\cdot\left(q'(\|\nabla u_1^*\|^2 + \|\nabla u_2^*\|^2)\nabla u_2^*\right) + \gamma u_2^* = 0, \quad \forall \boldsymbol{x}\in\Omega.$$

The nonlinear set of equations (2.15) is solved using the method of steepest descent. The following set of partial differential equations is obtained:

$$\begin{aligned}
\frac{\partial u_1}{\partial\theta} =& -\alpha\left(\frac{\partial\phi}{\partial x}u_1 + \frac{\partial\phi}{\partial y}u_2 + \frac{\partial\phi}{\partial t}\right)\frac{\partial\phi}{\partial x} + \\
& \beta\nabla\cdot\left(q'(\|\nabla u_1\|^2 + \|\nabla u_2\|^2)\nabla u_1\right) - \gamma u_1 && \text{on } \Omega\times(0, T_{fin}^4], \\
\frac{\partial u_2}{\partial\theta} =& -\alpha\left(\frac{\partial\phi}{\partial x}u_1 + \frac{\partial\phi}{\partial y}u_2 + \frac{\partial\phi}{\partial t}\right)\frac{\partial\phi}{\partial y} + \\
& \beta\nabla\cdot\left(q'(\|\nabla u_1\|^2 + \|\nabla u_2\|^2)\nabla u_2\right) - \gamma u_2 && \text{on } \Omega\times(0, T_{fin}^4], \\
u_i|_{\theta=0} =& \; u_{i,0} && \text{on } \Omega,\ i = 1,2 \\
u_i =& \; 0 && \text{on } \partial\Omega\times(0, T_{fin}^4],\ i = 1,2.
\end{aligned} \tag{2.16}$$

2.5 Numerical solution

2.5.1 Spatial discretization

The complementary finite volume method described in [34, 42] is used for spatial discretization. The digital image can be considered as a grid of pixels denoted by V:

$$V = \{(ih,(i+1)h)\times(jh,(j+1)h) \mid i = 0,..,N_1-1, j = 0,..,N_2-1\}, \tag{2.17}$$

where $h = 1/\max(N_1, N_2)$ is the spatial step. The individual volume elements of set V are denoted by $V_{i,j} = (ih,(i+1)h)\times(jh,(j+1)h)$. The centers of volume elements $V_{i,j}$ are denoted by $x_{i,j} = \left[\left(\frac{1}{2}+i\right)h, \left(\frac{1}{2}+j\right)h\right]$. The edges of $V_{i,j}$ are denoted $E_{i,j}^1, E_{i,j}^2, E_{i,j}^3, E_{i,j}^4$. The set of volume elements, the central points, and edges are shown in Figure 2.5.

The functions, defined on domain Ω are approximated by grid functions. The grid function is constant on each element $V_{i,j}$. The function value of the grid function at given element $V_{i,j}$ is denoted by subscript i,j. No new notation is introduced for the grid functions to simplify the following formulas. I.e. if the notation $\psi_{i,j}$ refers to the function value of the grid function approximating the original function ψ at point $x_{i,j}$.

2.5.2 Edge detection

Partial differential equations (2.5) is solved using the method of lines. First, the spatial derivatives are discretized. The resulting set of ordinary differential equations (ODEs) are solved by the explicit Euler scheme until reaching a steady state, the specific criteria are provided in Section 2.6.

Let us now derive the discretization of the spatial derivatives. Equation (2.5) is first integrated over a fixed volume $V_{i,j}$:

$$\int_{V_{i,j}}\frac{\partial\psi}{\partial\theta}\mathrm{d}\boldsymbol{x} = \int_{V_{i,j}}\nabla\psi\cdot\nabla g_0\mathrm{d}\boldsymbol{x} + \int_{V_{i,j}}\|\nabla\psi\|_\epsilon g_0\nabla\left(\frac{\nabla\psi}{\|\nabla\psi\|_\epsilon}\right)\mathrm{d}\boldsymbol{x}. \tag{2.18}$$

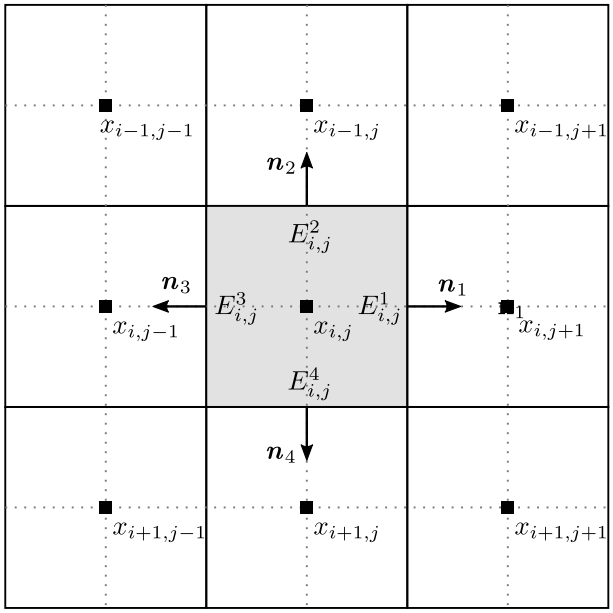

Figure 2.5: Diagram of section of the grid V.

The left-hand side of equation (2.18) is approximated using the value of grid function $\psi_{i,j}$:

$$\int\limits_{V_{i,j}} \frac{\partial \psi}{\partial \theta} \mathrm{d}\boldsymbol{x} \approx h^2 \frac{d\psi_{i,j}}{d\theta} \tag{2.19}$$

The first term on the right-hand side of equation (2.18) is first approximated in similar way:

$$\int\limits_{V_{i,j}} \nabla\psi \cdot \nabla g_0 \mathrm{d}\boldsymbol{x} \approx h^2 \left(\nabla\psi \cdot \nabla g_0\right)\big|_{x_{i,j}} \tag{2.20}$$

Expression $\left(\nabla\psi \cdot \nabla g_0\right)\big|_{x_{i,j}}$ is discretized using the first-order upwind scheme:

$$\left(\frac{\partial\psi}{\partial x}\frac{\partial g_0}{\partial x}\right)\Big|_{x_{i,j}} \approx \begin{cases} \frac{g_{0,i+1,j}-g_{0,i-1,j}}{2h}\,\frac{\psi_{i+1,j}-\psi_{i,j}}{h}, & \text{if } \frac{g_{0,i+1,j}-g_{0,i-1,j}}{2h} > 0, \\ \frac{g_{0,i+1,j}-g_{0,i-1,j}}{2h}\,\frac{\psi_{i,j}-\psi_{i-1,h}}{h}, & \text{if } \frac{g_{0,i+1,j}-g_{0,i-1,j}}{2h} < 0. \end{cases}$$

The derivatives with respect to y are treated analogically. The term $\left(\nabla\psi \cdot \nabla g_0\right)\big|_{x_{i,j}}$ discretized using this formula will be denoted $D_{0,i,j}$.

The second term on the right-hand side is discretized using the schemes described in [42]. The term is approximated and divided into three parts $P_{1,i,j}, P_{2,i,j}, P_{3,i,j}$:

$$\int\limits_{V_{i,j}} \|\nabla\psi\|_\epsilon g_0 \nabla\left(\frac{\nabla\psi}{\|\nabla\psi\|_\epsilon}\right)\mathrm{d}\boldsymbol{x} \approx \underbrace{\|\nabla\psi\|_\epsilon\big|_{V_{i,j}}}_{P_{1,i,j}} \underbrace{\frac{1}{1+K\,\|\nabla I\|_\epsilon\big|_{V_{i,j}}}}_{P_{2,i,j}} \underbrace{\int\limits_{V_{i,j}} \nabla\left(\frac{\nabla\psi}{|\nabla\psi\|_\epsilon}\right)\mathrm{d}\boldsymbol{x}}_{P_{3,i,j}}.$$

Notation $|\nabla\psi|_\epsilon\big|_{V_{i,j}}$ and $\|\nabla I\|_\epsilon\big|_{V_{i,j}}$, respectively, is used to approximate the values of function $\|\nabla\psi\|_\epsilon$ and $\|\nabla I\|_\epsilon$ in the volume element $V_{i,j}$. Similar notation will be used to approximate the value on the edges $E^1_{i,j}, E^2_{i,j}, E^3_{i,j}, E^4_{i,j}$.

The terms $P_{1,i,j}, P_{2,i,j}$ are discretized as:

$$P_{1,i,j} \approx \sqrt{\epsilon^2 + \frac{1}{4}\left[\left(\|\nabla\psi\|_{E^1_{i,j}}\right)^2 + \left(\|\nabla\psi\|_{E^2_{i,j}}\right)^2 + \left(\|\nabla\psi\|_{E^3_{i,j}}\right)^2 + \left(\|\nabla\psi\|_{E^4_{i,j}}\right)^2\right]},$$

$$P_{2,i,j} \approx \frac{1}{1 + K\sqrt{\epsilon^2 + \frac{1}{4}\left[\left(\|\nabla I\|_{E^1_{i,j}}\right)^2 + \left(\|\nabla I\|_{E^2_{i,j}}\right)^2 + \left(\|\nabla I\|_{E^3_{i,j}}\right)^2 + \left(\|\nabla I\|_{E^4_{i,j}}\right)^2\right]}},$$

where $\|\nabla\psi\|_\epsilon|_{E^k_{i,j}}$ and $\|\nabla\psi\|_\epsilon|_{E^k_{i,j}}$, for $k = 1, \ldots, 4$, are evaluated as:

$$\|\nabla\psi\|_\epsilon|_{E^k_{i,j}} = \sqrt{\left(\frac{\partial\psi}{\partial x}\right)^2\Big|_{E^k_{i,j}} + \left(\frac{\partial\psi}{\partial y}\right)^2\Big|_{E^k_{i,j}}} \tag{2.21}$$

and

$$\|\nabla I\|_\epsilon|_{E^k_{i,j}} = \sqrt{\left(\frac{\partial I}{\partial x}\right)^2\Big|_{E^k_{i,j}} + \left(\frac{\partial I}{\partial y}\right)^2\Big|_{E^k_{i,j}}}. \tag{2.22}$$

the discretization of partial derivatives of ψ and I on the edges will be described later in this section.

The discretization of the third term $P_{3,i,j}$ will be shown on a more general term

$$\tilde{P}_{3,i,j} = \int\limits_{V_{i,j}} \nabla \cdot (g(\psi)\nabla\psi)\,\mathrm{d}\boldsymbol{x}, \tag{2.23}$$

as this approach is used also for the discretizations in differential equations (2.16). In the case of term $P_{3,i,j}$, the function has the form of $g(\psi) = 1/\|\nabla\psi\|_\epsilon$.

First, the Green's formula is applied to $\tilde{P}_3$:

$$\tilde{P}_{3,i,j} = \int\limits_{V_{i,j}} \nabla \cdot (g(\psi)\nabla\psi)\,\mathrm{d}\boldsymbol{x} = \int\limits_{S_{i,j}} g(\psi)\nabla\psi \cdot \boldsymbol{n}\mathrm{d}S,$$

where $\boldsymbol{n}$ denotes the outer unit normal vector to the edge $S_{i,j}$ of the volume $V_{i,j}$. The boundary $S_{i,j}$ consists of four edges $E^1_{i,j}, E^2_{i,j}, E^3_{i,j}, E^4_{i,j}$ as can be seen in Figure 2.5. We substitute the values of normal vectors to the edges:

$$\begin{aligned}
&\int\limits_{S_{i,j}} g(\psi)\nabla\psi \cdot \boldsymbol{n}\mathrm{d}S = \sum_{k=1}^{4} \int\limits_{E^k_{i,j}} g(\psi)\nabla\psi \cdot \boldsymbol{n}\mathrm{d}S = \int\limits_{E^1_{i,j}} [g(\psi)\nabla\psi]|_{E^1_{i,j}} \cdot (1,0)\mathrm{d}S + \\
&\int\limits_{E^2_{i,j}} [g(\psi)\nabla\psi]|_{E^2_{i,j}} \cdot (0,-1)\mathrm{d}S + \int\limits_{E^3_{i,j}} [g(\psi)\nabla\psi]|_{E^3_{i,j}} \cdot (-1,0)\mathrm{d}S + \int\limits_{E^4_{i,j}} [g(\psi)\nabla\psi]|_{E^4_{i,j}} \cdot (0,1)\mathrm{d}S \\
&= \int\limits_{E^1_{i,j}} g(\psi)|_{E^1_{i,j}} \left.\frac{\partial\psi}{\partial x}\right|_{E^1_{i,j}} \mathrm{d}S - \int\limits_{E^2_{i,j}} g(\psi)|_{E^2_{i,j}} \left.\frac{\partial\psi}{\partial y}\right|_{E^2_{i,j}} \mathrm{d}S - \int\limits_{E^3_{i,j}} g(\psi)|_{E^3_{i,j}} \left.\frac{\partial\psi}{\partial x}\right|_{E^3_{i,j}} \mathrm{d}S \\
&\quad + \int\limits_{E^4_{i,j}} g(\psi)|_{E^4_{i,j}} \left.\frac{\partial\psi}{\partial y}\right|_{E^4_{i,j}} \mathrm{d}S.
\end{aligned}$$

Let us now define how the derivatives of general function f at the edges $E^1_{i,j}, E^2_{i,j}, E^3_{i,j}, E^4_{i,j}$ are discretized. We assume function f is defined on the grid V and therefore can be approximated by the corresponding grid function with function values denoted by $f_{i,j}$. The discretization is following:

$$\begin{aligned}
\left.\frac{\partial f}{\partial x}\right|_{E^1_{i,j}} &\approx \frac{f_{i+1,j} - f_{i,j}}{h},\\
\left.\frac{\partial f}{\partial y}\right|_{E^1_{i,j}} &\approx \frac{f_{i,j+1} + f_{i+1,j+1} - f_{i,j-1} - f_{i+1,j-1}}{4h},\\
\left.\frac{\partial f}{\partial x}\right|_{E^2_{i,j}} &\approx \frac{f_{i+1,j} + f_{i+1,j-1} - f_{i-1,j} - f_{i-1,j-1}}{4h},\\
\left.\frac{\partial f}{\partial y}\right|_{E^2_{i,j}} &\approx \frac{f_{i,j} - f_{i,j-1}}{h},\\
\left.\frac{\partial f}{\partial x}\right|_{E^3_{i,j}} &\approx \frac{f_{i,j} - f_{i-1,j}}{h},\\
\left.\frac{\partial f}{\partial y}\right|_{E^3_{i,j}} &\approx \frac{f_{i-1,j+1} + f_{i,j+1} - f_{i-1,j-1} - f_{i,j-1}}{4h},\\
\left.\frac{\partial f}{\partial x}\right|_{E^4_{i,j}} &\approx \frac{f_{i+1,j} + f_{i+1,j+1} - f_{i-1,j} - f_{i-1,j+1}}{4h},\\
\left.\frac{\partial f}{\partial y}\right|_{E^4_{i,j}} &\approx \frac{f_{i,j+1} - f_{i,j}}{h}.
\end{aligned}$$

These formulas are used to replace all derivatives at the edges to finish the discretization of terms $P_{1,i,j}, P_{2,i,j}, P_{3,i,j}$. Let us denote the fully discretized right hand side by $D_{i,j}(\psi_{i,j})$.

The equation 2.18 fully discretized in space reads:

$$h^2 \frac{\mathrm{d}\psi_{i,j}}{\mathrm{d}\theta} = D_{i,j}(\psi_{i,j}). \tag{2.24}$$

This presented process could be repeated for all non-boundary volumes of the grid V, resulting in set ODEs:

$$h^2 \frac{\mathrm{d}\psi_{i,j}}{\mathrm{d}\theta} = D_{i,j}(\psi_{i,j}), \quad \text{for } i = 1 \dots N_1 - 2, j = 1, \dots, N_2 - 2. \tag{2.25}$$

The set of ODEs is solved using explicit Euler scheme. The time is discretized using a time step h_t. We denote the value of $\psi_{i,j}$ in time $\theta = 0$ by $\psi^0_{i,j}$. Similarly, the value of $\psi_{i,j}$ in discrete time nh_t is denoted by $\psi^n_{i,j}$. The derivative on the left hand side is then discretized using following finite difference:

$$h^2 \left(\frac{\mathrm{d}\psi_{i,j}}{\mathrm{d}\theta}\right)\bigg|_{\theta = nh_t} \approx h^2 \frac{\psi^n_{i,j} - \psi^{n-1}_{i,j}}{h_t} \tag{2.26}$$

Finally, when discretizing the initial and boundary conditions of PDE (2.5), we obtain a set

of equations:

$$
\begin{aligned}
h^2 \frac{\psi_{i,j}^n - \psi_{i,j}^{n-1}}{h_t} &= D_{i,j}(\psi_{i,j}^n) && \text{for } i = 1 \dots N_1 - 2,\ j = 1, \dots, N_2 - 2,\ n = 1, \dots, N_t, \quad (2.27)\\
\psi_{i,j}^0 &= \psi_{0,i,j} && \text{for } i = 1 \dots N_1 - 2,\ j = 1, \dots, N_2 - 2,\\
\psi_{0,j}^n &= \psi_{1,j}^n && \text{for } j = 1, \dots, N_2 - 2,\ n = 1, \dots, N_t,\\
\psi_{N_1-1,j}^n &= \psi_{N_1-2,j}^n && \text{for } j = 1, \dots, N_2 - 2,\ n = 1, \dots, N_t,\\
\psi_{i,0}^n &= \psi_{i,1}^n && \text{for } i = 1, \dots, N_1 - 2,\ n = 1, \dots, N_t,\\
\psi_{i,N_2-1}^n &= \psi_{i,N_2-2}^n && \text{for } i = 1 \dots, N_1 - 2,\ n = 1, \dots, N_t,
\end{aligned}
$$

where N_t is the number of time steps needed to reach the convergence.

2.5.3 Signed-distance function

The partial differential equation (2.7) was solved numerically by the method of lines. The spatial derivatives are discretized in the first step. Second, the resulting set ODEs are solved by the explicit Euler scheme. Godunov scheme [59] is used for the discretization of the right hand side. First, we define two version of discretization of term $\|\nabla\phi\|$:

$$
\begin{aligned}
\|\nabla\phi\|_{i,j}^+ = \Bigg(&\left(\max\left\{\max\left\{\frac{\phi_{i,j} - \phi_{i-1,j}}{h}, 0\right\}, \min\left\{\frac{\phi_{i+1,j} - \phi_{i,j}}{h}, 0\right\}\right\}\right)^2 +\\
&\left(\max\left\{\max\left\{\frac{\phi_{i,j} - \phi_{i,j-1}}{h}, 0\right\}, \min\left\{\frac{\phi_{i,j+1} - \phi_{i,j}}{h}, 0\right\}\right\}\right)^2\Bigg)^{1/2}\\
\|\nabla\phi\|_{i,j}^- = \Bigg(&\left(\max\left\{\max\left\{\frac{\phi_{i+1,j} - \phi_{i,j}}{h}, 0\right\}, \min\left\{\frac{\phi_{i,j} - \phi_{i-1,j}}{h}, 0\right\}\right\}\right)^2 +\\
&\left(\max\left\{\max\left\{\frac{\phi_{i,j+1} - \phi_{i,j}}{h}, 0\right\}, \min\left\{\frac{\phi_{i,j} - \phi_{i,j-1}}{h}, 0\right\}\right\}\right)^2\Bigg)^{1/2}
\end{aligned}
$$

Then, the right hand side is discretized in a following way:

$$
S(\psi)\,(1 - \|\nabla\phi\|) \approx \begin{cases} S(\psi_{i,j})\left(\|\nabla\phi\|_{i,j}^+ - 1\right) & \text{for } S(\psi_{i,j}) > 0,\\ S(\psi_{i,j})\left(\|\nabla\phi\|_{i,j}^- - 1\right) & \text{for } S(\psi_{i,j}) < 0. \end{cases} = G_{i,j}(\psi_{i,j}) \qquad (2.28)
$$

We remind, that $S(\psi) = \psi/\sqrt{\psi^2 + \epsilon}$ and therefore $S(\psi_{i,j}) = \psi_{i,j}/\sqrt{{\psi_{i,j}}^2 + \epsilon}$. Analogical equation can be derived for all non-boundary nodes $x_{i,j}$ of the grid V, resulting in following set of ODEs:

$$
\frac{\partial\phi_{i,j}}{\partial\theta} = G_{i,j}(\phi_{i,j}), \quad \text{for } i = 1, \dots, N_1 - 2,\ j = 1, \dots, N_2 - 2. \qquad (2.29)
$$

The ODEs are solved using Euler scheme, leading to set of equations analogical with (2.27).

2.5.4 Determining of the optical flow

The set of PDEs (2.16) is also solved using the method of lines. First, the spatial derivatives are discretized and the resulting system of ordinary differential equation is then solved by the explicit Euler scheme.

In this section, the discretization of spatial derivatives is described for one of the equations, the process would be analogical for the other one. The differential equation is first integrated over a fixed volume $V_{i,j}$:

$$\int_{V_{i,j}} \frac{\partial u_1}{\partial \theta} \mathrm{d}\boldsymbol{x} = -\alpha \underbrace{\int_{V_{i,j}} \left(\frac{\partial \phi}{\partial x} u_1 + \frac{\partial \phi}{\partial y} u_2 \mathrm{d}\boldsymbol{x} + \frac{\partial \phi}{\partial t} \right) \frac{\partial \phi}{\partial x}}_{O_{1,i,j}} + \underbrace{\beta \int_{V_{i,j}} \nabla \cdot \left(q'(\|\nabla u_1\|^2 + \|\nabla u_2\|^2) \nabla u_1 \right) \mathrm{d}\boldsymbol{x}}_{O_{2,i,j}} - \underbrace{\gamma \int_{V_{i,j}} u_1 \, \mathrm{d}\boldsymbol{x}}_{O_{3,i,j}}. \tag{2.30}$$

The left-hand side is approximated by

$$\int_{V_{i,j}} \frac{\partial u_1}{\partial \theta} \mathrm{d}\boldsymbol{x} \approx h^2 \frac{\mathrm{d}u_{1,i,j}}{\mathrm{d}\theta}. \tag{2.31}$$

The first term $O_{1,i,j}$ is discretized as:

$$O_{1,i,j} \approx h^2 \left(\frac{\phi_{i+1,j} - \phi_{i,j}}{h} u_{1,i,j} + \frac{\phi_{i,j+1} - \phi_{i,j}}{h} u_{2,i,j} + \phi^T_{i,j} - \phi_{i,j} \right) \frac{\phi_{i,j} - \phi_{i-1,j}}{h} \tag{2.32}$$

The second term $O_{2,i,j}$ has the same form as the term $\tilde{P}_{3,i,j}$ (2.23) and it is discretized in the same way. The remaining term $O_{3,i,j}$ is discretized as:

$$O_{3,i,j} \approx h^2 u_{1,i,j}. \tag{2.33}$$

When denoting the spatially discretized right hand side of equation (2.30) by $H_{i,j}(\phi_{i,j})$, the following set of ODEs can be derived for all non-boundary elements $V_{i,j}$:

$$h^2 \frac{\mathrm{d}u_{1,i,j}}{\mathrm{d}\theta} = H_{i,j}(\phi_{i,j}) \quad \text{for } i = 1, \ldots, N_1 - 2, \; j = 1, \ldots, N_2 - 2. \tag{2.34}$$

The ODEs are solved using Euler scheme, leading to set of equations analogical with (2.27).

2.6 Experimental results

At the beginning of this section, we introduce the parameters and stopping criteria for equations discretized in the previous section, the notation used in this section, and the functions used to evaluate the results of registration.

Then, we present the results of the proposed method applied to synthetic images and images from real MOLLI series. The results are compared with the mutual information maximization method [49], for which the version described in [65] and implemented in MIRTK library[1] was used.

2.6.1 Parameters of the discretization and criteria of convergence

In the numerical solution of the level-set equation for edge detection (described in 2.5.2), the time is discretized with a time step $h_t = 2.0 \cdot 10^{-6}$. The condition $\|\psi^{n+1} - \psi^n\|_2 / \|\psi^n\|_2 < 5 \cdot 10^{-4}$ was used as a stopping criterion for edge-detection equation.

[1] `https://mirtk.github.io/sidebar.html`

In the computation of the signed distance function (described in 2.3.3), the time is discretized with a time step $h_t = 1.0 \cdot 10^{-4}$. The distance function was evaluated only in the surrounding of the zero level set. Therefore, based on [2], it is not necessary to solve the equation until reaching the steady state. In order to get the correct solution in the 10-pixel-wide neighborhood of the zero level set, it was sufficient to set $T^4_{fin} = 10h$.

In the numerical solution of the optical flow equation (described in Section 2.5.4), the initial conditions $u_{1,0}, u_{2,0}$ are set to uniform value $0.1h$, where h is the spatial discretization step. The time is discretized with a time step $h_t = 7.0 \cdot 10^{-8}$. The stopping condition was used in the form $\left(\|u_1^{n+1} - u_1^n\|_2 + \|u_2^{n+1} - u_2^n\|_2\right) / \left(\|u_1^n\|_2 + \|u_2^n\|_2\right) \quad < 0.002$.

The equation used for image denoising is not solved until a steady state to avoid "over-smoothing" of the image, hence T_{fin} was set to $6 \cdot 10^{-5}$.

The value of regularization $\epsilon = 10^{-4}$ was used.

2.6.2 Terminology and evaluation of results

Mutual information

Mutual information is a widely used metrics for comparing multimodality medical images. In the following section, the normalized mutual information will be used to evaluate the difference between the images with varying intensity. Before its definition, we introduce the following notations. Let $P(i)$ denotes the probability of intensity i being present in image I with the range of discrete intensities $i \in \{0, 1, .., i_{\max}\}$. For two images I, J, $P(i, j)$ denotes the joint probability of intensities i, j being present at the same position in both images I and J. These probabilities are computed as a number of pixels with given characteristics, divided by the total number of pixels.

The normalized mutual information is defined as: $MI(I, J) = (H(I) + H(J))/H(I, J)$, where $H(I) = -\sum_{i=0}^{i_{\max}} P(i)\ln(P(i))$ denotes the marginal entropy of given image and $H(I, J) = -\sum_{i,j=0}^{i_{\max}} P(i, j)\ln(P(i, j))$ denotes the joint entropy of two images.

Evaluation of results

To evaluate the difference between two functions f_1, f_2 defined on the numerical grid V we use norm $\| \phi_1 - \phi_2\|_{h,2} = h^2 \left(\sum_{i=1,j=1}^{N_1,N_2} \left(\phi_1(x_{i,j}) - \phi_2(x_{i,j})\right)^2\right)^{\frac{1}{2}}$, where h is the spatial discretization step of the given grid.

Notations

In the section of experimental results, the target image is denoted as T, the source image by S, and the signed-distance functions of the target and source objects by ϕ_T and ϕ_S, respectively. The source image registered by the given method is denoted by S_{method}, the registered signed-distance function of the source object by $\phi_{S,method}$. The compared methods include: optical flow applied to signed-distance functions (OF^{dist}), mutual information maximization method applied to the original images (MIM), and to the signed-distance functions (MIM^{dist}).

2.6.3 Synthetic images with single object

Two binary synthetic images of one fully visible object with dimensions $N_1 = 200, N_2 = 200$ are shown in Figures 2.6a and 2.6b. Due to the simplicity of the scene, the segmentation was done by thresholding. The OF^{dist} method was applied to the signed-distance functions, as described in the previous sections. To provide a relevant comparison, the mutual information maximization

method was applied to both – the original images and o the signed-distance functions (i.e. methods MIM and MIM^{dist}).

The absolute value of the difference between the target and source images before registration can be seen in Figure 2.6c. The differences after registration by OF^{dist}, MIM, and MIM^{dist} are shown in the second line of Figure 2.6. As can be seen in Table 2.1, the best result was obtained by the MIM method applied to the original images. The replacement of images by the distance functions of the object of interest does not provide any advantage in this simple case.

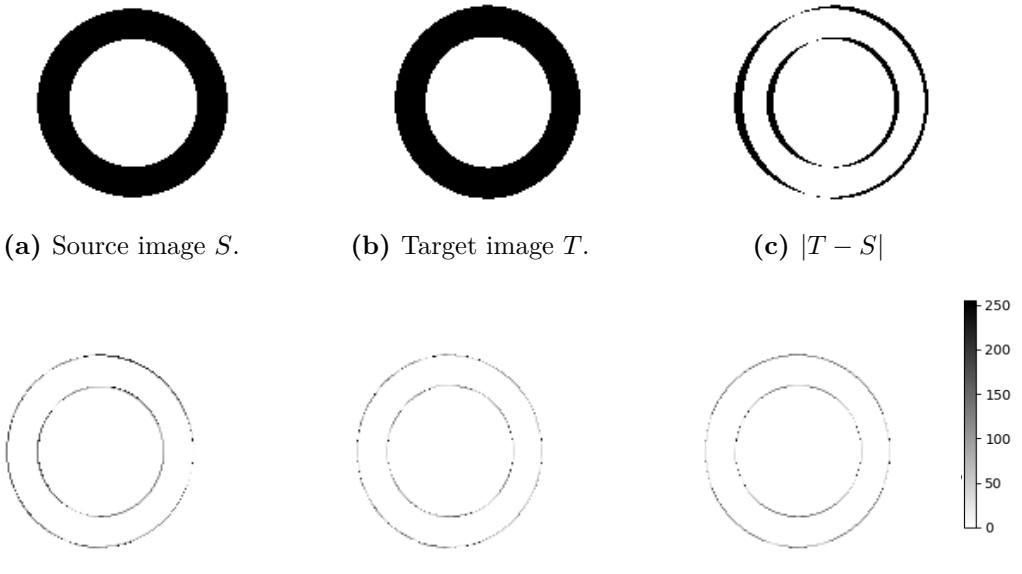

(a) Source image S. **(b)** Target image T. **(c)** $|T - S|$

(d) $|T - S_{OF^{dist}}|$. **(e)** $|T - S_{MIM}|$. **(f)** $|T - S_{MIM^{dist}}|$.

Figure 2.6: Source image (a), target image (b), the absolute value of their difference before registration (c) and after registration by OF^{dist}, MIM and MIM^{dist} (d-f). Parameters used in the determination of the optical flow (2.13):$\alpha = 1.0, \beta = 3.25, \gamma = 2.5$.

$\|T - S\|_{h,2}$	$\|T - S_{OF^{dist}}\|_{h,2}$	$\|T - S_{MIM}\|_{h,2}$	$\|T - S_{MIM^{dist}}\|_{h,2}$
0.2365	0.0782	0.0543	0.0651

Table 2.1: Norms of difference between the target 2.6b image and source image 2.6a before and after registration by OF^{dist}, MIM and MIM^{dist}.

2.6.4 Synthetic images with two objects

Next, we present binary synthetic images of two fully visible objects with dimensions $N_1 = 200, N_2 = 200$. The source and target images are shown in Figures 2.7a and 2.7b, respectively. The absolute value of the difference between the target and source images before registration can be seen in Figure 2.7c.

2.6.5 Registration of both objects

First, both objects were registered by OF^{dist}, MIM, and MIM^{dist}. The differences between the source and target image after registration are presented in the second line of Figure 2.7.

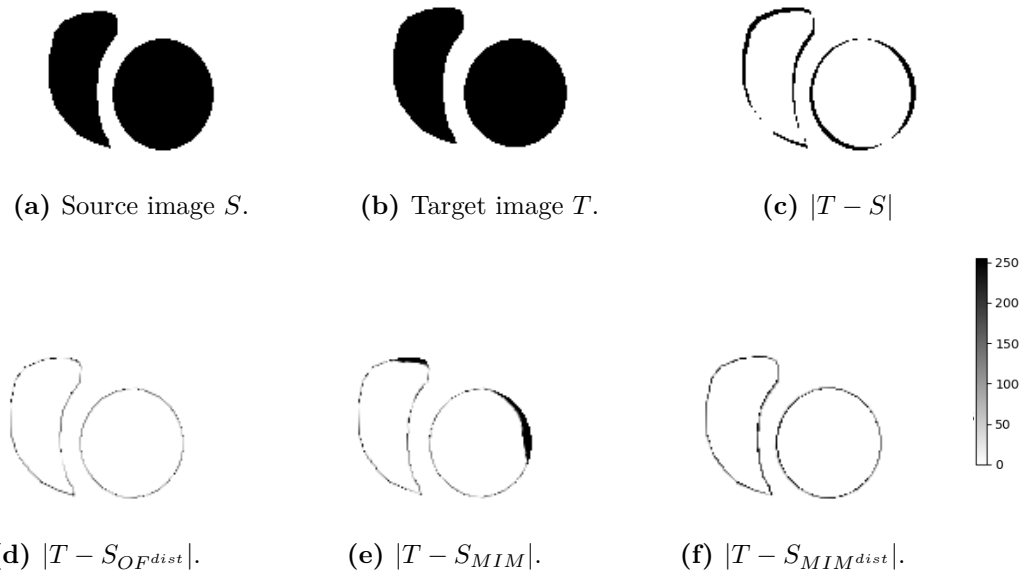

(a) Source image S. **(b)** Target image T. **(c)** $|T - S|$

(d) $|T - S_{OF^{dist}}|$. **(e)** $|T - S_{MIM}|$. **(f)** $|T - S_{MIM^{dist}}|$.

Figure 2.7: Source image (a), target image (b) and the absolute value of their difference before (c) and after registration by OF, MIM, and MIM^{dist} (d-f). Parameters used in the determination of the optical flow (2.13): $\alpha = 1.5, \beta = 3.75, \gamma = 3.25$.

The direct application of MIM is not suitable in this case, as can be seen in Figure 2.7e. Much better results were obtained by the MIM^{dist} method, which uses the signed-distance functions. However, as the values in Table 2.2 show, the smallest error was obtained by OF^{dist}. In Figure 2.8 the difference between OF^{dist} and MIM^{dist} approach is well visible. Applying MIM^{dist} decreases the error uniformly throughout the whole image (Figure 2.8b), while OF^{dist} (Figure 2.8b) creates unevenly distributed error. Table 2.3 quantifies these errors and shows that OF^{dist} performed best. Similar results could be expected for similar images.

$\|T - S\|_{h,2}$	$\|T - S_{OF^{dist}}\|_{h,2}$	$\|T - S_{MIM}\|_{h,2}$	$\|T - S_{MIM^{dist}}\|_{h,2}$
0.1663	0.0549	0.1030	0.0901

Table 2.2: Norms of difference between the target image in Figure 2.7b image and source image in Figure 2.7a before and after registration by OF^{dist}, MIM and MIM^{dist}.

$\|\phi_T - \phi_S\|_{h,2}$	$\|\phi_T - \phi_{S,OF^{dist}}\|_{h,2}$	$\|\phi_T - \phi_{S,MIM^{dist}}\|_{h,2}$
$21.247{\cdot}10^{-6}$	$5.984{\cdot}10^{-6}$	$7.375{\cdot}10^{-6}$

Table 2.3: Norms of difference between target and source signed-distance function before and after registration by OF^{dist} and MIM^{dist}. The source and target objects can be seen in Figure 2.7a and 2.7b, respectively.

2.6.6 Registration of one object

In this experiment, one object was segmented (marked by a green line in Figure 2.9a) and registered by OF^{dist}, while MIM was applied directly on the images in order to provide global

(a) $|\phi_T$ - $\phi_S|$. **(b)** $|\phi_T$ - $\phi_{S,OF^{dist}}|$. **(c)** $|\phi_T$ - $\phi_{S,MIM^{dist}}|$.

Figure 2.8: Absolute value of the difference between the target and source signed-distance function before and after registration by OF^{dist} and MIM^{dist}. The signed-distance functions are computed on a 10-pixel-wide neighborhood of the edges of the object and set to constant outside the neighborhood.

registration. The results can be seen in Figures 2.9b and 2.9c, respectively. The global registration by MIM provides a smaller global error, as can be seen in Table 2.4. However, the local registration by OF^{dist} (denoted by $S_{1,OF^{dist}}$) provides a smaller error in the object of interest as can be seen in Figure 2.9.

(a) The segmented object.

(b) $|T - S_{OF^{dist}}|$. **(c)** $|T - S_{MIM}|$.

Figure 2.9: The results of OF^{dist} registration of object marked by green line in 2.9a, and global MIM registration of the whole scene.

$\|T - S\|_{h,2}$	$\|T - S_{1,OF^{dist}}\|_{h,2}$	$\|T - S_{MIM}\|_{h,2}$
0.1663	0.1265	0.1030

Table 2.4: Norms of difference between the target image 2.7b and source image 2.7a before registration, after registration of one object by OF^{dist}, and after global registration by MIM.

2.6.7 Results MOLLI images

In this section, we present a comparison of the three registration approaches on real MRI MOLLI data. A set of three images with segmented myocardium marked by the green contour is presented in Figure 2.10. The dimensions of the images are $N_1 = 256, N_2 = 218$. In this case, the segmentation was done by the level-set method described in Section 2.5.2. The initial circle around the segmented object was provided by the user. The initial level-set function with properties given by (2.1) was then computed as $\psi_0(x_{i,j}) = \|x_{i,j} - s\| - r$, where s is the center of the circle and r is the radius. The values of parameter K, which governs the sensitivity of edge detection in equation (2.5), are provided in the caption of Figure 2.10.

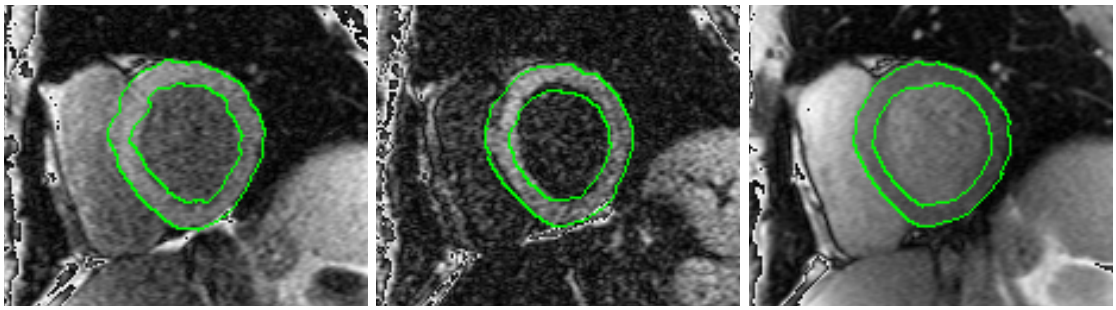

(a) Source image S_1. **(b)** Source image S_2. **(c)** Target image T.

Figure 2.10: Images from the MOLLI sequence with segmented myocardium. Values of parameter K (2.6), used for the outer edge detection in images S_1, S_2, T are: $K_{S_1} = 1.3 \cdot 10^{-6}$, $K_{S_2} = 1.3 \cdot 10^{-6}$, $K_T = 2.3 \cdot 10^{-6}$. Values of the parameter used for the inner edge detection: $K_{S_1} = K_{S_2} = K_T = 9.0 \cdot 10^{-6}$.

The images were registered by OF^{dist}, MIM, and MIM^{dist}. The results of all these approaches are presented in Figure 2.11.

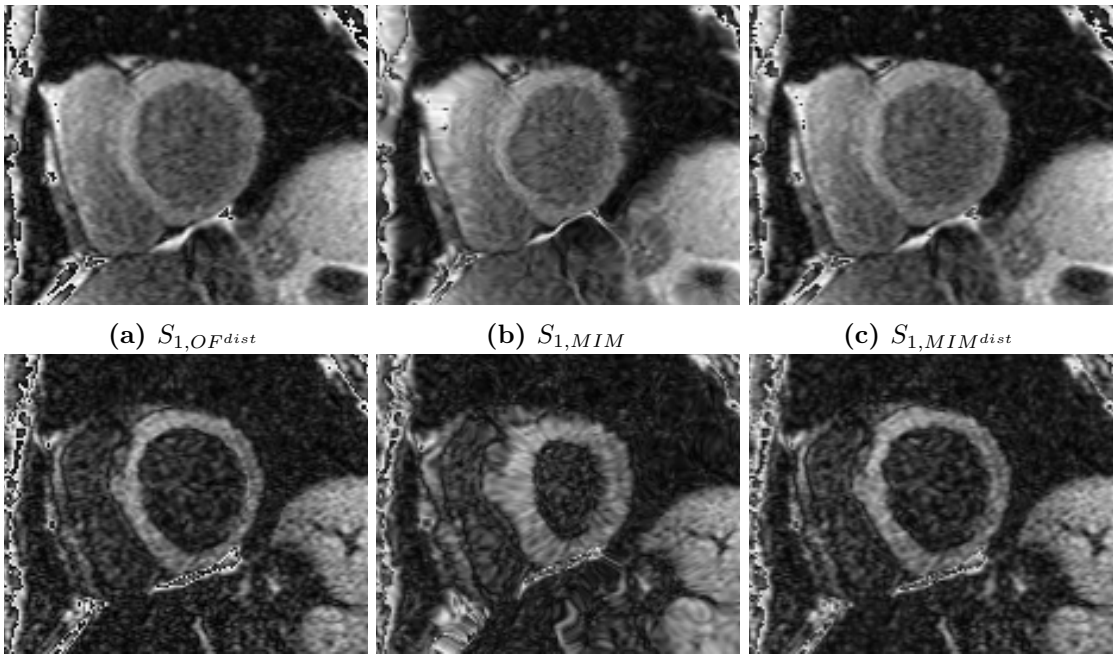

(a) $S_{1,OF^{dist}}$ **(b)** $S_{1,MIM}$ **(c)** $S_{1,MIM^{dist}}$

(d) $S_{2,OF^{dist}}$ **(e)** $S_{2,MIM}$ **(f)** $S_{2,MIM^{dist}}$

Figure 2.11: Results of registration of S_1, S_2 with target image T. Parameters used in the determination of the optical flow (2.13): $\alpha = 1.25, \beta = 3.5, \gamma = 3.0$.

MI measure was used to compare all three registration approaches. The *MI* was computed only in 10-pixels-wide surroundings of the edge of the segmented object. The values of *MI* are presented in Table 2.5.

The largest increase in *MI* was obtained by the direct application of MIM on the source and target images. However, the transformation led to an unrealistic deformation of the myocardium, as can be seen especially in Figure 2.11e. The results obtained by OF^{dist} and MIM^{dist} are visually comparable. The unrealistic deformation of the myocardium is avoided when using the signed-distance function (see Figures 2.11d and 2.11f), while the value of mutual information is

i	$MI(T, S_i)$	$MI(T, S_{i,OF^{dist}})$	$MI(T, S_{i,MIM})$	$MI(T, S_{i,MIM^{dist}})$
1	1.1556	1.2184	1.2273	1.2170
2	1.1012	1.2034	1.2052	1.1964

Table 2.5: *MI* of target image and source images from Figure 2.11 before and after registration by OF^{dist} and MIM and MIM^{dist}.

higher. The largest increase of mutual information was obtained by the OF^{dist} method.

2.7 Application for calculation of ECV

The proposed method for image registration is used in a application for the computation of ECV available at `https://mmg.fjfi.cvut.cz/mmg-medical-tools/`. In the application, the ECV map is computed based on the pre- and post-contrast T_1 maps and two representative images from the pre- and post-contrast MOLLI image series. The representative images are used to determine the displacement field using the presented method. The displacement is then used to register the T_1 maps. Finally, ECV map is computed based on the registered maps.

2.8 Conclusions

In this chapter, we presented a new approach to the registration of medical images with varying image intensity. We were specifically interested in the MOLLI image series, in which the changes in intensity and contrast make the registration challenging. The proposed registration method consists of the segmentation of the object of interest by level set method, its representation by a signed-distance function, and determining optical flow based on these functions.

The proposed method (OF^{dist}) was compared with two traditional registration methods based on the maximization of mutual information: either applied to the original images (MIM) or to the signed-distance function (MIM^{dist}). The experiments on synthetic binary images with one or two objects and on real images of the MOLLI cardiac MRI sequence were presented. The segmentation of the object of interest provided no advantage in the case of one binary object. It was however proven to be beneficial in other tested cases, i.e. synthetic images with two objects of interest or the images of real MOLLI sequence, where both OF^{dist} and MIM^{dist} provided better results than MIM. In particular, in the experiments on real MOLLI images, the MIM provided the largest increase in mutual information by prioritizing the registration of more distinct objects in the scene. This, however, led to unrealistic deformation of the myocardium, which was then avoided by using OF^{dist} and MIM^{dist}. Based on the experiments, it can be concluded, that the proposed segmentation-based registration using the signed-distance function provides better results when registering the objects of interest which are not the most distinct in the scene.

Personal contribution

The author contributed to the design of the image registration method. The author was responsible for the implementation of all the methods, the computation of experimental results, and for including the MIRTK library, which allowed the comparison with a standard method based on mutual information.

Mechanical and imaging models in image registration 3

In this chapter, we deal with image registration from a different perspective, than in Chapter 2. The image registration has two outputs – the aligned images and the deformation field. In Chapter 2, the goal was obtaining the aligned images. The emphasis was on designing an image similarity metric that would account for the evolving image intensity in the MOLLI image series. In some cases, however, it is the obtained deformation field that is the object of interest or the input for subsequent analysis. Especially in this type of application, it is often advisable to pay more attention to the regularization requirements in order to avoid non-physiological deformations. This can be achieved by incorporating more complex mechanical and image models into the image registration method. One such example is given in this chapter. The method was described in [78]:

Škardová, K., Rambausek, M., Chabiniok, R., and Genet, M. (2019). **Mechanical and imaging models-based image registration**. In ECCOMAS Thematic Conference on Computational Vision and Medical Image Processing, pages 77–85. Springer.

3.1 Introduction

Although new model-free machine learning-based approaches are now beginning to provide robust and accurate results [64], extracting motion from images is still most commonly based on combining analysis of the images intensity and a model of the underlying deformation as an initial guess or regularizer [80].

In this chapter, we focus on avoiding the dependence on image intensity analysis. As demonstrated in the previous chapter on the example of the MOLLI image series, building rules for correspondence between two points in an image based on their intensity can be too restrictive. However, complications can also arise in applications where the image intensity remains essentially unchanged. Primarily, any artifact in the source image can drastically deteriorate the result of the registration. In MRI, these artifacts may occur due to a local decrease in signal-to-noise ratio, local signal void, or partial volume effect, which is caused by the boundary between two different tissue types passing through a region corresponding to one voxel in the final image. These issues, intrinsic to the intensity-based approach, can be limited by geometrical or mechanical regularization. The additional regularization may, however, in turn, distort the deformation field. For instance, radial strains are systematically underestimated in 3D tagging cardiac images [29, 80].

In this chapter, we introduce a novel approach to extracting motion from medical image series, based on a model of the imaging modality. This approach is, to a large extent, independent of the type of image – the only pre-requisite is to be able to generate a realistic image associated with a given shape of the considered object, i.e., having an imaging model at hand.

The goal of this chapter is to propose an image registration that incorporates a model of tagged magnetic resonance images. The application of the method is illustrated with examples of synthetically created tagged images.

3.2 The problem setting

Let us assume I_0 and I are two images of the object $\mathcal{B}$, acquired at times t_0 and t. In the scope of this chapter, the position of $\mathcal{B}$ in I_0 will be referred to as a reference configuration, and the position in I as a deformed configuration. We define image functions I and I_0:

$$\begin{aligned} I_0 &: \Omega_0 \to \mathbb{R}, \\ I &: \Omega \to \mathbb{R}, \end{aligned} \tag{3.1}$$

The position of the material point in the reference and deformed configuration is denoted $\boldsymbol{X}$ and $\boldsymbol{x}$, respectively. I.e. image function I_0 assigns intensity to points $\boldsymbol{X}$ of image domain Ω_0 at time t_0 and I assigns intensity to points $\boldsymbol{x}$ in the domain Ω at time t. Domains Ω_0, Ω are in most cases identical.

The domains occupied by the object $\mathcal{B}$ at times t_0 and t are denoted $\Pi_0 \subset \Omega_0$ and $\Pi \subset \Omega$, respectively. The goal of the image registration problem is to find mapping Φ between the position of the material points in the reference and deformed domain:

$$\Phi : \Pi_0 \to \Pi. \tag{3.2}$$

It means that mapping Φ transforms the coordinates of a given point from the reference to the deformed configuration: $\Phi(\boldsymbol{X}) = \boldsymbol{x}$.

In the following formulation, we will work with the mapping Φ, however, we can alternatively define smooth deformation field U instead:

$$U : \Pi_0 \to \mathbb{R}^3, \tag{3.3}$$

The relation between Φ and U is $\boldsymbol{x} = \Phi(\boldsymbol{X}) = \boldsymbol{X} + U(\boldsymbol{X})$.

Because of the ill-posedness of the problem, finding the optimal mapping Φ^* is formulated as a minimization problem:

$$\Phi^* = \arg\min_{\Phi} E_{similarity}(\Phi), \tag{3.4}$$

where $E_{similarity}$ is the image similarity metric. In the image-intensity based methods, $E_{similarity}$ typically has the following form:

$$E^{image}_{similarity}(\Phi) = \frac{1}{2} \int_{\Pi_0} \left(I(\Phi(\boldsymbol{X})) - I_0(\boldsymbol{X})\right)^2 \mathrm{d}\boldsymbol{X}. \tag{3.5}$$

In general, the functional $E_{similarity}$ may not be quadratic but is assumed to be convex.

We note that the integration in (3.5) is performed over the reference domain Π_0, where $\boldsymbol{X}$ is the position of a given point in the reference configuration and $\Phi(\boldsymbol{X}) = \boldsymbol{x}$ is the position of the same point in the deformed configuration. As was mentioned in the introduction to this chapter, this approach has drawbacks that arise from the fact that the image intensity values are directly compared and, therefore, any artifacts in the images may distort the resulting value of the similarity metric. Therefore, an alternative metric is proposed in the following section.

3.3 Incorporation of imaging and mechanical model

In this section, we first define the imaging model. To goal is to use this mode to design a functional $E_{similarity}(\Phi)$ alternative to $E^{image}_{similarity}(\Phi)$ given by (3.5). We will present the model for tagged MRI images [3], but we note that it could be used for other types of images.

3.3.1 Model of tagged MRI images

The tagged MRI images refer to images obtained using the SPAMM (Spatial Modulation of Magnetization) technique [3]. In this paper, the imaging technique is described only to the extent necessary to understand the construction of the imaging model. The principle of SPAMM is based on generating a regular pattern of saturated magnetization in the tissue, e.g. myocardium wall. This pattern moves with the tissue. When imaging contraction of the myocardium during the cardiac cycle, the deformation of the pattern is also captured. The regular character of the grid – the tagged pattern – may allow for more reliable tracking of some types of deformations.

The pattern tag lines with sinusoidal modulation in direction of axis x are generated using the following model:

$$I^x_{\Pi_0}(\boldsymbol{X}) = \mathbb{I}_{\Pi_0}(\boldsymbol{X})|\sin(k(X_1 - X_{0,1}))|, \quad \forall \boldsymbol{X} \in \Pi_0, \tag{3.6}$$

where X_1 is the x-component of $\boldsymbol{X}$, k and $X_{0,1}$ are the parameters controlling the density and position of the waves, $\mathbb{I}_{\Pi_0}$ is the characteristic function of domain Π_0. In tagged MRI images the waves are typically generated in two perpendicular directions to form a grid. In 2D, when considering $\boldsymbol{X}_0 = (X_{0,1}, X_{0,2}) = \boldsymbol{0}$ for simplicity, the imaging model reads:

$$I_{\Pi_0}(\boldsymbol{X}) = \mathbb{I}_{\Pi_0}(\boldsymbol{X}) \sqrt{\prod_{i=1}^{2} \left|\sin\left(\frac{\pi X_i}{l}\right)\right|}, \quad \forall \boldsymbol{X} \in \Pi_0, \tag{3.7}$$

where l denotes the distance between the tag lines.

The imaging model is used to generate the tagged pattern over domain Π_0 – the domain occupied by object $\mathcal{B}$ in the reference configuration. After the deformation, the body occupies domain $\Pi = \Phi(\Pi_0)$ and the deformed image is obtained as:

$$I_{\Pi,\Phi}(\boldsymbol{x}) = I_{\Pi_0}(\Phi^{-1}(\boldsymbol{x})), \quad \forall \boldsymbol{x} \in \Omega. \tag{3.8}$$

3.3.2 Model of MRI artifacts

The additional corrupting effect might be incorporated into the imaging model (3.7) to make the resulting synthetic tagged images more realistic. To explain the chosen type of artifacts, we first need to explain the difference between the current state of imaging model I_{Π_0} and MRI. We note that the concept of MRI is explained very simplistically. The model I_{Π_0} assigns intensity to points in the image domain Ω_0. MRI, however, does not construct the image in this way. MRI first creates an image in the so-called temporary image space. The final image is then obtained by applying an inverse Fourier transform to the stored data. However, only a limited number of frequencies can be stored in the temporary image space in a limited amount of time. To simulate this effect of the limited bandwidth of the MR, we may apply Fourier transform to the synthetic image, keep frequency content only within a box window and apply the inverse Fourier transform. The same can be simulated by a convolution of the synthetic image with $\mathrm{sinc}(x) = \sin(x)/x$ function. The deformed image $\tilde{I}_{\Pi,\Phi}$ with this corrupting effect is therefore obtained as:

$$\tilde{I}_{\Pi,\Phi}(\boldsymbol{x}) = \int_{\Omega} I_{\Pi,\Phi}(\boldsymbol{y}) b(\boldsymbol{y} - \boldsymbol{x}) \mathrm{d}\boldsymbol{y}, \quad \forall \boldsymbol{x} \in \Pi, \tag{3.9}$$

where the box-window function b is defined as:

$$b(\boldsymbol{x}) = \prod_{i=1}^{2} \operatorname{sinc}\left(\frac{x_i}{d_i}\right), \tag{3.10}$$

where d_i is the image resolution in the direction of i-th axis.

3.3.3 Formulation of the optimization problem

With the imaging model at hand, the alternative similarity functional $E_{similarity}(\Phi)$ can be defined. Before proceeding to the mathematical formulation, we introduce the basic idea of how the imaging model is incorporated into the problem of finding the mapping $\Phi : \Pi_0 \to \Pi$.

Let us suppose the position of the object $\mathcal{B}$ in the reference configuration, i.e. Π_0, is known. We may therefore generate a synthetic tagged image of the object $\mathcal{B}$ using imaging model (3.7). Then, for any admissible mappings Φ, we obtain the deformed domain $\Pi = \Phi(\Pi_0)$. Furthermore, the position of each material point $\boldsymbol{X}$ after the deformation can be determined as $\Phi(\boldsymbol{X})$. Therefore, synthetic deformed image $I_{\Pi,\Phi}$ can be generated from the reference image using (3.8) or (3.9). Finally, the synthetic and real deformed image can be compared and the mapping Φ is updated based on their difference.

The similarity metric $E_{similarity}(\Phi)$ that would asses the difference between the deformed image $I_{\Pi,\Phi}$ and real deformed image I could be defined in a following way:

$$\hat{E}_{similarity}(\Phi) = \frac{1}{2}\int_{\Pi} \left(I_{\Pi,\Phi}(\boldsymbol{x}) - I(\boldsymbol{x})\ \right)^2 \mathrm{d}\boldsymbol{x}. \tag{3.11}$$

However, it may be more suitable to perform the integration over the reference domain, instead of the deformed domain, the same way it was done in (3.5):

$$E_{similarity}(\Phi) = \frac{1}{2}\int_{\Pi_0} \left(I_{\Pi,\Phi}(\Phi(\boldsymbol{X}))\ - I(\Phi(\boldsymbol{X}))\ \right)^2 \mathrm{d}\boldsymbol{X}. \tag{3.12}$$

When using the basic imaging model (3.7), where $I_{\Pi,\Phi}(\Phi(\boldsymbol{X})) = I_{\Pi_0}(\Phi^{-1}(\Phi(\boldsymbol{X}))) = I_{\Pi_0}(\boldsymbol{X})$, the general equation (3.12) is simplified to:

$$E_{similarity} = \frac{1}{2}\int_{\Pi_0} \left(I_{\Pi_0}(\boldsymbol{X})\ - I(\Phi(\boldsymbol{X}))\ \right)^2 \mathrm{d}\boldsymbol{X}. \tag{3.13}$$

When using the more complicated model (3.9), the synthetic deformed image $I_{\Pi,\Phi}(\Phi(\boldsymbol{X})$ is obtained as:

$$\tilde{I}_{\Pi,\Phi}(\Phi(\boldsymbol{X})) = \int_{\Omega} I_{\Pi,\Phi}(\boldsymbol{y}) b(\boldsymbol{y} - \Phi(\boldsymbol{X}))\mathrm{d}\boldsymbol{y}, \quad \forall \boldsymbol{X} \in \Omega_0. \tag{3.14}$$

The variational formulation of the problem 3.4 is convenient for the incorporation of regularization terms. The regularised problem reads as:

$$\Phi^* = \arg\min_{\Phi} \left(E_{similarity}(\Phi) + E_{reg}(\Phi)\right) \tag{3.15}$$

where E_{reg} is the regularization term. In the presented method, the regularization term proposed by Genet, et al. in [29] is used.

This mechanical regularization is based on the assumption of mechanical equilibrium:

$$\operatorname{Div}(\mathbb{F} \cdot \mathbb{S}) = 0,\ \mathbb{S}^T = \mathbb{S}, \quad \forall \boldsymbol{X} \in \Omega_0, \tag{3.16}$$

where $\mathbb{S} = \mathbb{S}(\Phi)$ is the second Piola-Kirchhoff stress tensor and $\mathbb{F}(\Phi) = \partial\Phi/\partial\boldsymbol{X}$ is the transformation gradient [37]. The regularization term is designed for finite element-based problems, where the object $\mathcal{B}$ is discretized using a mesh of finite elements. For the definition of the regularization term, we denote K the set of elements, F the set of interior faces with corresponding normal vectors $\boldsymbol{N}$, and h the characteristic length of the mesh. The regularization term is defined as:

$$E_{reg} = \sum_K \frac{1}{2}\|Div(\mathbb{F}\cdot\mathbb{S})\|^2_{L^2(K)} + \sum_F \frac{1}{2h}\|\mathbb{F}\cdot\mathbb{S}\cdot\boldsymbol{N}\|^2_{L^2(F)}. \tag{3.17}$$

This regularisation term was used in extracting the motion from various medical image series [29, 45].

3.4 Numerical solution

The models presented in previous sections were implemented in Python. The model and similarity functional were integrated as an addition to the existing finite element-based tool for image registration, implemented in Python and C++, using the FEniCS [48] and VTK [68] libraries.

The optimization problem (3.15) is solved iteratively using Newton's method. The discretization is done using the standard first-order continuous Galerkin elements. In [29], the numerical solution of the optimization problem 3.15 with image intensity-based similarity term 3.5 is described in detail.

The mapping Φ obtained by the numerical solution is obtained in the form of deformation filed U stored at the nodes of the mesh. This is convenient for the subsequent analysis of the deformation, e.g. computation of strains.

The implementation of the presented method is freely available at `https://gitlab.inria.fr/mgenet/dolfin_warp`.

3.5 Experimental results on synthetic images

In [78], the proposed method was tested on 2D synthetic image registration problems. Rigid (translation and rotation) and non-rigid (compression and sheering) transformations of the square object were examined. The impact of added noise on the accuracy of the registration is also investigated in [78]. In this chapter, only the visual results of the motion tracking in the case of shearing and compression are presented.

All presented image series consisted of 30 time-lapse images, each image was 100×100 pixels in size. Imaging model 3.7 was used with the distance $l = 10$ pixels. The synthetic images were generated by the same imaging model used in the image registration stage. In order to make the experiment more realistic, zero-mean gaussian noise was added to the images in both generated image series. The standard deviation of 0.1 (SNR=10) was used in the shearing experiment and 0.3 (SNR=3) in the compression experiment, respectively. In the experiments presented in this work, the effect of corruption artifacts was neglected, and, therefore, the simplified version of $E_{similarity}$ given by 3.13 could be used.

The results of both experiments are shown in Figures 3.1 and 3.2, respectively. Figure 3.1 shows the synthetic images at three different times during the deformation (shearing). In Figure 3.1a, the superimposed triangular mesh is in the reference configuration – aligned with the body $\mathcal{B}$. Figures 3.1b and 3.1c, show the mesh in the middle and the end of the deformation process. Figure 3.2 shows the superimposed mesh obtained using the proposed method for the second type of deformation – compression. In both experiments, the mesh follows the object during the deformation.

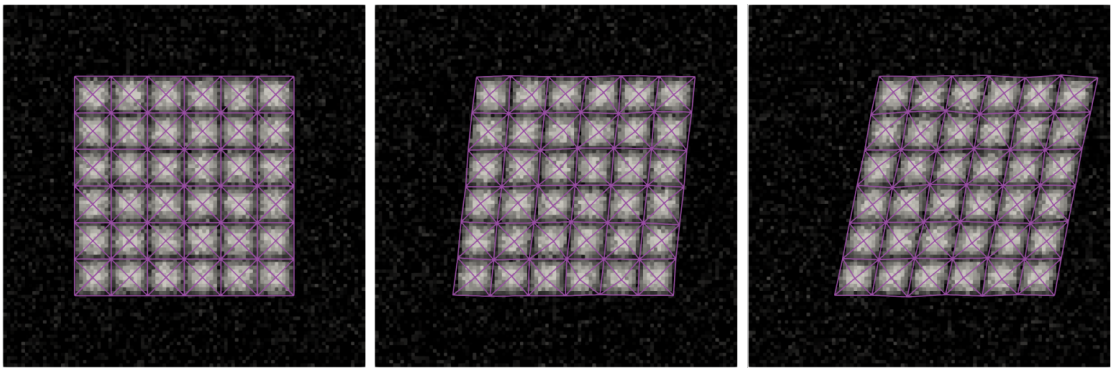

(a) Time frame 0. **(b)** Time frame 14. **(c)** Time frame 29.

Figure 3.1: The process of shearing the tagged square, captured in three time frames. The synthetic images contain added noise (SNR=10). The superimposed mesh shows the deformations extracted from the image series using the proposed method.

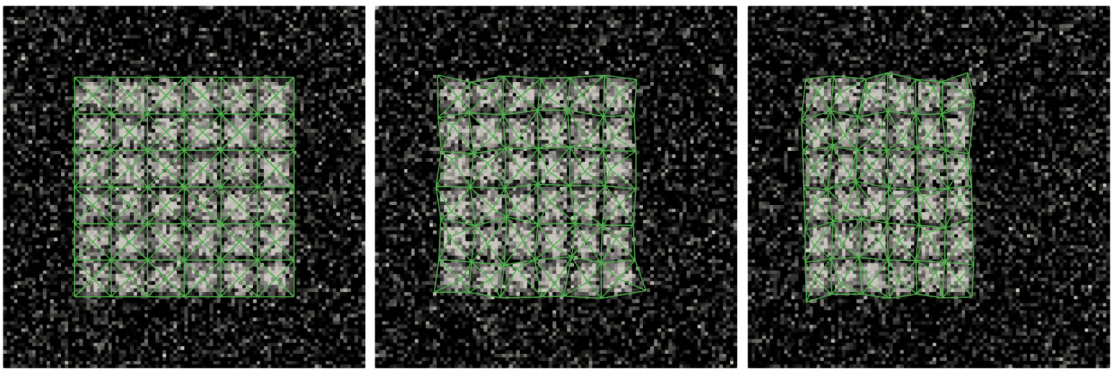

(a) Time frame 0. **(b)** Time frame 14. **(c)** Time frame 29.

Figure 3.2: The compression of the tagged square, captured in three time frames. The synthetic images contain added noise (SNR=3). The superimposed mesh shows the deformations extracted from the image series using the proposed method.

3.6 Conclusions

We introduced a novel approach to the problem of image registration. This approach utilized an imaging model used to create synthetic images similar to processed images. The similarity functional based on this imaging model was combined with the existing mechanics-based regularization. The resulting minimization problem was discretized using the finite element method and solved by Newton's method.

The proposed method was tested on synthetic images. The method was shown to perform well in all presented cases. In the future, the method should be evaluated on more complicated shapes and transformations. Finally, the method should be tested on real images.

Personal contribution

The author participated in the design and implementation of the imaging model, that would allow the integration with the existing finite element-based solver.

Estimation of left ventricular torsion 4

In this chapter, we present an application of cardiac motion analysis using an image registration method. The mathematical method and subsequent clinical study including patients with tetralogy of Fallot after a surgical repair was described in [12]:

Castellanos, D. A., Škardová, K., Bhattaru, A., Berberoglu, E., Greil, G., Tandon, A., Dillenbeck, J., Burkhardt, B., Hussain, T., Genet, M., and Chabiniok, R. (2021). **Left ventricular torsion obtained using equilibrated warping in patients with repaired tetralogy of Fallot**. Pediatric Cardiology, 42(6):1275–1283.

The aim of the published study was to evaluate a novel method for the assessment of left ventricular torsion as an early indicator of left ventricular systolic dysfunction. While in this paper the topic has been described from a clinical perspective, in this chapter we will attempt to describe in more detail the proposed workflow and how a general image registration method can be incorporated into the solution of a real clinical problem.

4.1 Introduction to the tetralogy of Fallot

Tetralogy of Fallot (TOF), as described also in [15], is a congenital heart disease characterized by specific birth defects that affect the normal blood flow through the heart and that would lead to death in infancy, if untreated. As depicted in 4.1b, these defects typically are:

- pulmonary stenosis – a narrowing of the outflow from the right ventricle (RV),
- a ventricular septal defect – a hole allowing blood to flow between the two ventricles,
- right ventricular hypertrophy – a thickening of the right ventricular muscle,
- an overriding aorta, which is when blood from both ventricles can enter the aorta, which leads to the mixing of both oxygenated and deoxygenated blood.

The diagrams of a normal heart and heart with the tetralogy of Fallot are shown in Figures 4.1a and 4.1b, respectively. The surgical repair od the tetralogy of Fallot (rTOF) typically consists of repairing the ventricular septal defect and correction of the pulmonary stenosis transannular patch. The heart after full surgical repair is shown in Figures 4.1c.

Although the tetralogy of Fallot predominantly affects the right ventricle. A significant number of adults with repaired TOF exhibit left ventricular (LV) dysfunction [24]. As described

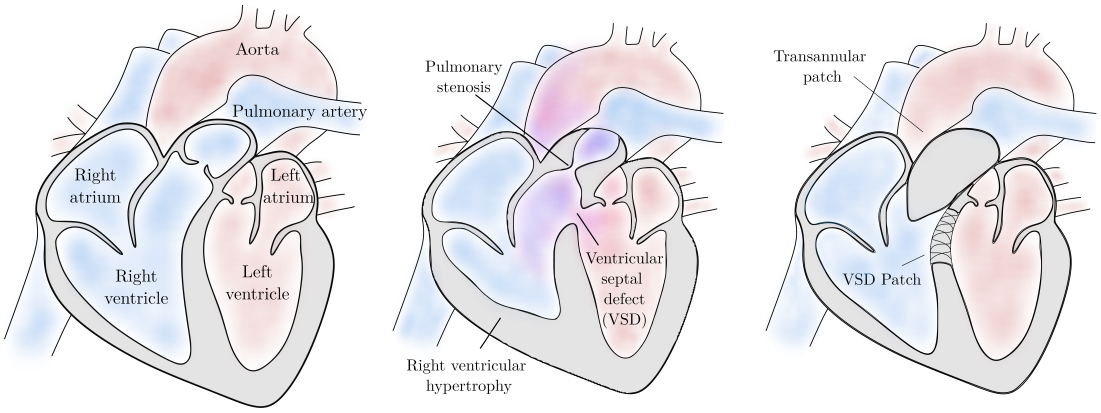

(a) Normal heart. **(b)** Tetralogy of Fallot **(c)** Repaired tetralogy of Fallotl

Figure 4.1: Diagram of a normal heart, one with tetralogy of Fallot and one with repaired tetralogy of Fallot.

in [15, 24, 31], many of the right-ventricle-related factors may contribute to suboptimal left ventricular mechanics or even a loss in left ventricular function in patients with rTOF. Therefore, early identification of deteriorating left ventricular mechanics and function may be used to guide the clinical management in this population. This task is quite challenging, however, because the findings suggest that the progression of the left ventricular dysfunction may be rather gradual, starting decades before the first symptoms. Studies suggest that one of the early indicators of changes in LV mechanics may be the loss of torsion in the LV [81]. This property of the LV is also investigated in this chapter.

4.2 The objective

Torsion, also referred to as a twist, is a characteristic feature of ventricular contraction. Looking from the apex, the base (top part of the ventricle) of a normal heart rotates clockwise in the systole while the apex (the bottom of the left ventricle) rotates counter-clockwise, producing a twisting motion [54]. For a simplified diagram of the twist in LV, see Figure 4.2. Typically, LV torsion is defined as the difference in rotation between the LV apex and base at peak systole. In this work, the LV twist gradient is also evaluated, which is obtained as the difference in rotation divided by the distance between the base and apex to accommodate the differences in LV dimensions between patients.

The torsion is usually determined based on a series of images capturing the contraction of the heart. However, it has been documented that tissue tracking analysis and the subsequent calculation of torsion performed in standard clinical software exhibits a large variance of obtained results [9]. The aim of this study is to propose a method to determine LV torsion with higher reliability based on the same input data.

4.3 Materials and methods

In this section, we first describe the clinical data used in the study, their pre-processing, and the estimation of LV twist and other parameters using standard clinical software. Subsequently, we describe the proposed method of LV twist estimation using the same input data.

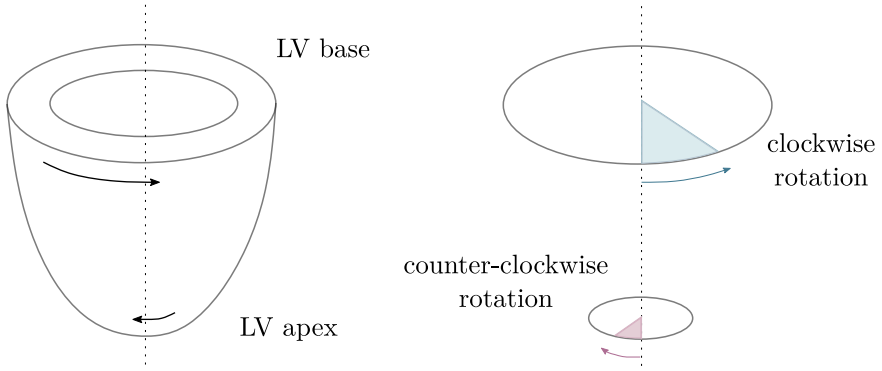

Figure 4.2: Diagram of rotation of base and apex of normal LV. The direction of rotation is indicated as clockwise or counterclockwise when viewed from the apex to the base.

4.4 Clinical data

The study in [12] was designed as a single-center retrospective study using anonymized data obtained from routine clinical scans. The studied dataset consisted of 76 cases of rTOF patients and ten normal controls. The analysis was performed using short-axis cine MR images. In all cases, the ventricle contours were manually segmented as a part of routine clinical work, using standard clinical software (CVI42, version 5.10.1, Calgary, Canada).

The control group was used to evaluate the dependence of results on the LV segmentation. In other words, it was investigated how the twist differed for different input segmentations. The twist was determined using CVI42 and the proposed method. The compared quantities were:

- the difference in results when using segmentations provided repeatedly by the same observer (the intra-observer variability)
- the difference in results when using segmentations provided by different observers (the inter-observer variability)

The comparison between normal and abnormal torsion was performed among the patients with rTOF, where the proposed method was used to evaluate the twist.

Additionally, standardly used indicators of LV and RV function were assessed for each subject: end-systolic volume of LV and RV (LVESV, RVESV), the end-diastolic volume of LV and RV (LVEDV, RVEDV), ejection fraction of LV and RV (LVEF, RVEF).

The end-diastolic (captured at the end of the relaxed phase of the cardiac cycle) LV endocardial and epicardial surface meshes surface and the short-axis cine MR image series were used as the input data for the proposed method described in the next section. An example of the surface meshes exported from CVI42 overlaid on the MRI image data in two slices is shown in Figure 4.3.

4.5 The proposed workflow

In this section, we describe the workflow used to obtain the LV torsion based on the MR image series and the segmented contours. The process consisted of three steps – the preparation of the data, the motion tracking, and the calculation of LV twist based on the extracted motion.

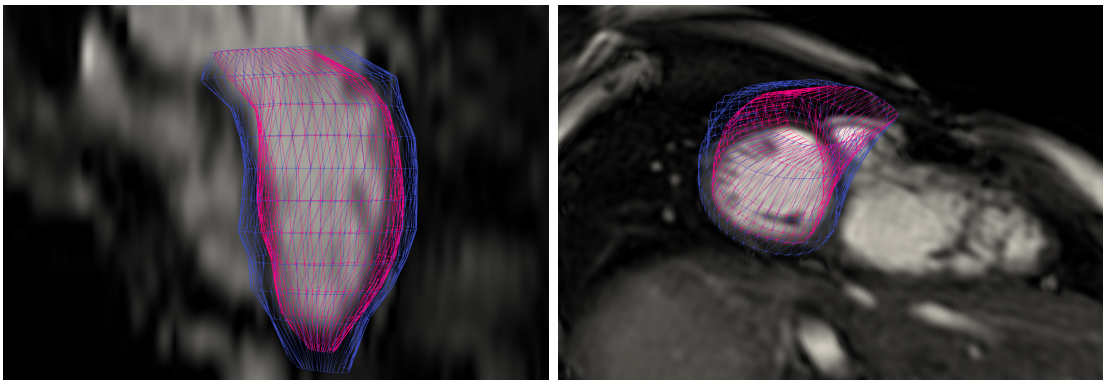

Figure 4.3: Example of the segmented endocardial (pink) and epicardial (blue) LV surface mesh overlaid over two sections through the stack of short-axis MRI cine.

4.5.1 Data preparation

The image data were exported for each subject in DICOM format. The images are not truly 3D but are a stack of 2D slices. The orientation of these slices in the real space (in the patient's frame of reference) and in the image space is shown in Figure 4.4. The stack of 2D slices in the image space forms a 3D image. The number of stacked images was low compared to their dimensions. Due to this, the 3D image resolution in the direction of z-axis was initially significantly lower than the resolution in the xy-plane.

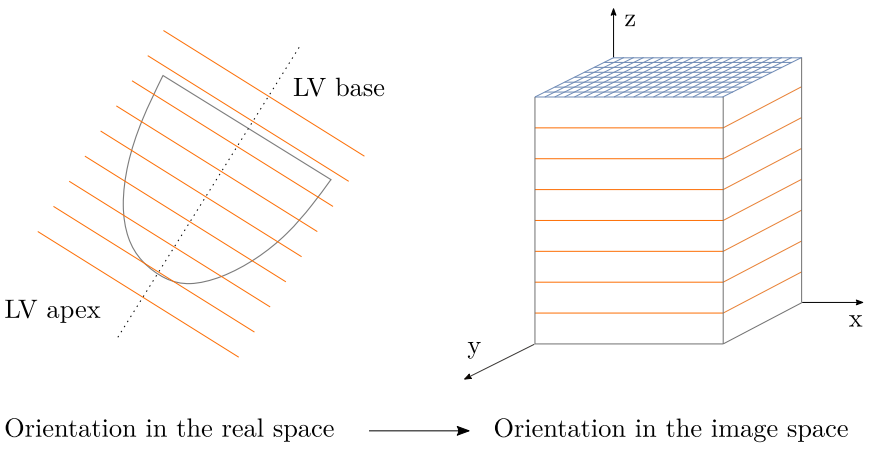

Figure 4.4: Diagram of the orientation of the 2D MRI images in the real space and in the image space. In the image space, the stack of 2D slices forms a 3D image. The image resolution in the direction of z-axis is significantly lower than the isotropic resolution in the xy-plane.

The image resolution in the xy-plane, was isotropic with a voxel size of approximately 1 mm $\times$ 1 mm. In the z-axis direction, the resolution was 8-10 mm. This disproportion in image resolution is also visible in Figure 4.3. The input data were therefore interpolated to an isotropic voxel size in all three directions using the MeVisLab software (Application Framework for Medical Image Processing and Visualization, version 3.0.2, Bremen, Germany). The voxel spacing in the resulting interpolated image was therefore approximately 1 mm $\times$ 1 mm $\times$ 1 mm.

The motion tracking method used in the second step required a volume mesh of the tracked object. Therefore, the endocardial and epicardial surfaces needed to be connected into a single

object. Both meshes, segmented from the image data in the real space, were first transformed to the image space. In the image space, the meshes were closed by a plane perpendicular to the z-axis at the base and apex area to obtain a closed surface. Then, the unified surface mesh was used to generate volume mesh using GMSH [30]. Finally, the segmented contours were extended inward and outward and this additional space was also meshed by tetrahedral elements. The volume mesh with the extension is shown in Figure 4.5. This extension of the LV allowed tracking objects outside the myocardial contours, such as the papillary muscles located inside the ventricle (shown in the example in Figure 4.3). The inclusion of these additional reference points improved the ability to detect in-plane rotation. It should be noted that the LV has a relatively homogeneous image intensity on cine MRI images. Therefore, the detection of LV rotation is generally more challenging than, for example, the detection of contraction or dilation and without the inclusion of additional landmarks, it could easily be missed.

The extended computational meshes of LV had approximately 2000 nodes and 8000 to 10000 tetrahedral elements. The additional layer was dropped after the motion tracking step and the twist was evaluated only in the segmented region.

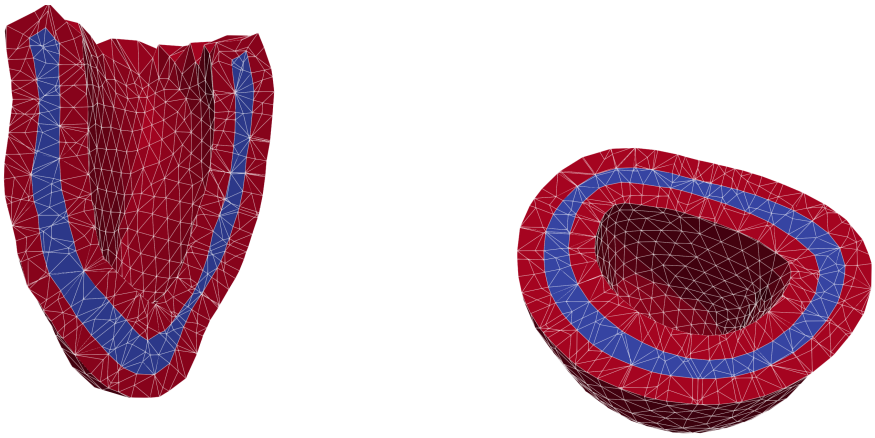

Figure 4.5: Example of the volume mesh of the segmented LV (blue) and an additional layer of elements used to track the motion of the objects surrounding the segmented domain (red).

4.5.2 Tracking the motion of the ventricle

The motion tracking was performed using the finite element-based method used in Chapter 3 therefore we use some of the previously defined terms. In this chapter, the tracked object $\mathcal{B}$ corresponds to the LV.

The short-axis cine MR image series captures one cardiac cycle in n images corresponding to times $t_0, \ldots, t_{n-1}$. In the studied dataset, $n = 30$ was typically used. The LV contours are segmented at the end of the diastole – the image in which the LV volume is the largest. We denote this image I_0 and the corresponding time t_0. Using the terminology used in Chapter 3, image I_0 shows the body $\mathcal{B}$ in reference configuration, and images $I_1, \ldots, I_{n-1}$ show the body $\mathcal{B}$ in the deformed configuration. The time frames are processed sequentially. At each time $t = t_1, \ldots, t_{n-1}$, we seek mapping Φ (3.2) that would transform the body $\mathcal{B}$ from the reference configuration to the deformed one. The optimal mapping Φ^* is found as:

$$\Phi^* = \arg\min_{\Phi} \left(E_{similarity}(\Phi) + E_{reg}(\Phi) \right), \tag{4.1}$$

where the E_{reg} is the mechanical regularization term proposed by Genet, et al. in [29]. This term was described in the previous Chapter 3. Given cine MR image data were used (i.e. image

intensity remains constant over time), the intensity-based image similarity term 3.5 can be employed:

$$E_{similarity}(\Phi) = \frac{1}{2}\int_{\Pi_0} \left(I(\Phi(\boldsymbol{X})) - I_0(\boldsymbol{X})\right)^2 \mathrm{d}\boldsymbol{X}, \tag{4.2}$$

where I_0 is the reference image (where the contours were segmented) and I is the deformed image. The optimal mapping from time frame t_{n-1} is used as an initial guess for mapping in time frame t_n.

The output of this step is a series of mappings $\Phi_1, \ldots, \Phi_{n-1}$. The identity mapping Φ_0 may be added to the series for completeness. This series of mappings, capturing one cardiac cycle, is used in the next step to determine the torsion of the LV.

4.5.3 Estimation of left ventricular torsion

Two torsion-related characteristics of LV contraction were calculated: peak systolic twist (the difference in the angles by which the base and apex are rotated at the peak of LV contraction), and peak systolic twist gradient (the peak systolic twist divided by the distance between the base and apex). Both values are estimated based on the mesh of LV in the reference configuration and the series of mappings $\Phi_0, \ldots, \Phi_{n-1}$ obtained in the previous step.

First, the angle $\beta(\boldsymbol{X})$ by which each node is rotated during the transition from the reference position $\boldsymbol{X}$ to the deformed position $\boldsymbol{x} = \Phi_i(\boldsymbol{X})$ is determined at each time t_i. Only the rotations in the xy-plane are considered. It is assumed that the component outside the xy-plane can be neglected without introducing significant errors to the model due to the orientation of the image data, where the base-to-apex LV axis is effectively parallel to the z-axis.

In the present study, the dependence of the angle β on the z-component of the corresponding point $\boldsymbol{X}$ was assumed to be linear. Therefore, a linear regression was performed on the angle values and z-components of the nodes. This step reduced the effect of point misregistration due to noise in the image data and also ensured that the change in rotation direction from clockwise to counterclockwise could only occur at one point along the base-to-apex axis of the LV. An example of the distribution of β along the z-axis is shown in Figure 4.6, the evolution rotation of base and apex of LV in time is shown in Figure 4.7. Finally, the twist is obtained as the difference between the linearly fitted base and apex rotation.

4.6 Results

In this section, we provide only a summary of the results. More details and the additional statistical analyses carried out as part of the evaluation can be found in the full text of the study [12].

In the control group, the motion tracking step of the proposed method failed to converge to admissible deformation in 1 of the 10 cases. The LV torsion therefore could not be estimated in this case. The other software provided results in all cases. The comparison however showed that in the rest of the cases, where both methods provided results, the proposed method provides more consistent results compared to the standard clinical software.

In the rTOF group, torsion was obtained using the proposed methods in 68 of 76 cases. In the 68 cases where the motion tracking step was successfully performed, a visual inspection of torsion during the cardiac cycle was used to categorize the cases into two groups: those with normal systolic torsion (clockwise basal rotation and counterclockwise apical rotation) and those with loss of systolic torsion (loss of normal clockwise systolic basal rotation). Loss of torsion was noted in 32 of the 68 cases.

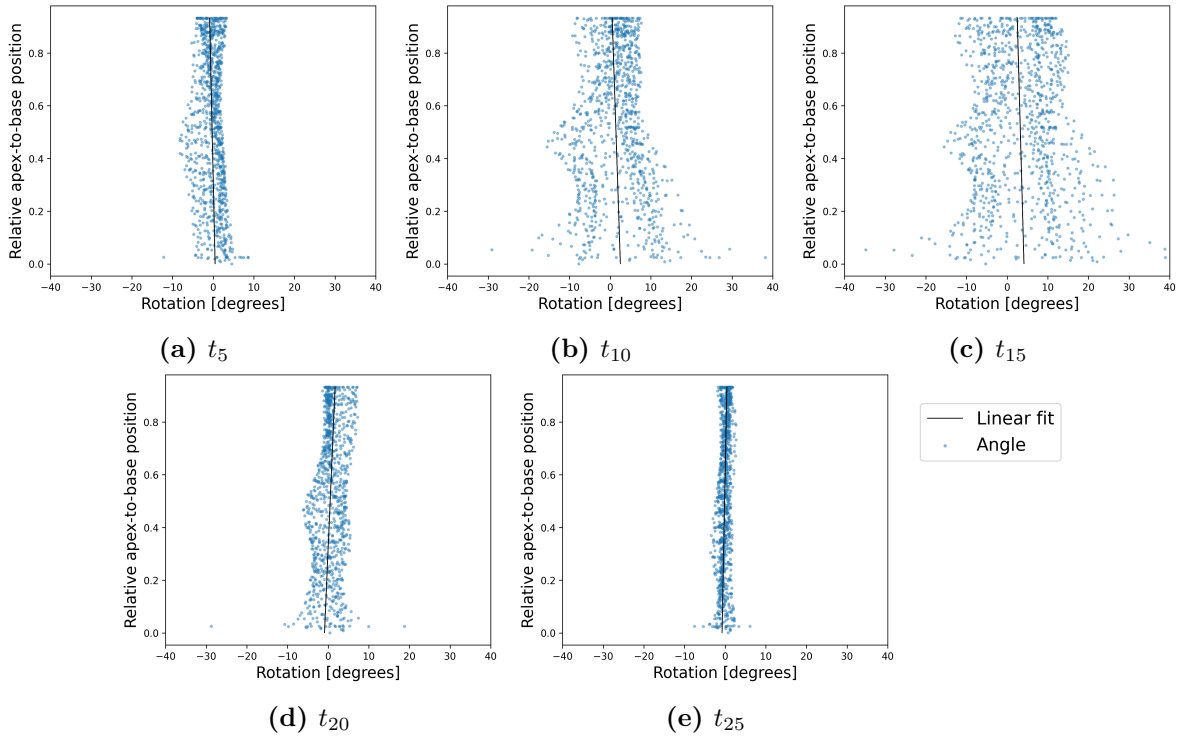

Figure 4.6: The distribution of β along the z axis in 5 of the 30 time frames. Linear regression was performed on the angle values and z-components of the nodes. The position on z-axis is visualized in a relative sense as the position between the LV apex and base.

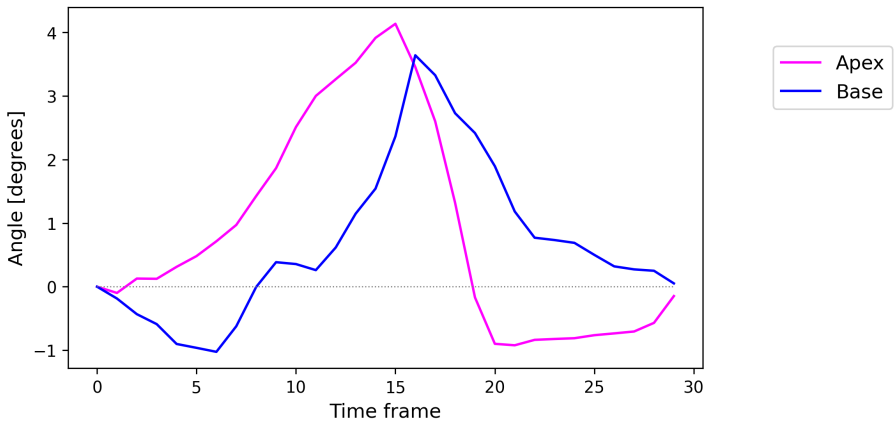

Figure 4.7: The rotation of the base and apex of LV in one cardiac cycle (30 time frames). The clockwise rotation is represented by negative values, and the counter-clockwise rotation by positive values). The LV contraction peaks approximately at time frame t_{15}.

There was a significant difference in the peak systolic twist determined by the proposed method in the two groups. In the group with normal torsion, the average peak systolic twist gradient was 0.16 [degrees/cm] while it was 0.01 [degrees/cm] in the group with the observed loss of torsion. On the contrary, no difference was found when comparing the other characteristics, (RVESV, RVEDV, RVEF, LVESV, LVEDV, and LVEF).

4.7 Discussion and conclusions

The proposed method based on image registration with mechanical regularization term can be used to extract features of left ventricular contraction. This has been demonstrated in the example of extraction of left ventricular torsion for patients with repaired tetralogy of Fallot, where approximately 90% success rate was achieved. The study suggests that this approach could be used to detect the insidious progression of left ventricular dysfunction with greater robustness compared with standard clinical software.

There was no significant association between the torsion loss and other ventricular parameters indicative of deterioration in cardiac status, such as reduced ventricular ejection fraction. We note, that a long-term follow-up of the studied population would be required to further support the hypothesis of a relationship between left ventricular torsion loss and worsening of ventricular parameters and poor clinical outcomes.

The method has shown greater robustness with regard to input segmentation, but the coefficient of variance still remains high. This is consistent with previous publications on this topic [81]. Also, there are still aspects in the motion tracking step that should be addressed, as evidenced by the 8 patients with rTOF and 1 control subject in whom the motion tracking step failed. Although modification of the image registration method itself could be considered, in some cases these problems may be related to the image data. Specifically, the interpolation of short-axis cine stacks in the longitudinal direction to obtain 3D image data may be problematic due to the significant difference in the resolution in the direction of z-axis. This could be improved by combining the short-axis cine stacks with another series of images, such as long-axis cine images.

Finally, while this is a study performed on a cohort of patients with rTOF, it should be noted that the method could also be used to evaluate torsion in other cardiac patients.

Personal contribution

The author contributed to the design and implementation of data pre-processing tools and the computation of torsion directly in the clinical environment of the Division of Pediatric Cardiology, UT Southwestern Medical Center Dallas. The author was also responsible for the implementation of the automation of these steps and testing the method on several datasets.

Image enhancement by solving inverse diffusion equation

5

Image enhancement covers many techniques in image processing. Generally, it includes all procedures that either improve the quality of the image data or make it easier for visual interpretation by a human audience. Commonly used techniques include contrast enhancement, denoising, enhancement of edges, or deblurring. The focus of this chapter is on image deblurring – the process of restoring a sharp image from the blurred input image.

Image blurring can occur when using various imaging techniques. For example in photography, blurriness is often the result of light distortion, movement of either the imaging device or the imaged object, or the imaged object being out of focus. Blurring can also be present in MRI image data. In this case, the blurring may be a result of the patient's movement – e.g. cardiac and respiratory motion – or the partial volume effect mentioned in Section 3.1.

Blurring can reduce the sharpness of edges and the visibility of smaller details in the image. Image data processing is often heavily dependent on the information about edges. Consequently, the reliability of indicators derived from MRI images, e.g. torsion or ejection fraction, may be affected by the quality of segmentation which in turn may be affected the level of image blurring. Therefore, image deblurring or blur assessment techniques are being actively researched in the field of medical imaging. The review of the state of the art of image deblurring methods can be found in [66]. Recently, the use of neural networks and specifically convolutional neural networks have been intensively explored also in the field of medical imaging [46, 86].

In this chapter, we examine the solution of the inverse heat equation for the task of image deblurring. We intend to solve the problem by solving the adjoint equation. A similar problem was already studied in several publications, such as [52], where the deblurring was combined with noise removal. However, to the author's best knowledge, the problem was not studied using the adjoint formulation. This chapter is not intended to present a method with results superior to the existing state of the art techniques but rather to provide an alternative mathematical approach to the given optimization problem.

First, the general principle of the adjoint method is presented in Section 5.2. In Section 5.3, the image deblurring problem is formulated as a minimization problem with PDE constraint, and the solution using the adjoint formulation is derived. The numerical solution of the derived equations is described in Section 5.4 and finally, the results of the proposed method are presented in Section 5.5.

5.1 Gradient descent method for minimization problems

In this section, we briefly describe the descent algorithm that will be used to solve the optimization problems in this chapter. Gradient descent is an iterative optimization method for finding a local minimum of a differentiable function. Let us consider a simple minimization problem for function $f : \mathbb{R}^n \to \mathbb{R}$:

$$\min_u f(u). \tag{5.1}$$

We denote the initial guess of the parameter u by u_{init}. The algorithm is initialized by this initial guess, i.e. $u_0 = u_{init}$. Then in each iteration of the algorithm, the estimation is updated as $u_{i+1} = u_i - \nu \nabla f(u_i),\ i \geq 1$. The parameter $\nu \in \mathbb{R}$ is called the step of the gradient descent.

When using this algorithm, the derivative of f with respect to the parameter u need to be computed in each iteration. In the following section, we describe, how the direct computation of the derivative may be avoided.

5.2 Gradient computation in general PDE constrained minimization problem

Let us first formulate a general minimization problem with PDE constraints. We follow the formulation of the problem used [8] and [36], where the theoretical background for the following steps can be found.

Let us define a loss functional $J : Y \times \Theta \to \mathbb{R}$, where Y, Θ are Banach spaces. Space Θ will be referred to as the space of parameters and Y as the space of solutions.

We further assume the solution y and parameter θ to be bound together by a constraint $e : Y \times \Theta \to H$, where H is a Hilbert space. We consider constraint $e(y, \theta) = 0$ consisting of system of partial differential equations (PDEs) with boundary and initial conditions. We assume, that the constraint $e(y, \theta) = 0$ implicitly defines unique mapping $\theta \in \Theta \to y(\theta) \in Y$, and also that function $y = y(\theta)$ is differentiable with respect to θ. Then the full PDE constraint minimization problem reads:

$$\min_{\theta \in \Theta} J(y(\theta), \theta) \quad \text{subject to} \quad e(y(\theta), \theta) = 0. \tag{5.2}$$

As stated above, we want to solve this problem by the gradient descent method. Therefore, computing the derivative of J with respect to the optimized parameter θ is required in each iteration. Because y is uniquely determined by θ, we may define reduced functional $\hat{J}(\theta) = J(y(\theta), \theta)$. Next, we would compute the Fréchet derivative of $\hat{J}(\theta)$ formally. For clarity of writing, we keep $J(y(\theta), \theta)$ and we proceed to compute the derivative with respect to θ in this sense. First, we define the Lagrange function L:

$$L(y, \theta, \lambda) = J(y(\theta), \theta) + \langle \lambda | e(y(\theta), \theta) \rangle \,, \tag{5.3}$$

where $\langle . | . \rangle$ denotes scalar product in the Hilbert space H. Function $\lambda \in H$ will be referred to as the Lagrange multiplier. Given the constraint $e(y(\theta), \theta) = 0$ is met, $J(y(\theta), \theta)$ is trivially equal to $L(y, \theta, \lambda)$ for any λ. This equality and, therefore, also equality of the derivatives of both functions is used in the next steps.

Let us now compute the derivative of L with respect to θ at point $\theta^* \in \Theta$, denoted by $L'(\theta^*)$. The partial derivatives of J with respect to the first and second argument are denoted $\frac{\partial J}{\partial y}$ and $\frac{\partial J}{\partial \theta}$, respectively. The derivative of y with respect to θ at point θ^* is denoted by $y'(\theta^*)$. By differentiating 5.3, we obtain:

$$L'(\theta^*)[s] = \frac{\partial L}{\partial y} y'(\theta^*)[s] + \frac{\partial L}{\partial \theta}[s] = \frac{\partial J}{\partial y} y'(\theta^*)[s] + \frac{\partial J}{\partial \theta}[s] + \left\langle \lambda \;\middle|\; \frac{\partial e}{\partial y} y'(\theta^*)[s] + \frac{\partial e}{\partial \theta}[s] \right\rangle, \quad (5.4)$$

where $s \in \Theta$. Using the Riesz representation theorem [36], we denote the representation of $\frac{\partial J}{\partial y}$ by J_y^*:

$$\frac{\partial J}{\partial y} y'(\theta^*) = \left\langle J_y^* | y'(\theta^*) \right\rangle. \quad (5.5)$$

The adjoint operator to $\frac{\partial e}{\partial y}$ will be denoted by

$$\left\langle \lambda \;\middle|\; \frac{\partial e}{\partial y} y'(\theta^*)[s] \right\rangle = \left\langle \left(\frac{\partial e}{\partial y}\right)^* \lambda \mid y'(\theta^*)[s] \right\rangle. \quad (5.6)$$

Substituting both expressions to equation 5.4, the following steps can be taken to regroup the expressions on the right hand side of the equation:

$$\begin{aligned} L'(\theta^*)[s] &= \left\langle J_y^* | y'(\theta^*)[s] \right\rangle + \frac{\partial J}{\partial \theta}[s] + \left\langle \left(\frac{\partial e}{\partial y}\right)^* \lambda \;\middle|\; y'(\theta^*)[s] \right\rangle + \left\langle \lambda \;\middle|\; \frac{\partial e}{\partial \theta}[s] \right\rangle \\ &= \left\langle J_y^* + \left(\frac{\partial e}{\partial y}\right)^* \lambda \;\middle|\; y'(\theta^*)[s] \right\rangle + \frac{\partial J}{\partial \theta}[s] + \left\langle \lambda \;\middle|\; \frac{\partial e}{\partial \theta}[s] \right\rangle. \end{aligned} \quad (5.7)$$

We note, that if such λ could be found, that $\left(\frac{\partial e}{\partial y}\right)^* \lambda = -J_y^*$ the first expression on the right side would be equal to zero and the potentially complicated computation of $y'(\theta^*)$ would be avoided.

Therefore, the adjoint approach to computing $L'(\theta^*)$ is following:

1. Solve the adjoin equation for λ: $\left(\frac{\partial e}{\partial y}\right)^* \lambda = -J_y^*$.
2. Compute $L'(\theta^*)$: $L'(\theta^*)[s] = \frac{\partial J}{\partial \theta}[s] + \left\langle \lambda \;\middle|\; \frac{\partial e}{\partial \theta}[s] \right\rangle = \frac{\partial L}{\partial \theta}[s]$.

Let us summarize the findings: if λ is the solution of the adjoint equation, then the derivative $L_{\theta^*}[s]$ is simplified to $\frac{\partial L}{\partial \theta}[s]$. Therefore, the derivative of J with respect to the parameter θ is avoided.

5.3 Image deblurring as a PDE constrained minimization problem

The problem addressed in this section is reconstructing the original image from the blurred image. Similarly to Chapter 2, we represent the original image by image function $I_0 : \Omega \to \mathbb{R}$ and the blurred image by the function $B : \Omega \to \mathbb{R}$, where Ω is the spatial domain of the image. We assume the domain $\Omega \subset \mathbb{R}^2$ to be unit square.

5.3.1 Formulation of the problem

In this chapter we deal with one type of blur – the Gaussian blur. This type of blurring process can be modeled by solving a heat equation:

$$\begin{aligned} \frac{\partial I(\boldsymbol{x},t)}{\partial t} &= \omega \Delta I(\boldsymbol{x},t) \quad \text{on} \quad \Omega \times (0,T), \\ I(\boldsymbol{x},0) &= I_0(\boldsymbol{x}) \quad \text{on} \quad \Omega \times (0,T), \\ \frac{\partial I(\boldsymbol{x},t)}{\partial \boldsymbol{n}} &= 0 \quad \text{on} \quad \partial\Omega \times (0,T), \end{aligned} \tag{5.8}$$

where $\boldsymbol{n}$ is normal vector to the edge $\partial\Omega$ of domain Ω and ω is the diffusion coefficient. The result at the final time T is the blurred image $B(\boldsymbol{x}) = I(\boldsymbol{x},T)$. We consider setting $I_0(\boldsymbol{x}) \in \mathcal{C}^2(\bar{\Omega})$, $I(\boldsymbol{x},t) \in \mathcal{C}^2(\bar{\Omega} \times [0,T])$.

We formulate the problem of deblurring as finding such initial image I_0 based on $B(\boldsymbol{x})$. The goal is to find such I_0, so that when the known blur is applied, the final image $I(\boldsymbol{x},T)$ is as close as possible to image $B(\boldsymbol{x})$. In this problem, the parameters θ control the initial image I_0. We set $I_0(\boldsymbol{x}) = \theta(\boldsymbol{x})$ and therefore also $I = I(\boldsymbol{x},t,\theta)$. In the notation of the previous section, $Y = \mathcal{C}^2(\bar{\Omega} \times [0,T]), \Theta = \mathcal{C}^2(\bar{\Omega} \times [0,T])$.

We assume all parameters of the blurring process – diffusion coefficient ω and final time T – are known and not dependent on θ. We define loss function J:

$$J(I(\theta),\theta) = \int_\Omega \frac{1}{2} \left(I(\boldsymbol{x},T,\theta) - B(\boldsymbol{x})\right)^2 \mathrm{d}\boldsymbol{x}. \tag{5.9}$$

The PDE constraint e contains the diffusion equation (5.8). In the notation used in Section (5.2), we consider $H = \mathrm{L}^2(\bar{\Omega} \times [0,T]) \times \mathrm{L}^2(\bar{\Omega}) \times \mathrm{L}^2(\partial\Omega \times [0,T])$, and $e(I,\theta)$ reads:

$$e(I,\theta) = \begin{bmatrix} \frac{\partial I}{\partial t} - \omega \Delta I \\ I - I_0 \\ \frac{\partial I(\boldsymbol{x},t)}{\partial \boldsymbol{n}} \end{bmatrix}. \tag{5.10}$$

Combining the loss function J and the constrains e, the constrained minimization problem reads analogical to (5.2):

$$\begin{aligned} \min_\theta \int_\Omega \frac{1}{2} \left(I(\boldsymbol{x},T,\theta) - B(\boldsymbol{x})\right)^2 \mathrm{d}\boldsymbol{x} \quad &\text{subject to} \\ \frac{\partial I(\boldsymbol{x},t,\theta)}{\partial t} &= \omega \Delta I(\boldsymbol{x},t,\theta) \quad \text{on} \quad \Omega \times (0,T), \\ I(\boldsymbol{x},0,\theta) &= I_0(\boldsymbol{x},\theta) \quad \text{on} \quad \Omega \times (0,T), \\ \frac{\partial I(\boldsymbol{x},t,\theta)}{\partial \boldsymbol{n}} &= 0 \quad \text{on} \quad \partial\Omega \times (0,T). \end{aligned} \tag{5.11}$$

5.3.2 Computation of the gradient

We formally follow the approach used in section 5.2 in order to simplify the computation of gradient. Analogically with Lagrangian function in the general case (5.3), we define the function for problem (5.11). When denoting the Lagrange multipliers $\lambda = (\lambda_1, \lambda_2, \lambda_3) \in H$, the Lagrangian

function reads:

$$\begin{aligned} L(I,\theta,\lambda_1,\lambda_2,\lambda_3) = &\int_\Omega \frac{1}{2}\left(I(\boldsymbol{x},T,\theta) - B(\boldsymbol{x})\right)^2 \mathrm{d}\boldsymbol{x} \\ &+ \int_\Omega \int_0^T \lambda_1(\boldsymbol{x},t)\left(\frac{\partial I(\boldsymbol{x},t,\theta)}{\partial t} - \omega\Delta I(\boldsymbol{x},t,\theta)\right)\mathrm{d}\boldsymbol{x}\mathrm{d}t \\ &+ \int_\Omega \lambda_2(\boldsymbol{x})\left(I(\boldsymbol{x},0,\theta) - I_0(\boldsymbol{x},\theta)\right)\mathrm{d}\boldsymbol{x} \\ &+ \int_{\partial\Omega}\int_0^T \lambda_3(\boldsymbol{x},t)\left(\frac{\partial I(\boldsymbol{x},t,\theta)}{\partial \boldsymbol{n}}\right)\mathrm{d}S\mathrm{d}t \end{aligned} \tag{5.12}$$

As was explained in the previous section, the loss function J is equal to the Lagrangian function L for any $\lambda_1, \lambda_2, \lambda_3$, given that the PDE constraint is satisfied. Therefore also the derivatives of J and L are equal under such condition.

Therefore, we proceed to compute derivative of the Lagrangian function L with respect to argument θ at point θ^* and direction s. We use the same notation for the derivatives as in the general case in Section 5.2:

$$L'(\theta^*)[s] = \frac{\partial L}{\partial I} I'(\theta^*)[s] + \frac{\partial L}{\partial \theta}[s] \tag{5.13}$$

It was demonstrated in Section 5.2, that the first term $\frac{\partial L}{\partial I} I'(\theta^*)[s]$ can be made equal to zero, under a specific set of conditions. The derivative is then reduced to the second term $\frac{\partial L}{\partial \theta}[s]$.

Let us derive these conditions. We will simplify the notation and use $I'(\theta^*)[s] = v$. We also omit explicitly writing the arguments of the functions in following equations. The function values at initial and final time will be denoted by $|_{t=0}$ and $|_{t=T}$. We derive:

$$\begin{aligned} \frac{\partial L}{\partial I} v = &\int_\Omega \left(I|_{t=T} - B(\boldsymbol{x})\right) v|_{t=T} \mathrm{d}\boldsymbol{x} + \int_\Omega \int_0^T \lambda_1 \left(\frac{\partial v}{\partial t} - \omega\Delta v\right)\mathrm{d}\boldsymbol{x}\mathrm{d}t \\ &+ \int_\Omega \lambda_2 (v|_{t=0} - s)\mathrm{d}\boldsymbol{x} + \int_{\partial\Omega}\int_0^T \lambda_3 \left(\frac{\partial v}{\partial \boldsymbol{n}}\right)\mathrm{d}S\mathrm{d}t. \end{aligned} \tag{5.14}$$

Next, we offload the derivatives in the second term using Green's formula [44]:

$$\int_0^T \lambda_1 \frac{\partial v}{\partial t}\mathrm{d}t = (\lambda_1 v)|_{t=T} - (\lambda_1 v)|_{t=0} - \int_0^T \frac{\partial \lambda_1}{\partial t} v \mathrm{d}t \tag{5.15}$$

$$\int_\Omega \lambda_1 \omega \Delta v \mathrm{d}\boldsymbol{x} = \int_\Omega \omega \Delta \lambda_1 v \mathrm{d}\boldsymbol{x} + \int_{\partial\Omega} \omega\lambda_1 \frac{\partial v}{\partial \boldsymbol{n}} - \omega v \frac{\partial \lambda_1}{\partial \boldsymbol{n}} \mathrm{d}S \tag{5.16}$$

Substituting (5.15) and (5.16) to equation (5.14), we obtain:

$$\begin{aligned} \frac{\partial L}{\partial I} v = &\int_\Omega \left(I|_{t=T} - B(\boldsymbol{x})\right) v|_{t=T} \mathrm{d}\boldsymbol{x} - \int_\Omega \int_0^T \left(\frac{\partial \lambda_1}{\partial t} v + \omega\Delta\lambda_1 v\right)\mathrm{d}\boldsymbol{x}\mathrm{d}t \\ &+ \int_\Omega \lambda_2 v|_{t=0} + (\lambda_1 v)|_{t=T} - (\lambda_1 v)|_{t=0} \mathrm{d}\boldsymbol{x} \\ &+ \int_{\partial\Omega}\int_0^T \lambda_3 \left(\frac{\partial v}{\partial \boldsymbol{n}}\right) - \omega\lambda_1 \frac{\partial v}{\partial \boldsymbol{n}} + \omega v \frac{\partial \lambda_1}{\partial \boldsymbol{n}} \mathrm{d}S\mathrm{d}t \end{aligned} \tag{5.17}$$

Based on (5.17), it can be concluded that $\frac{\partial L}{\partial I}v$ is equal to zero for any v if following conditions are satisfied by the multipliers $\lambda_1, \lambda_2, \lambda_3$:

$$\frac{\partial \lambda_1}{\partial t} + \omega \Delta \lambda_1 = 0 \quad \text{on} \quad \Omega \times (0,T), \tag{5.18}$$

$$\lambda_1|_{t=T} - B(\boldsymbol{x}) + I|_{t=T} = 0 \quad \text{on} \quad \Omega, \tag{5.19}$$

$$\frac{\partial \lambda_1}{\partial \boldsymbol{n}} = 0 \quad \text{on} \quad \partial\Omega \times (0,T), \tag{5.20}$$

$$\lambda_2 - \lambda_1|_{t=0} = 0 \quad \text{on} \quad \Omega, \tag{5.21}$$

$$\lambda_3 - \omega\lambda_1 = 0 \quad \text{on} \quad \partial\Omega \times (0,T). \tag{5.22}$$

These conditions state the relation between λ_2, λ_3 and λ_1 in a form of PDE with final and boundary condition. The PDE for λ_1 is similar to the original diffusion equation solved for I in the blurring process. The final time condition (5.19) can be reformulated to initial condition using following time-reverting substitution: $\tau = T - t$. For the simplicity of notation, function$\tilde{\lambda}_1(\boldsymbol{x}, \tau) = \lambda_1(\boldsymbol{x}, T-t)$ will be denoted by $\lambda_1(\boldsymbol{x}, \tau)$ in the following equations. Substituting the new variable τ, the PDE for λ_1 reads:

$$\begin{aligned} \frac{\partial \lambda_1}{\partial \tau} - \omega \Delta \lambda_1 = 0 \quad &\text{on} \quad \Omega \times (0,T), \\ \lambda_1|_{\tau=0} = B(\boldsymbol{x}) - I|_{\tau=0} \quad &\text{on} \quad \Omega, \\ \frac{\partial \lambda_1}{\partial \boldsymbol{n}} = 0 \quad &\text{on} \quad \partial\Omega \times (0,T). \end{aligned} \tag{5.23}$$

We note that the existence of strong solution of this adjoint problem is not guaranteed. However, if these conditions for $\lambda_1, \lambda_2, \lambda_3$ are satisfied, the derivative of loss function J with respect to the parameter θ is in θ^* and direction s reduced to:

$$J'(\theta^*)[s] = L'(\theta^*)[s] = \frac{\partial L}{\partial \theta}[s] = -\int_\Omega \lambda_2 s \mathrm{d}\boldsymbol{x}. \tag{5.24}$$

Finally, let us summarize the adjoint approach to computing derivative of loss function J:

1. Solve the primary PDE (5.8) for I.
2. Solve the adjoint PDE (5.23) for λ_1.
3. Compute $\lambda_2 = \lambda_1|_{\tau=T}$ as given by (5.21).
4. Substitute to (5.24) and evaluate $J'(\theta^*)[s]$.

5.4 Numerical solution

5.4.1 Spatial discretization, approximation of spatial derivatives and integrals

For the numerical solution, the image function $I : \Omega \to \mathbb{R}$ is approximated by a grid function $I_h : \Omega_h \to \mathbb{R}$. First, we define Ω_h – the spatial discretization of square domain $\Omega = [0,1] \times [0,1]$:

$$\Omega_h = \{[h/2 + ih, h/2 + jh] \mid i = 0, .., N-1, j = 0, .., N-1\}, \tag{5.25}$$

where N is the number of grid points in each direction and $h = 1/N$ is the spatial step. The nodes of grid Ω_h are denoted by $x_{i,j},\ i = 0, .., N-1, j = 0, .., N-1$. The grid function I_h is

defined only in nodes $x_{i,j}$. Function I_h is fully determined by the values in $N \times N$ nodes of grid Ω_h:

$$I_h = \sum_{i=0}^{N-1} \sum_{j=0}^{N-1} I_{i,j} \chi(x_{i,j}), \tag{5.26}$$

where $I_{i,j}$ denotes the function value and χ is the characteristic function of point $x_{i,j}$. The same approximation and notation is used for all image functions used in Section (5.3). Namely, the blurred image B is approximated by the discrete function B_h, and the initial image function I_0 is approximated by grid function $I_{0,h}$.

In this work, the adjoint equation (5.23) is numerically solved on the same grid as the primary equation (5.8). Therefore, the adjoint function λ_1 is also approximated by discrete function $\lambda_{1,h} : \Omega_h \to \mathbb{R}$. Both PDEs are also solved using the same method. The spatial derivatives in both equations are first discretized, and the resulting ordinary differential equations are solved by the explicit Euler scheme. In equation (5.8), term ΔI is discretized using the second-order central finite difference:

$$\Delta I(x_{i,j}) \approx \frac{I_h(x_{i-1,j}) - 2I_h(x_{i,j}) + I_h(x_{i+1,j})}{h^2} + \frac{I_h(x_{i,j-1}) - 2I_h(x_{i,j}) + I_h(x_{i,j+1})}{h^2}.$$

In the adjoint equation (5.23), term $\Delta\lambda_1$ is treated analogically.

Due to approximation (5.26), optimizing θ is reduced to finding optimal values $\theta_{i,j}$ $i = 0, .., N, j = 0, .., N$. Derivative of the loss function J with respect to $\theta_{i,j}$ is obtained based on equation (5.24) using a piece-wise constant interpolation:

$$\frac{\partial J}{\partial \theta_{i,j}} \approx -\sum_{k=0}^{N-1} \sum_{l=0}^{N-1} h^2 \lambda_{2,k,l} \chi(x_{k,l}) \chi(x_{i,j}) = -h^2 \lambda_{2,i,j}. \tag{5.27}$$

5.4.2 Numerical algorithm

The minimization problem (5.11) is solved iteratively using ADAM optimization method [41]. The initial guess for θ_h is based on the blurred image ${\theta_h}^0 = B_h$. The k-th iteration of the algorithm has the following form:

1. Solve discretized PDE (5.8) with initial condition $I_{0,h} = {\theta_h}^k$.
2. Solve discretized adjoint PDE (5.23) for $\lambda_{1,h}$.
3. Compute $\lambda_{2,h} = \lambda_{1,h}|_{\tau=T}$ based on (5.21).
4. Compute $\frac{\partial J}{\partial \theta^k_{i,j}}$, $i = 0, .., N_1 - 1, j = 0, .., N_2 - 1$ based on (5.27).
5. Compute θ^{k+1} using ADAM based on $\frac{\partial J}{\partial \theta^k_{i,j}}$, $i = 0, .., N_1 - 1, j = 0, .., N_2 - 1$ and θ^k.

5.5 Experimental results

In this section, we present the results of the proposed deblurring method. The blurred images are generated as a solution of diffusion equation (5.8). The parameters used to generate the blurred images are $T = 2.0 \cdot 10^{-5}$ and three values of diffusion coefficient $\omega = 0.25$, $\omega = 0.5$, $\omega = 0.75$. For the numerical solution of equations (5.14) and (5.23), following parameters

were used: $N = 320$, $\tau = 10^{-6}$. In the optimization algorithm, the convergence criterion of $\left(\sum_{i=0}^{N_1-1}\sum_{j=0}^{N_2-1}\left(\frac{\partial J}{\partial\theta_{i,j}}\right)^2\right)^{1/2} < 10^{-9}$ was used.

The input image I_0 and the blurred images are shown in Figure 5.1. The diffusion coefficient used to generate the blurred images is indicated in the subscript B_ω. The estimation of the original image θ, based on the blurred images $B_{0.25}$, $B_{0.5}$, $B_{0.75}$ is shown in Figure 5.2. The norms of difference between the original, blurred, and reconstructed images are provided in Table 5.1. Norm $\|\cdot\|_{2,h}$ is defined using notation for discretized functions used in (5.26):

$$\|I_0 - B\|_{2,h} = \sqrt{\sum_{i=0}^{N}\sum_{j=0}^{N}(I_{0,i,j} - B_{i,j})^2}. \tag{5.28}$$

(a) I_0 **(b)** $B_{0.25}$ **(c)** $B_{0.5}$ **(d)** $B_{0.75}$

Figure 5.1: The original mage I_0 and the three blurred images generated as a solution of equation (5.14). The values of diffusion coefficient with ω equal used in (5.14) are indicated in the subscript B_ω.

Table 5.1 shows, that the difference between the original image I_0 and the reconstruction increases with increasing diffusion coefficient ω. This can be also observed in Figure 5.2. While the reconstruction in Figures 5.2a and 5.2b are very similar to the original image I_0, artifacts are visible in image reconstructed from $B_{0.75}$, especially around the edges.

(a) θ reconstructed from $B_{0.25}$ **(b)** θ reconstructed from $B_{0.5}$ **(c)** θ reconstructed from $B_{0.75}$

Figure 5.2: The result of optimization algorithm for θ. The experiment was performed for blurred images $B_{0.25}$, $B_{0.5}$, $B_{0.75}$.

(a) θ reconstructed from $B_{0.25}$ **(b)** θ reconstructed from $B_{0.5}$ **(c)** θ reconstructed from $B_{0.75}$

Figure 5.3: The details of image reconstructed from blurred images $B_{0.25}$, $B_{0.5}$, $B_{0.75}$.

ω	$\|I_0 - B\|_{2,h}$	$\|I_0 - \theta\|_{2,h}$
0.25	10.85	0.84
0.5	15.7	3.23
0.75	18.67	6.54

Table 5.1: The norm of difference of the original image I_0, the blurred image B and the reconstructed image θ. The experiment was performed for three levels of the blur controlled by the diffusion coefficient ω.

5.6 Conclusions

The adjoint formulation can be used to solve the inverse diffusion equation. First, the adjoint equation was derived. Subsequently, the algorithm for the solution of the inverse heat equation, which utilizes the solution of the adjoint equation, was presented.

The proposed approach was successfully used in the problem of image deblurring. In the future, the differences between the presented method and existing approaches for image deblurring should be investigated. This might lead to finding a context in which is approach might be advantageous.

Personal contribution

The author derived the adjoint problem for the diffusion equation, implemented the solver and performed the presented experiment on blurred images.

Estimation of T_1 relaxation time from cardiac MRI data

6

6.1 Introduction

In this study, we propose a two-stage approach to tissue parameter estimation based on MRI data that attempts to address some of the problems outlined in Section 1. We illustrate the proposed method on the problem of estimating the T_1 relaxation time from cardiac MR image series acquired by the standard Modified Look-Locker Inversion recovery technique (MOLLI) [53] and demonstrate some advantages of such a combined approach.

This Chapter starts with Section 6.1.2 in which the mathematical models with different levels of complexity used for T_1 relaxation time estimation are introduced. Subsequently, we describe how some aspects of the previously published models are combined in the proposed method.

In Section 6.2, the building blocks of the proposed method are described in detail. First, the mathematical model of the MOLLI sequence based on Bloch equations is described in Subsection 6.2.1. In Subsection 6.2.3, we describe the use of the imaging model in the training of NN, used in the first stage of the estimation process. In Subsection 6.2.2, we describe how the generic model of the MOLLI sequence is turned into a patient- and measurement-specific model used in the second stage of T_1 estimation, which is described in Subsection 6.2.4. Finally, the incorporation of the regularization term is described in Subsection 6.2.5. In Section 6.3, we provide the parameters of the synthetic, phantom, and in-vivo MRI data used to validate the proposed method. Finally, the results of the proposed method on the three types of data are presented in Section 6.2.5.

6.1.1 Tissue magnetization

We start this section with a simplified introduction to the main principles of nuclear magnetic resonance (NMR). NMR utilizes the magnetic properties of atomic nuclei and their interaction with an external magnetic field. Nuclei with different numbers of protons and neutrons, such as hydrogen nuclei, exhibit magnetic momentum $\boldsymbol{m}_i$. In a volume of tissue containing hydrogen atoms, the macroscopic magnetic momentum can be defined as a sum of contributions of all nuclei in that volume: $\boldsymbol{M} = \sum_i \boldsymbol{m}_i$.

Under normal conditions, the orientation of $\boldsymbol{m}_i$ is random, and therefore the macroscopic magnetization $\boldsymbol{M} = \boldsymbol{0}$. In an external homogeneous magnetic field with strength $\boldsymbol{B}_0$, individual momenta $\boldsymbol{m}_i$ align to direction parallel or antiparallel with $\boldsymbol{B}_0$. The parallel orientation represents a lower energy state. Therefore, the majority of momenta take this orientation. Cumulatively, this aligning creates a non-zero macroscopic magnetization vector $\boldsymbol{M}$. A diagram of the alignment of m_i in normal conditions and in an external magnetic field is shown in Figure 6.1.

We denote the component of $\boldsymbol{M}$ parallel with $\boldsymbol{B}_0$ by $\boldsymbol{M}_{\parallel}$ (longitudinal magnetization) and the

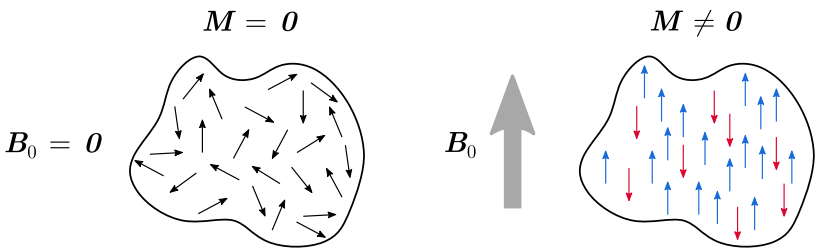

Figure 6.1: Diagram of macroscopic magnetization of given volume under normal conditions and in external magnetic field $\boldsymbol{B}$.

component perpendicular to $\boldsymbol{B}_0$ by $\boldsymbol{M}_\perp$ (transverse magnetization), i.e. $\boldsymbol{M} = \boldsymbol{M}_\parallel + \boldsymbol{M}_\perp$. Only the transverse component $\boldsymbol{M}_\perp$ generates a detectable signal. The imaging process, therefore, requires manipulation with $\boldsymbol{M}$ that would result in non-zero $\boldsymbol{M}_\perp$. The manipulation typically involves the application of an energy pulse – radiofrequency pulse (RF). In the macroscopic point of view, the effect of such a pulse is a rotation of $\boldsymbol{M}$ away from the direction parallel with $\boldsymbol{B}_0$ and therefore formation of non-zero $\boldsymbol{M}_\perp$ and reduction of $\boldsymbol{M}_\parallel$.

After the excitation, the magnetization vector re-aligns with $\boldsymbol{B}_0$ in a process called relaxation. During the relaxation, the magnitude of $\boldsymbol{M}_\parallel$ increases to its original value, while the magnitude of $\boldsymbol{M}_\perp$ decreases to $\boldsymbol{0}$. Both processes are described by the following equations:

$$\|\boldsymbol{M}_\parallel(t)\| = M_0(1 - e^{-\frac{t}{T_1}}), \tag{6.1}$$

$$\|\boldsymbol{M}_\perp(t)\| = M_0 e^{-\frac{t}{T_2}}, \tag{6.2}$$

where M_0 is the initial magnitude of vector $\boldsymbol{M}$. The T_1 relaxation time controls the rate at which the magnitude of longitudinal magnetization $M_\parallel$ returns to initial (equilibrium) value M_0. Similarly, the T_2 relaxation time controls the rate at which the magnitude of $M_\perp$ decreases to zero. The diagram of $\boldsymbol{M}$ in the initial state, after excitation by RF pulse and during the relaxation process, is shown in Figure 6.2.

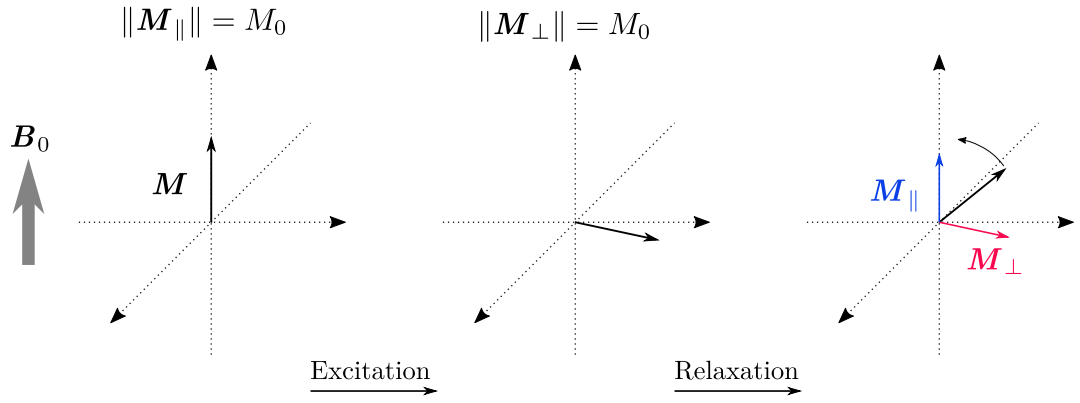

Figure 6.2: Diagram of magnetization vector $\boldsymbol{M}$ in the initial orientation (aligned with $\boldsymbol{B}$) after excitation and during the relaxation.

In magnetic resonance imaging (MRI), the intensity of the given pixel is given by the magnitude of $\boldsymbol{M}_\perp$. In order to create an image, the signal also needs to be localized in space.

This is done by superimposing magnetic field gradients on the uniform magnetic field $\boldsymbol{B}_0$. The steps of excitation and signal detection are repeated until a sufficient amount of information is collected.

6.1.2 Background to T_1 estimation

The process of longitudinal tissue relaxation in nuclear magnetic resonance, introduced in the previous section, can be described by a phenomenological model based on an exponential function with the time constant T_1:

$$w(t) = A - Be^{-\frac{t}{T_1}}.$$

The applicability of this model in cardiac MRI is limited due to several factors. In particular, cardiac MRI applications require the repetition time (TR) being significantly lower than the actual longitudinal relaxation of the myocardium due to acquisition in breath-hold. This results in incomplete recovery of longitudinal magnetization. The relaxation curve is also corrupted by the manipulation of the magnetization vector during the acquisition. These factors lead to an underestimation of the T_1 relaxation time. Therefore, a two-step estimation of T_1 is typically used. First, the apparent relaxation time $T_1^\star$ is estimated using the standard three-parameter fitting of the function $A - Be^{-\frac{t}{T_1^\star}}$. Then, the actual relaxation time T_1, $T_1 > T_1^\star$, is computed according to the correction formula

$$T_1 = \left(\frac{B}{A} - 1\right) T_1^\star, \tag{6.3}$$

designed with the assumption of a continuous FLASH (fast low-angle shot) gradient echo readout [19].

Sampling and fitting the exponential curve is a fast and efficient way of estimating T_1. However, the result may be influenced by a number of factors, which are not completely considered in the phenomenological model even when adding the correction step. These may be for instance the type of readout or non-constant TR due to varying heart rate. Furthermore, the FLASH-sequence-derived correction formula (6.3) applied for the MOLLI data (with balanced steady-state free precession readout) introduces yet another bias.

Several alternatives to this phenomenological model are presented in the following section.

6.1.3 Alternative approaches to T_1 estimation

Alternatively to the phenomenological models, a biophysical approach can be employed. In our problem, this would be the application of the mathematical model of the relaxation process described by the Bloch equations – Bloch simulator [6]. Recently, several ways of integrating a mathematical model of the MOLLI imaging sequence have been pursued. We now list several methods relevant to our own approach, which we describe at the end of this section.

- In [27], the use of the Bloch simulator to generate synthetic data that would mimic the measured data of phantoms and human volunteers, was examined. The standard two-step estimation of the relaxation time T_1 by fitting the phenomenological exponential $T_1^\star$ and applying the correction formula (6.3) was to estimate T_1 from the measured data and from the synthetic data generated by the Bloch simulator. The work showed the equivalency of the parameters estimated from the real and synthetic data. Furthermore, it was demonstrated that the Bloch equation-based simulations can be used to analyze various effects in the standard two-step estimation of T_1, e.g. varying flip angle, maximal inversion time or the actual encoding schemes for data acquisition.

- In [85] the three-parameter fit was avoided altogether. In phantom and *in vivo* study, the authors showed that the estimation of T_1 from a series of MOLLI images can be improved by comparing the signals with a large set of possible measurement results generated by Bloch simulations with different tissue parameters.

- In study,[73] the two types of estimation methods were compared. The representative of the first approach was the standard three-parameter fit in its modified version named Inversion Group (IG) fitting [79]. In the IG fitting, the three parameters were allowed to vary for each "inversion group" – signals acquired between two subsequent inversion pulses. The second approach was based on estimating T_1 by pixel-wise matching the simulated signal to the measured signal using the least squares algorithm.

- The comparison on phantoms by [73] demonstrated that estimating T_1 by directly matching the measured and generated signal has superior accuracy compared to the three-parameter-fit methods. However, in some cases, these methods showed a lower precision. The authors speculate that this might be caused by a higher sensitivity to noise. The best approach found in [73] was based on BLESSPC (Bloch equation simulation with slice profile correction) and a subsequent inversion of the model by minimizing the mean square error between the simulated and measured signal for each pixel.

- In BLESSPC [75], the minimization was performed by using the Levenberg-Marquardt algorithm The method was shown to suffer from a long computation time in some cases. Therefore, [72] presented an approach incorporating the original BLESSPC method with NN. In this work, a deep convolutional NN with an input layer containing the measured signal and the acquisition time stamps were used. The T_1 relaxation time was predicted pixel-wise. It was shown that the NN trained on synthetic data obtained similar estimations as the original method in a much shorter time.

- The presented approaches also differ in the used variants of Bloch simulators. The set of free parameters that need to be optimized, besides the T_1, therefore also differ. For instance, [74] in the method InSiL (Instantaneous Signal Loss simulation) additionally estimated the initial magnetization M_0 and the factor of instantaneous signal loss in longitudinal magnetization. In [75], method BLESSPC was used to estimate the initial magnetization M_0 together with an apparent flip angle, to give some examples.

In the present work, we combine ML with biophysical modeling to benefit from both. Similarly to [72], a mathematical model of the MOLLI sequence is used to generate a sufficient amount of synthetic datasets for training an NN. It is trained by using various combinations of cardiac cycle durations, inversion times, flip angles, tissue relaxation parameters, etc. The NN is not fully specific for a single patient and a single type of acquisition, and can therefore be trained beforehand. It is used as a black-box model that produces a fast *first-stage* estimate of the parameters of T_1, T_2 relaxation times, tissue magnetization M_0 and the actual value of flip angle α in the tissue. Then, the parameters of the given measurement are substituted into the mathematical model of MOLLI. This "patient- and measurement-specific" model is used for the final fine-tuning of the estimated parameters by NO while using the NN-based first-stage estimate as an initial guess. The *second-stage* of parameter estimation can additionally include various regularization constraints (e.g. spatial, physical, or physiological). The diagram of the proposed approach is shown in Figure 6.3.

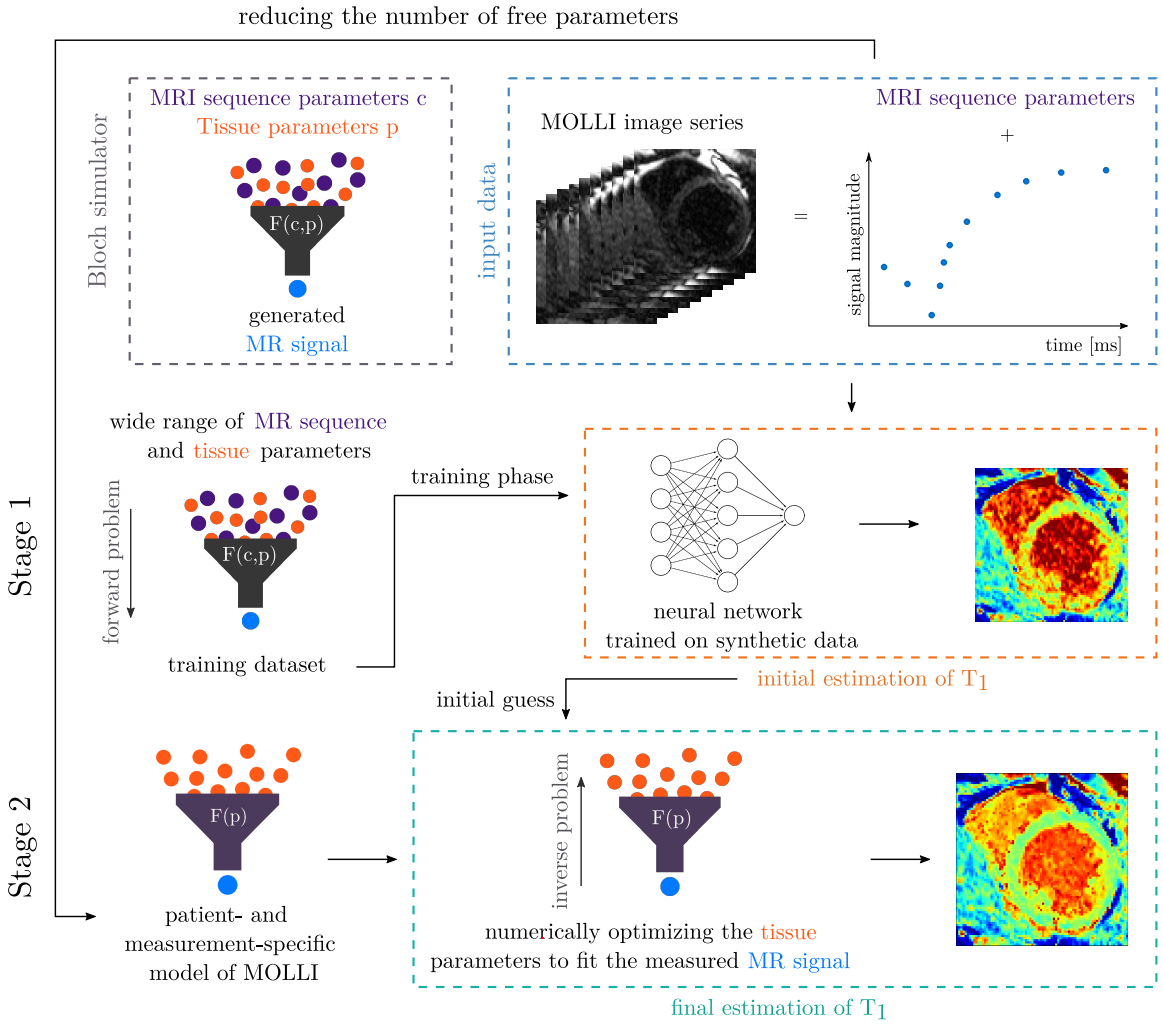

Figure 6.3: Diagram of the proposed two-stage approach to T_1 relaxation time estimation.

6.2 The proposed two-stage method

In this work, the estimation of T_1 relaxation time from the conventional 5-3-3 MOLLI MR images (see [53] and schematics in Figure 6.4) is formulated as an inversion problem. The MOLLI sequence provides an image series, where n values of intensity ($n = 11$ for the 5-3-3 MOLLI sequence) are available for each pixel. These values may be represented by an n-dimensional vector $\boldsymbol{s}$. Let us consider a mathematical model F of this imaging sequence, which simulates the signal $\hat{\boldsymbol{s}}$, i.e.

$$F(\boldsymbol{c}, \boldsymbol{p}) = \hat{\boldsymbol{s}}, \tag{6.4}$$

where vector $\boldsymbol{c}$ consists of the fixed parameters (typically given by the imaging sequence) and vector $\boldsymbol{p}$ is composed of the free parameters (representing the characteristics of the imaged tissue, one of them being the relaxation time T_1).

In order to estimate $\boldsymbol{p}$, we formulate the following minimization problem

$$\min_{\boldsymbol{p}} l(F(\boldsymbol{c}, \boldsymbol{p}), \boldsymbol{s}), \tag{6.5}$$

where l is a loss function used to evaluate the difference between the measured values $\boldsymbol{s}$ and the

values $\hat{\boldsymbol{s}}$ generated by the model F. Next, the model of imaging sequence F, the loss function l, and the minimization method are described.

6.2.1 Mathematical model of the imaging sequence

The mathematical model of the 5-3-3 MOLLI sequence is based on an analytical solution of the Bloch equations [7], solving for tissue magnetization vector $\boldsymbol{M}(t) = (M_x(t), M_y(t), M_z(t))$:

$$\begin{aligned}
\frac{\mathrm{d}\ M_x(t)}{\mathrm{dt}} &= \gamma(\boldsymbol{M}(t) \times \boldsymbol{B}(t))_x - \frac{M_x(t)}{T_2}, \\
\frac{\mathrm{d}\ M_y(t)}{\mathrm{dt}} &= \gamma(\boldsymbol{M}(t) \times \boldsymbol{B}(t))_y - \frac{M_y(t)}{T_2}, \\
\frac{\mathrm{d}\ M_z(t)}{\mathrm{dt}} &= \gamma(\boldsymbol{M}(t) \times \boldsymbol{B}(t))_z - \frac{M_z(t) - M_0}{T_1}.
\end{aligned} \tag{6.6}$$

The set of equations (6.6) describes the relaxation process of a magnetization vector $\boldsymbol{M}$ with the tissue characteristics T_1, T_2 corresponding to the time constants of the longitudinal (z) and transverse (xy) component relaxation, γ being the gyromagnetic ratio of ^{1}H nuclei ($\omega_0 = \gamma B_0$ being the Larmor frequency). Under the assumption of a static external magnetic field $\boldsymbol{B}(t) = (0, 0, B_0)$, the system (6.6) is simplified to following system of ODEs:

$$\begin{aligned}
\frac{\mathrm{d}\ M_x(t)}{\mathrm{dt}} &= \omega_0 M_y(t) - \frac{M_x(t)}{T_2}, \\
\frac{\mathrm{d}\ M_y(t)}{\mathrm{dt}} &= -\omega_0 M_x(t)\ - \frac{M_y(t)}{T_2}, \\
\frac{\mathrm{d}\ M_z(t)}{\mathrm{dt}} &= -\frac{M_z(t) - M_0}{T_1},
\end{aligned} \tag{6.7}$$

which has an analytical solution [58]:

$$\begin{aligned}
\boldsymbol{M}(t + \Delta t) = &\begin{pmatrix} \mathrm{e}^{-\frac{\Delta t}{T_2}} & 0 & 0 \\ 0 & \mathrm{e}^{-\frac{\Delta t}{T_2}} & 0 \\ 0 & 0 & \mathrm{e}^{-\frac{\Delta t}{T_1}} \end{pmatrix} \begin{pmatrix} \cos(\omega_0 \Delta t) & \sin(\omega_0 \Delta t) & 0 \\ -\sin(\omega_0 \Delta t) & \cos(\omega_0 \Delta t) & 0 \\ 0 & 0 & 1 \end{pmatrix} \boldsymbol{M}(t) + \\
&\begin{pmatrix} 0 \\ 0 \\ M_0 \left(1 - \mathrm{e}^{-\frac{\Delta t}{T_1}}\right) \end{pmatrix}
\end{aligned} \tag{6.8}$$

We remark that the acquired signal – represented by the output of F in the Equation (6.5) – is associated with the magnitude of the projection of $\boldsymbol{M}$ onto the transverse (xy) plane. The rotation around the z-axis, given by the $\omega_0 \Delta t$ term, is not simulated as it has no effect on the magnitude of the transverse component of $\boldsymbol{M}$.

In the image acquisition model, the relaxation process follows each manipulation with the magnetization vector $\boldsymbol{M}$ by the MRI sequence. The manipulation of the magnetization is governed by the specific sequence parameters incorporated in the model. In general, the manipulation with magnetization vector by a single radiofrequency (RF) pulse with given flip angle alpha ϕ

and duration Δt is simulated as a rotation of $\boldsymbol{M}$ around x-axis:

$$\boldsymbol{M}(t+\Delta t) = \begin{pmatrix} 1 & 0 & 0 \\ 0 & \cos(\phi) & \sin(\phi) \\ 0 & -\sin(\phi) & \cos(\phi) \end{pmatrix} \boldsymbol{M}(t). \tag{6.9}$$

As explained above, the imaging sequence model F (6.4) operates with two types of parameters $\boldsymbol{c}$ and $\boldsymbol{p}$. The measurement-specific parameters $\boldsymbol{c}$ are as follows: *Echo Time (TE);* 11 values of *Inversion Time* (IT); 11 values of RR (time period between consecutive R-waves in ECG, i.e. cardiac cycle duration reciprocal to the heart rate); *Base Resolution (BR); Reference Lines of parallel imaging (RL); Phase Partial Fourier (PPF); and Percent Phase Field Of View (PPW).* From these, the remaining sequence parameters can be computed based on the sequence structure, known from the source code provided by the vendor within the IDEA environment.

Based on the sequence-specific parameters, two additional parameters which control the timing of the imaging sequence are computed:

$$\begin{aligned} L_t =& \frac{1}{2}(BR \cdot PPW + RL) - \frac{1}{2}(1 - PPF) \cdot BR \cdot PPW, \\ L_c =& \frac{1}{2} BR \cdot PPW - \frac{1}{4}(BR \cdot PPW - RL) - \frac{1}{2}(1 - PPF) \cdot \ BR \cdot PPW. \end{aligned}$$

The tissue-specific parameters (vector $\boldsymbol{p}$) are in our problem represented by: T_1 and T_2 relaxation times; and initial tissue magnetization M_0. Furthermore, while the target flip angle α is a parameter of the MRI sequence, the actual tilting of $\boldsymbol{M}$ is not uniform in the imaged domain. In real acquisitions, the effective value of the flip angle is unevenly distributed around this target value. The actual flip angle α in the tissue can therefore be considered as an additional tissue characteristic and the value of α is becoming one of the estimated parameters.

The mathematical model of image acquisition consists of three consecutive main blocks, each containing either 5 or 3 inner units (see Figure 6.4 for details). Each main block starts with an inversion pulse which is followed by 5 or 3 inner units, each consisting of a period of relaxation, five preparatory radiofrequency (RF) pulses, the signal readout, and relaxation. In the first main block, the magnetization vector starts from the initial value $\boldsymbol{M}(0) = (0, 0, M_0)$. In the following blocks, the final $\boldsymbol{M}$ from the previous block is used as a starting value.

As shown in 6.4, the timing of the signal readouts is given primarily by the 11 values of *Inversion Time*. The cardiac-cycle duration RR is only needed to compute the duration of the 3-cardiac-cycles long relaxation between the three main blocks of the sequence. The duration of these cardiac cycles is however not measured and therefore a mean duration $\overline{RR}$ is used. The mean length of the cardiac cycle $\overline{RR}$ is computed as the average of all RR values.

The mathematical model also includes one signal-corrupting effect – the effect of an uneven distribution of flip angle α throughout the slice thickness (excitation profile). The thickness of each imaged voxel is significantly larger than its other two dimensions. For the diagram of the 3D imaged volume and the final 2D image, see Figure 6.5. The effective flip angle is known not to be uniform across a slice thickness [82]. In our work, the flip angle variation is modeled by dividing the virtual volume of imaged tissue into 9 sublayers and assuming the normal distribution of flip angle α with variance σ^2, the original value being in the middle layer. The distribution of the flip angle across the thickness of the imaged layer is shown in Figure 6.5. Similar slice profile correction was used also in [18] and [75]. The simulations are performed for each angle separately and the simulated signal is then averaged.

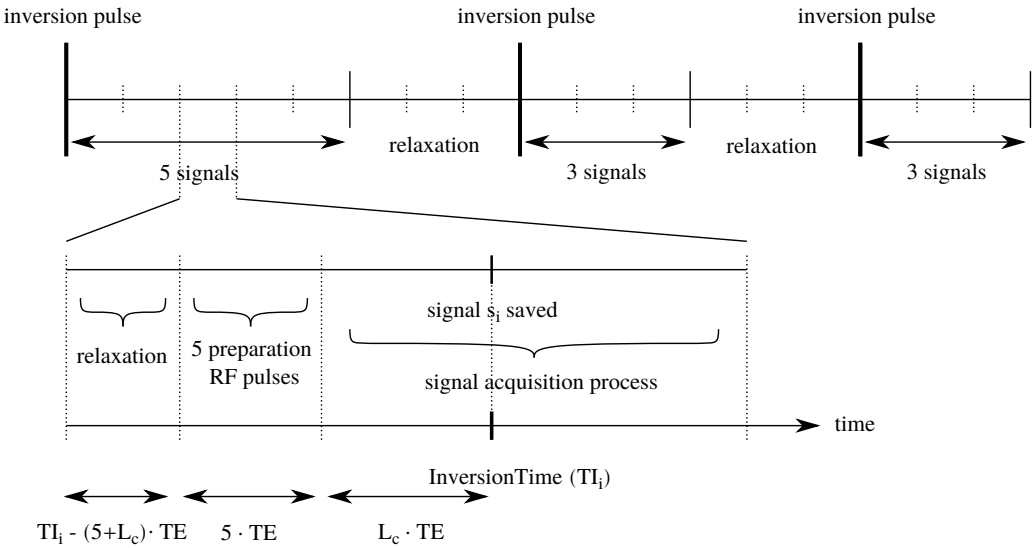

Figure 6.4: The simulation of the MOLLI sequence consists of 3 blocks. Each block consists of 5 or 3 inner units, followed by relaxation (of the duration of 3 cardiac cycles). Each block starts with an inversion pulse, which is simulated by flipping the magnetization vector $\boldsymbol{M}$ by 180° around the x-axis. Each inner unit consists of three steps – relaxation, preparation pulses, and signal acquisition. The timing in i-th inner unit depends on the i-th value of InversionTime and the value of TE. The signal acquisition process consists of L_t radiofrequency (RF) pulses with flip angle $\pm\alpha$, where the signal is generated as the magnitude of the transverse component of $\boldsymbol{M}$ after the L_c-th pulse. This moment needs to correspond to the i-th value of InversionTime (IT_i). Therefore the acquisition starts at time $IT_i - L_c \cdot TE$. The five preparation RF pulses with flip angles $1/10\alpha, -3/10\alpha, 5/10\alpha, -7/10\alpha, 9/10\alpha$ (each simulated as a rotation by given angle around the x-axis) start at time $IT_i - (5 + L_c) \cdot TE$. The remaining time before the preparation pulses is filled with relaxation.

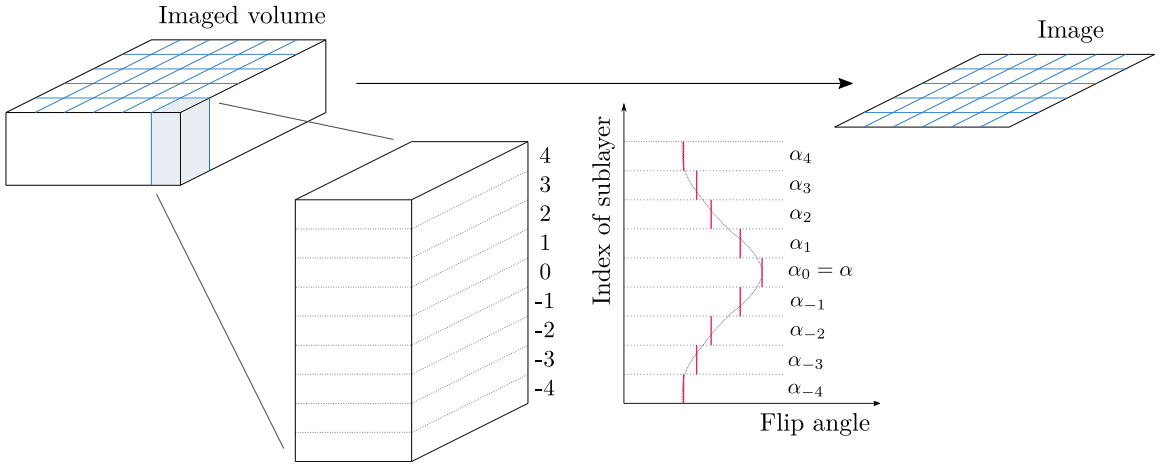

Figure 6.5: Diagram of distribution of the flip angle α in the imaged volume.

6.2.2 Patient- and measurement-specific model

The generic model F of the MOLLI sequence is turned into the patient- and measurement-specific regime $\tilde{F}$ by inputting the known parameter values. Specifically, the values of TE, 11 values of *Inversion Time*, mean RR, L_c, L_t are substituted into the model F. This specified model,

with reduces the number of free parameters, is denoted by $\tilde{F}(\boldsymbol{p})$. The variance of the flip angle through the slice thickness (σ^2), used for signal corruption in the training dataset, is set to zero in model $\tilde{F}$. The impact on the simulated signal $\tilde{\boldsymbol{s}}$ is covered by the remaining free parameters, particularly M_0. The tissue characteristics T_1, T_2, and M_0 and the tissue distribution of flip angle α are the only free parameters of the resulting model $\tilde{F}(\boldsymbol{p})$.

6.2.3 Neural network trained on the synthetic data

The initial estimation of the free parameters $\boldsymbol{p} = (T_1, T_2, M_0, \alpha)$ is obtained by using an NN trained on the model-generated data.

The NN consists of an input layer with 11 neurons, with the values of 11 sampling points of MOLLI sequence; 6 convolution layers with 3×1 kernel and 32 channels; 2×1 maximum pooling layer and two dense layers with 160 and 40 neurons; and the output layers consisting of 4 neurons. Exponential Linear Unit (ELU) activation function [16] was used in all layers.

The ELU activation function $ELU(x) = \begin{cases} x \text{ if } x > 0 \\ (e^x - 1) \text{ if } x \leq 0 \end{cases}$ provides nonlinearity to the NN.

Compared to the frequently used Rectified Linear Unit (ReLU) activation function, ELU takes also negative values, which may lead to a faster convergence, as was shown by [16].

To deal with the different orders of magnitude in the estimated parameters, the following loss function was used to evaluate the difference between the true ($\boldsymbol{p}$) and predicted parameters ($\hat{\boldsymbol{p}}$) in a relative sense:

$$l = \sum_{i=1}^{4} \left(\frac{\boldsymbol{p}_i - \hat{\boldsymbol{p}}_i}{\boldsymbol{p}_i} \right)^2. \tag{6.10}$$

The NN was trained on $1.6 \cdot 10^6$ samples of synthetic MOLLI sequences using the ADAM optimizer [41]. The batch of training samples was generated in each iteration by the model of the MOLLI sequence using a set of parameters randomly generated in the ranges listed in Table 6.1.

6.2.4 Parameter estimation approach combining neural network and numerical optimization

In the first stage, the NN is used to generate the first estimate of $\boldsymbol{p}$. In the second stage, $\boldsymbol{p}$ is optimized to minimize the difference between the measured signal and the signal generated by the model $\tilde{F}$. This leads to a reduced minimization problem

$$\min_{\boldsymbol{p}} l(\tilde{F}(\boldsymbol{p}), \boldsymbol{s}), \tag{6.11}$$

with $\boldsymbol{s}$ being the measured signal.

The optimization problem is not well posed, as a similar relaxation curve can be obtained by different combinations of the free parameters. Examples of such relaxation curves generated by the Bloch simulator are shown in Figure 6.6, using the same set of parameters $\boldsymbol{c}$ and different sets of parameter $\boldsymbol{p} = (T_1, T_2, M_0, \alpha)$. Therefore, optimizing all components of $\boldsymbol{p}$ in the second stage may not increase the accuracy of T_1.

The selection of the loss function l may also affect the accuracy of the estimation. In this work, four types of loss functions were evaluated.

First, the quadratic loss function

$$l_2(\boldsymbol{s}, \tilde{\boldsymbol{s}}) = \sum_{i=1}^{11} (s_i - \tilde{s}_i)^2, \tag{6.12}$$

Table 6.1: The ranges of parameter values were determined with respect to the range of typical values in human tissues and the setting of the scanner used for the validation measurements. The first InversionTime IT_1 was generated randomly in the given range, the other inversion times were computed based on delay Δd, RR and errors e_i as follow: $[IT_1, IT_1 + \Delta d + e_2,\ IT_1 + 2\Delta d + e_3,\ IT_1 + \overline{RR} + e_4,\ IT_1 + \Delta d + \overline{RR} + e_5,\ IT_1 + 2\Delta d + \overline{RR} + e_6,\ IT_1 + 2\overline{RR} + e_6,\ IT_1 + \Delta d + 2\overline{RR} + e_7,\ IT_1 + 2\Delta d + 2\overline{RR} + e_8,\ IT_1 + 3\overline{RR} + e_9, IT_1 + 4\overline{RR} + e_{10}]$. The errors e_i are introduced to simulate the non-constant value of RR in real measurements and thus increase the robustness of the neural network. The effect of non-even distribution was included in the training dataset for the same reason.

Parameter	Values / Ranges	Description
α	$25 - 45$ [°]	flip angle
TE	1 - 2 [ms]	*Echo Time*
$\overline{RR}$	600 - 1200 [ms]	mean duration of the 11 accepted heart beats
RL	36 [.]	*Reference Lines of parallel imaging*
PPF	7/8 [.]	*Phase Partial Fourier*
PPW	0.8 - 0.95 [.]	*Percent Phase Field Of View*
IT_1	$(5 + L_c) \cdot TE$ + (30 - 50)[ms]	first *Inversion Time*
Δd	80 [ms]	*Inversion Time* delay
e_i	(-10) - 10 [ms]	error in i-th *Inversion Time*, $i = 2 : 11$
T_1	180 - 2200 [ms]	relaxation time
T_2	20 - 300 [ms]	relaxation time
M_0	0.025 - 0.95 [.]	z-component of initial magnetization
σ	1.63 - 20 [°]	standard deviation of flip angle distribution

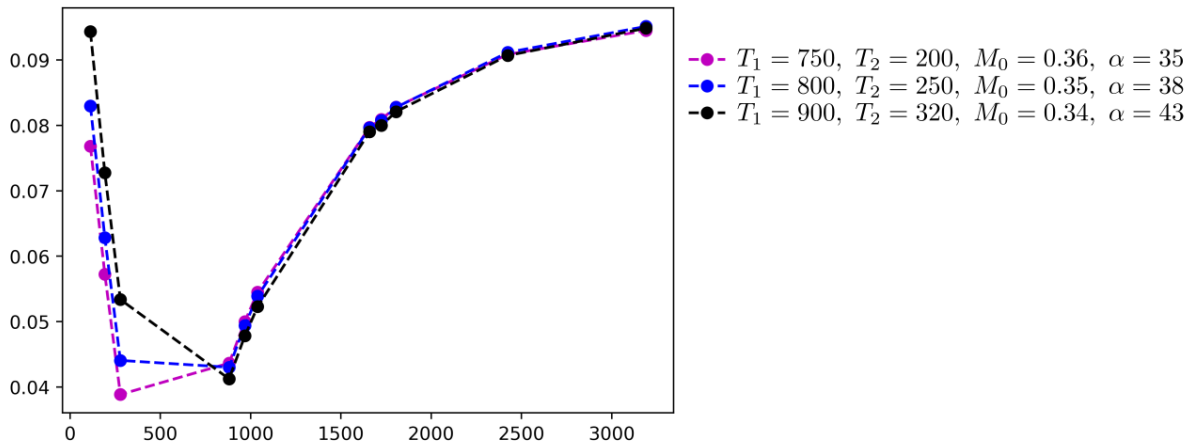

Figure 6.6: Example of three relaxation curves generated by the Bloch simulator.

was used.

Another option is to evaluate the difference between the measured and generated signal in a

relative manner, using the loss function

$$l_{rel}(\boldsymbol{s}, \tilde{\boldsymbol{s}}) = \sum_{i=1}^{11} \left(\frac{s_i - \tilde{s}_i}{s_i} \right)^2, \tag{6.13}$$

where the difference between the signals is normalized by the value of the measured signal. Contrary to l_2, which does not takes into account the difference in the order of magnitude between the values in MOLLI sampling points, l_{rel} does not penalize the mismatch in the sampling points with lower signal values less than the mismatch in the sampling points with higher signal values.

The uneven penalization of misalignment between the sampling points on the exponential relaxation curve may also be limited by using the logarithmic loss function

$$l_{\log}(\boldsymbol{s}, \tilde{\boldsymbol{s}}) = \sum_{i=1}^{11} (\log(s_i) - \log(\tilde{s}_i))^2, \tag{6.14}$$

Last, a loss function assigning different weights to the MOLLI sampling points was used

$$l_w(\boldsymbol{s}, \tilde{\boldsymbol{s}}) = \lambda \left(\sum_{i=1}^{2} (s_i - \tilde{s}_i)^2 + \sum_{i=7}^{11} (s_i - \tilde{s}_i)^2 \right) + \sum_{i=3}^{6} (s_i - \tilde{s}_i)^2. \tag{6.15}$$

In this loss function, 7 values sampled at the beginning and the end of the relaxation curve are assigned with lower weights, compared to the 4 signal values sampled in the middle of the relaxation curve, in order to compensate for the highest level of the signal.

6.2.5 Regularization terms

The variational formulation of problem (6.11) allows to the inclusion of a number of regularization terms.

This leads to the following minimization problem:

$$\min_{\boldsymbol{p}} \left(l(\tilde{F}(\boldsymbol{p}), \boldsymbol{s}) + r(\boldsymbol{p}) \right), \tag{6.16}$$

where l is a loss function defined in Section 6.2.4 and r is the regularization term. In our problem, we consider two types of regularisation terms.

A regularization term ensuring the smoothness of the resulting T_1 map

$$r(T_1) = \lambda_1 \int_\Omega \|\nabla T_1\|^2 \mathrm{d}\boldsymbol{x}, \tag{6.17}$$

is considered, where Ω denotes the domain of the T_1 map. Incorporating this term prevents the spatial gradient from getting a very high value, which would likely indicate a non-physiological sudden change of the estimated tissue characteristics.

6.3 Synthetic and real MRI data

6.3.1 Synthetic data

A dataset of 10,000 synthetic MOLLI image series was generated using combinations of parameter values randomly chosen from the ranges provided in Table 6.1. This dataset was used to compare various optimization approaches.

First, the impact of the second-stage estimation – NO – on the accuracy of the T_1 estimate was evaluated. Specifically, NN was used in the first stage of the estimation to obtain the values of T_1, T_2, M_0, and α. The accuracy of the second stage was evaluated for estimating various combinations of $\boldsymbol{p}$ components (while the remaining components were kept as given by the first-stage NN) and the loss functions (6.12) – (6.15).

The NO stage can be also run without the initialization by NN. In such a case, the initial guess for the parameters T_1, T_2, M_0, α can be based on prior knowledge. In our work, the mean values of the corresponding ranges in Table 6.1 were used. The accuracy of T_1 estimation after the NO initialized by the mean value is compared to the estimate with the initialization given by NN. The final test with the synthetic data is the assessment of the accuracy of T_1 estimate when using the input data corrupted by normally distributed noise.

6.3.2 Phantoms

To validate the proposed T_1 estimation approach, eight phantoms with a wide range of T_1 values were used. The T_1 relaxation values obtained by the inversion recovery turbo spin echo (IR-TSE) sequence were used as the pseudo-ground truth (pGT) values. The results of the proposed two-stage approach were compared with the T_1 estimation from the same MOLLI dataset provided directly by the scanner console and evaluated against the pGT values.

The phantoms were fabricated using a water solution of agar (mass fraction 4.5%) and sodium azide (0.2%). Agar constrains diffusion and azide protects against bacterial decay. This base mixture was filled into eight 50 mL cylindrical test tubes and mixed with a small volume of 10 mmol/L gadolinium contrast agent solution (ProHance, Bracco Imaging Deutschland GmbH, Germany). Thus, a series of phantoms was obtained with the following concentrations of contrast agent: 0.0000, 0.0456, 0.0842, 0.1228, 0.1806, 0.2771, 0.4700 and 1.0487 mmol/L, so as to produce intended T_1 times of: 200, 400, 600, 800, 1000, 1200, 1500 and 2130 ms.

The phantoms were imaged on a 3T MRI scanner (MAGNETOM Vida, Siemens Healthineers, Germany) and on a 1.5T MRI scanner (MAGNETOM Avanto fit, Siemens Healthineers, Germany) using a head coil. All parameters of the measurement are provided in Appendix A.1.

6.3.3 *In vivo* data

Datasets of 15 patients indicated for a cardiac MRI exam were used in this study. The datasets were acquired under the ethical approval number G-14-08-11, in conformance with the 1975 Declaration of Helsinki. All patients signed an informed consent approved by the institution's ethical committee. The MRI acquisition were performed on a 3T MRI scanner (MAGNETOM Vida, Siemens Healthineers, Germany) and on a 1.5T MRI scanner (MAGNETOM Avanto fit, Siemens Healthineers, Germany).

All parameters of the measurement are provided in Appendix A.2. The values of *Inversion time* and *RR* in the pre-contrast and post-contrast scan for each subject are shown in Table A2 and Table A3.

The MOLLI data were acquired prior to and approximately 10 minutes after administering a 1 mmol/ml solution of gadobutrol (0.15 ml/kg according to patient's weight).

6.4 Results

6.4.1 Synthetic data study

In the synthetic data study, the accuracy of the estimate can be evaluated against the known true values of the parameters, used to generate the dataset. True values of parameters

are denoted by $T_1^{GT}, T_2^{GT}, M_0^{GT}, \alpha^{GT}$; the first-stage estimations obtained by NN are denoted $T_1^{NN}, T_2^{NN}, M_0^{NN}, \alpha^{NN}$; and the second-stage estimations obtained by NO are denoted $T_1^{NO}, T_2^{NO}, M_0^{NO}, \alpha^{NO}$.

We investigate three problems:

1. which loss function should be used and which parameters should be optimized in the second stage in order to obtain the highest accuracy in T_1 estimation,

2. how the initialization by the NN effects the second stage,

3. how are the results effected by noise in the input data.

Selection of loss function and parameters optimized in the second stage

In order to evaluate the accuracy of T_1 estimation on the synthetic dataset, we define the following mean relative loss function:

$$\bar{l}_{\text{estim}} = \frac{1}{N} \sum_{i=1}^{N} \frac{\left| T_{1,i}^{GT} - T_{1,i}^{\text{estim}} \right|}{T_{1,i}^{GT}}, \tag{6.18}$$

where the subscript i, denotes the i-th item of the dataset, N denotes the total number of items in the dataset and estim stands for NN or NO.

The impact of the second-stage estimation – NO stage – on the accuracy of the T_1-estimate was evaluated for 6 combinations of the optimized parameters and loss functions l_2, l_w, l_{rel} and l_{ln}. The weighted loss function was used with $\lambda = 0.25$ The problem (6.11) was solved by the limited memory BFGS method for large-scale optimization, l-BFGS [47]. The initial guess for the NO was given by the result of first-stage NN estimation in all cases. The accuracy of estimated values with respect to ground truth T_1^{GT} is assessed using loss function $\bar{l}$. The percentage decrease of mean relative loss function $\bar{l}$, after the second stage with respect to the accuracy of the first stage is shown in Table 6.2.

Table 6.2: The table shows the percentage decrease of the mean relative error (6.18) between the first and second stage of estimation, that is $100 \cdot (\bar{l}_{\text{NN}} - \bar{l}_{\text{NO}})/(\bar{l}_{\text{NN}})$. The second stage of optimization was performed for 6 groups of optimized parameters and loss functions l_2, l_w, l_{rel} and l_{ln}

	Loss function used in the second stage			
Optimised parameters	l_2	l_w	l_{rel}	l_{ln}
T_1	15.47	27.02	40.88	34.81
T_1, T_2	43.63	30.97	33.45	30.23
T_1, M_0	73.18	62.00	50.13	48.18
T_1, α	0.01	0.00	0.32	34.81
T_1, T_2, M_0	86.32	86.14	65.53	63.48
T_1, T_2, M_0, α	0.04	0.09	0.26	0.74

The largest decrease of mean relative error in the T_1 estimate after NO was achieved when optimizing the combination of parameters T_1, T_2, M_0 using the quadratic loss function l_2. A similar decrease was obtained when using the weighted loss function l_w and the same set of parameters. Optimizing the parameter α in the second stage is generally the least beneficial for the accuracy of the T_1 estimate.

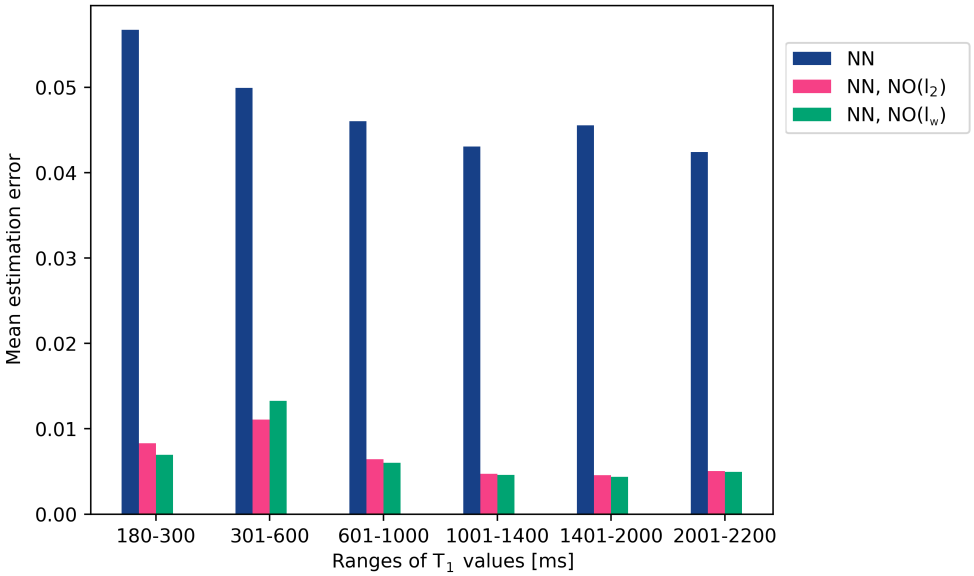

Figure 6.7: The range of T_1 values (180 - 2200 ms) is divided into 6 sub-intervals. The mean relative error in the T_1 estimation (6.18) is evaluated in each sub-interval. The three compared estimations are: prediction of the NN (denoted NN), the result of the NO optimization using loss function l_2 (denoted NN, NO(l_2)), the result of the NO optimization using loss function l_w (denoted NN, NO(l_w)).

The mean relative error $\bar{l}_{\mathrm{NO}}$ in the two most effective settings – i.e. T_1, T_2, M_0 optimized using either the quadratic or the weighted loss function – is in addition evaluated in 6 intervals of T_1 values. Figure 6.7 shows that incorporating the second-stage estimation based on NO decreases the mean estimation error in the whole range of T_1. The largest error in NN prediction is obtained for the T_1 values in the range 180-300 ms. The largest error in the NO stage is obtained in the range 180-300 ms for l_2 and 301-600 ms for l_w.

Conclusion

Largest decrease in T_1 estimation error was achieved when:

- parameters T_1, T_2, M_0 are optimized
- α is fixed on the value estimate in the first stage
- loss functions l_2 and l_w are used

Selection of initialization for the second stage

The NO stage of estimation in this setting is further evaluated with respect to various initializations: (A) all parameters initialized by the NN prediction; (B) by the mean values based

on Table 6.1, i.e. $T_1 = 1190.0,\ T_2 = 160.0,\ M_0 = 0.4875,\ \alpha = 35.0$; (C) a combined type of initialization (T_1, T_2, M_0 initialized by the NN and α by the mean value 35.0).

The mean error in T_1 estimation and the mean number of iterations needed to reach the convergence criterion (gradient magnitude $< 10^{-10}$) are shown in Table 6.3. Initializing all parameters by the NN prediction was shown to be the most efficient. The initialization by mean values provided significantly larger errors than the NN-initialization. The combined initialization led to an almost identical number of iterations and a slightly higher error in T_1 estimation than if fully initialized by NN.

Table 6.3: Mean relative error $\bar{l}$ evaluated on the dataset of 10,000 synthetic samples of MOLLI. The parameters T_1, T_2, M_0 are estimated in the NO phase, using the quadratic and weighted loss functions (l_2, l_w), while the parameter α remains fixed. In the NO, the parameters are initialized by:
Setting A: $T_1^{NN},\ T_2^{NN},\ M_0^{NN};\ \alpha = \alpha^{NN}$;
Setting B: $T_1 = 1190.0,\ T_2 = 160.0,\ M_0 = 0.4875;\ \alpha = 35.0$ (mean values);
Setting C: $T_1^{NN}, T_2^{NN}, M_0^{NN};\ \alpha = 35.0$.
The mean number of iterations indicates how many iterations of the NO method were needed to reach the convergence criterion.

	Loss function used in NO	Mean relative error $\bar{l}$	Mean number of iterations
Setting A	l_2	$6.29 \cdot 10^{-3}$	38.57
	l_w	$6.37 \cdot 10^{-3}$	36.43
Setting B	l_2	$1.43 \cdot 10^{-1}$	53.03
	l_w	$2.67 \cdot 10^{-1}$	52.28
Setting C	l_2	$7.20 \cdot 10^{-3}$	38.95
	l_w	$7.41 \cdot 10^{-3}$	36.62

The scatter plots of the predicted and true values for the three settings are shown in Figure 6.8. Similarly to Table 6.3, the figure shows that the NN initialization is superior to the mean value initialization. Especially for T_1 values below 500 ms, the NO stage does not provide correct results when initialized by the mean values. The figure also shows that on the synthetic datasets, the loss function l_2 provides higher accuracy than l_w (particularly for short T_1 relaxation times).

Conclusion

It was shown that the use of NN as the initialization for the second stage:

- increases the accuracy of T_1 estimation
- decreases the number of iterations needed to reach the convergence in the second stage

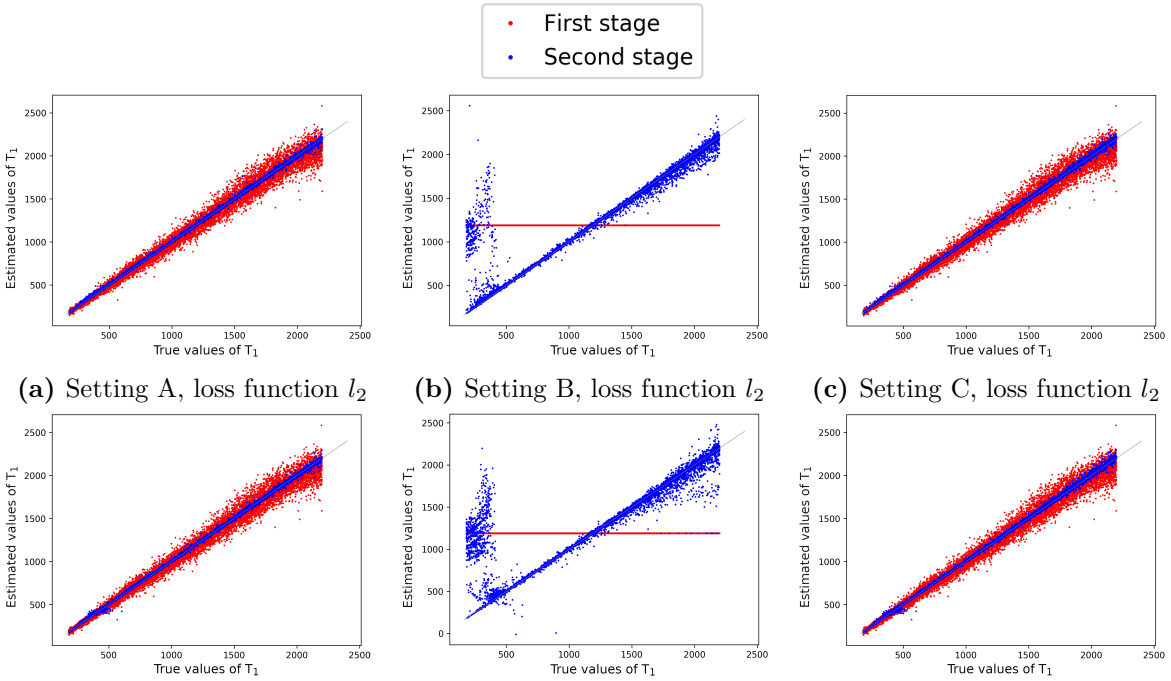

(a) Setting A, loss function l_2 **(b)** Setting B, loss function l_2 **(c)** Setting C, loss function l_2

(d) Setting A, loss function l_w **(e)** Setting B, loss function l_w **(f)** Setting C, loss function l_w

Figure 6.8: A comparison of the true and estimated values of T_1 was performed on the dataset of 10,000 synthetic samples of MOLLI. The first stage refers to the prediction of the neural network (NN), or the mean value of $T_1 = 1190.0$. The second stage refers to the result of numerical optimization (NO) of parameters T_1, T_2, M_0. Three settings of the NO stage initialization are evaluated:
Setting A) Initialization by the NN predictions: $T_1^{NN}, T_2^{NN}, M_0^{NN}$; $\alpha = \alpha^{NN}$
Setting B) Initialization by the mean values: $T_1 = 1190.0, T_2 = 160.0, M_0 = 0.4875$; $\alpha = 35.0$
Setting C) Combined initialization: $T_1^{NN}, T_2^{NN}, M_0^{NN}$; $\alpha = 35.0$
All variants were performed for quadratic loss function l_2 and weighted loss function l_w.

Sensitivity to noise in input data

The numerical optimization of T_1, T_2, M_0, initialized by the NN prediction, using l_2 and l_w loss functions were also evaluated on the data with added normally distributed noise with the standard deviations of $2 \cdot 10^{-3}, 5 \cdot 10^{-4}, 10^{-3}$. The mean relative error of the NN prediction of T_1 and the second stage estimation are shown in Table 6.4. The mean relative error in the T_1 estimated by the NN grows with the increasing standard deviation of the added noise. In the NO stage, the mean error is decreased in all cases. NO performed better when using the l_2 loss function.

Conclusion

When normally distributed noise is added to the input data:

- the accuracy of both the first ad second stage decreases
- the accuracy of the second stage estimation is still higher compared to the first stage

Table 6.4: Mean relative error (6.18) of the first- and second-stage T_1 estimation – $\bar{l}_{\mathrm{NN}}$ and $\bar{l}_{\mathrm{NO}}$ was evaluated on a synthetic dataset corrupted by normally distributed noise with four values of a standard deviation – $10^{-4}, 5 \cdot 10^{-4}$ and 10^{-3}. The NO stage was performed using loss functions l_2 and l_w.

		Types of added noise		
	Loss function	$N(0, 10^{-4})$	$N(0, 5 \cdot 10^{-4})$	$N(0, 10^{-3})$
$\bar{l}_{\mathrm{NN}}$	-	$4.66 \cdot 10^{-2}$	$5.75 \cdot 10^{-2}$	$7.79 \cdot 10^{-2}$
$\bar{l}_{\mathrm{NO}}$	l_2	$6.81 \cdot 10^{-3}$	$1.11 \cdot 10^{-2}$	$1.90 \cdot 10^{-2}$
	l_w	$6.99 \cdot 10^{-3}$	$1.25 \cdot 10^{-2}$	$2.22 \cdot 10^{-2}$

6.4.2 Phantom study

In the phantom study, the compared values of T_1 are denoted by: T_1^{pGT} for the pseudo-ground truth value obtained from IR-TSE sequence; $T_1^{scanner}$ for the scanner-provided estimate from the MOLLI sequence; T_1^{NN} for the first-stage estimate obtained from MOLLI measurement by NN; $T_1^{NN,NO(l_2)}$ second-stage estimate (NO) from MOLLI data initialized by NN and using loss function l_2; and $T_1^{NN,NO(l_w)}$ second-stage estimate (NO) initialized by NN using loss function l_w.

The problem (6.11) is solved by the l-BFGS method. The initial estimation of T_1, T_2, M_0 used in NO is based on the NN prediction in all cases. Two different values of flip angle are available – α^{NN} (predicted by NN) and the target value $\alpha = 35°$ (as set up in the MR sequence). The value α^{NN} is used in the NO stage if it does not differ from the expected value (in our case 35°) by more than 10°. Otherwise, the NN-predicted value is considered to be unrealistic and the value $\alpha = 35°$ is used instead.

Magnetic field 3 T

The mean T_1 value of the 8 phantoms was estimated in 5 slices measured by the MOLLI and IR-TSE sequence, respectively. The maps of T_1^{pGT}, $T_1^{scanner}$, T_1^{NN} and $T_1^{NN,NO(l_w)}$ in the middle slice are shown in Figure 6.9. The mean values and standard deviations of the estimated T_1, averaged over the 5 slices, are shown in Table 6.5. For the mean values and standard deviations evaluated in each slice, see Tables A4 and A5 in the Appendix.

The difference between the absolute values of percentage errors of $T_1^{NN,NO(l_w)}$ and $T_1^{scanner}$, with respect to T_1^{pGT}, was shown to be statistically significant (the hypothesis of equal means was rejected in Welch's t-test [84] with 95% confidence interval, p value = 0.036).

In the 8 phantoms, $T_1^{NN,NO(l_w)}$ estimations differs from the pseudo-ground truth T_1^{pGT} in average by 9.3%. $T_1^{NN,NO(l_w)}$ estimations are closer to T_1^{pGT} than $T_1^{scanner}$ in 7 out of the 8 phantoms. $T_1^{scanner}$ estimation is more accurate in Phantom 3, where its percentage error related to T_1^{pGT} is approximately 7.7%, while it is 9% in $T_1^{NN,NO(l_w)}$. Incorporating the NO stage increased the accuracy of the T_1^{NN} estimation in most phantoms (Phantom 1, 5, 6, 7, and 8).

The pseudo-ground truth T_1^{pGT} exhibits the lowest standard deviation. The NO stage decreased the standard deviation by more than 50% in all phantoms, except Phantom 1 and 8. The resulting standard deviations after the NO stage are still higher, compared to $T_1^{scanner}$.

$T_1^{NN,NO(l_w)}$ estimations are closer to T_1^{pGT} than $T_1^{NN,NO(l_2)}$ in all phantoms, except for Phantom 1 and 8.

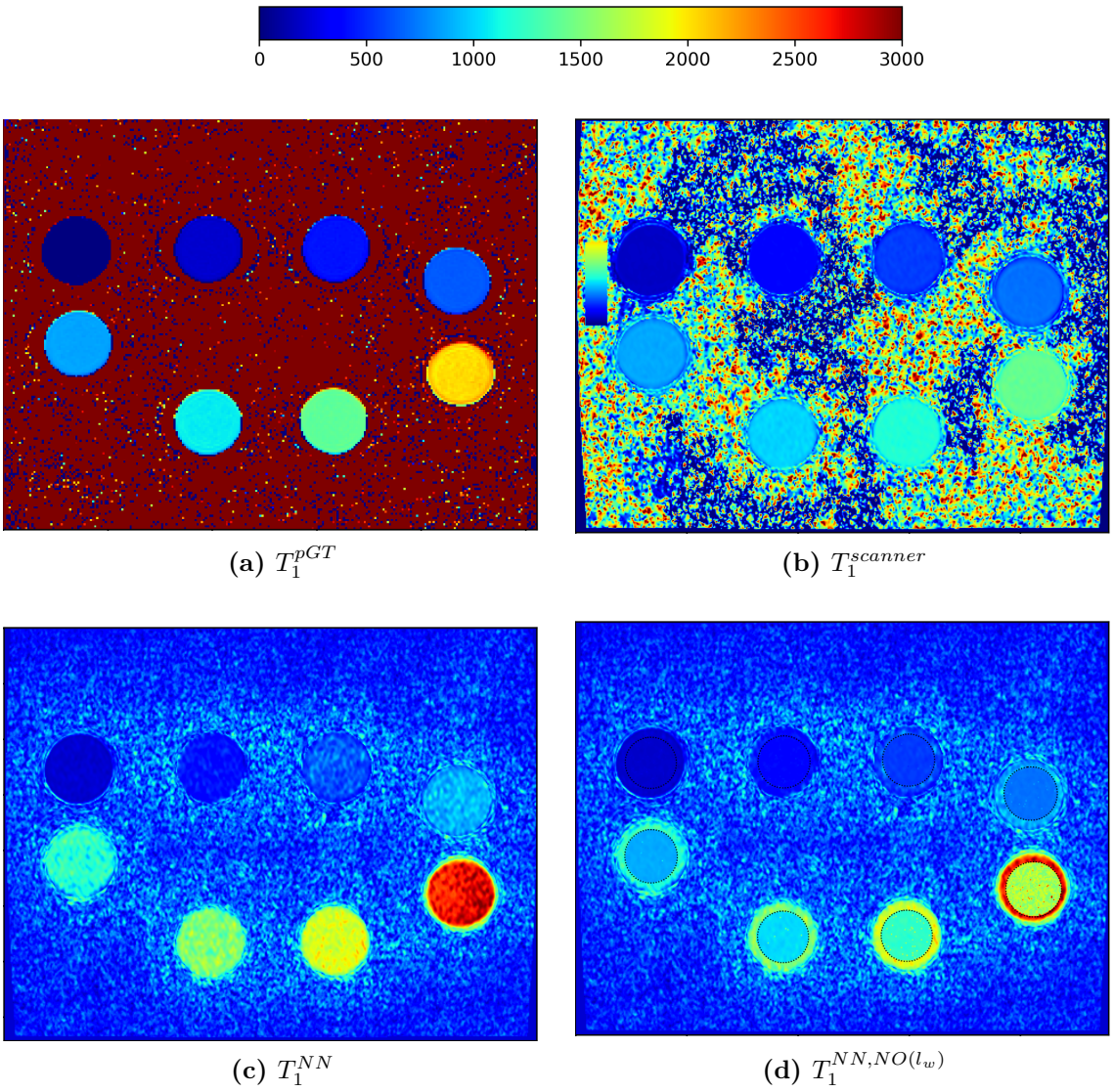

(a) T_1^{pGT} **(b)** $T_1^{scanner}$

(c) T_1^{NN} **(d)** $T_1^{NN,NO(l_w)}$

Figure 6.9: Maps of the pseudo-ground truth T_1^{pGT}, scanner estimation $T_1^{scanner}$, NN estimation T_1^{NN} and NO estimation $T_1^{NN,NO(l_w)}$. The NO stage was performed only for pixels in regions of interest marked with by a line.

Magnetic field 1.5T

The mean values and standard deviations of the estimated T_1, averaged over 6 slices, are shown in Table 6.6. For the mean values and standard deviations evaluated in each slice, see Tables A6 and A7 in the Appendix.

The difference between the absolute values of percentage errors of $T_1^{NN,NO(l_w)}$ and $T_1^{scanner}$, with respect to T_1^{pGT}, was shown not to be statistically significant (evaluated by Welch's t-test with 95% confidence interval, p value = 0.231).

The phantom experiment on data from 3T MRI scanner showed, that the proposed two-stage estimation method, using loss function l_w, is superior to the standard estimation method implemented on the scanner. In the experiment on 1.5T MRI scanner, the average percentage error of both estimations was significantly lower than in the experiment performed on 3T scanner.

Table 6.5: Parameters of T_1 estimations in phantoms (Ph. 1-8) acquired on 3T MRI scanner. The mean values and standard deviations of T_1 are averaged over the 5 slices measured by the MOLLI and IR-SE sequence, respectively. The percentage error is computed as a difference between the MOLLI-based T_1 estimations and the ground-truth value.

Mean values

	Ph. 1	Ph. 2	Ph. 3	Ph. 4	Ph. 5	Ph. 6	Ph. 7	Ph. 8
T_1^{pGT}	197.94	394.43	598.26	796.22	997.43	1194.15	1483.68	2065.34
$T_1^{scanner}$	177.62	371.70	552.33	665.15	856.48	1011.31	1185.88	1419.85
T_1^{NN}	226.56	407.87	647.35	857.66	1245.89	1473.56	1777.75	2596.16
$T_1^{NN,NO(l_2)}$	209.54	359.07	537.79	685.81	857.15	1008.37	1199.05	1872.09
$T_1^{NN,NO(l_w)}$	211.41	375.44	544.62	699.16	880.89	1037.96	1250.78	1761.88

Standard deviations

	Ph. 1	Ph. 2	Ph. 3	Ph. 4	Ph. 5	Ph. 6	Ph. 7	Ph. 8
T_1^{pGT}	2.40	4.76	6.54	6.45	7.78	11.05	13.70	25.85
$T_1^{scanner}$	13.69	8.54	12.55	45.52	30.01	15.09	18.86	28.31
T_1^{NN}	33.28	49.61	86.93	98.69	105.24	104.87	94.23	107.80
$T_1^{NN,NO(l_2)}$	45.11	11.09	13.36	51.61	46.74	45.45	55.16	695.21
$T_1^{NN,NO(l_w)}$	53.69	21.55	15.30	41.21	35.35	27.49	37.37	198.65

Percentage error with respect to T_1^{pGT}

	Ph. 1	Ph. 2	Ph. 3	Ph. 4	Ph. 5	Ph. 6	Ph. 7	Ph. 8
$T_1^{scanner}$	10.27	5.76	7.68	16.46	14.13	15.31	20.07	31.25
T_1^{NN}	-14.46	-3.41	-8.20	-7.72	-24.91	-23.40	-19.82	-25.70
$T_1^{NN,NO(l_2)}$	-5.86	8.96	10.11	13.87	14.06	15.56	19.18	9.36
$T_1^{NN,NO(l_w)}$	-6.80	4.81	8.97	12.19	11.68	13.08	15.70	14.69

6.4.3 *In vivo* data study

In the case of *in vivo* data, we only compare the scanner estimation from the MOLLI data $T_1^{scanner}$ and the results of the proposed method T_1^{NN} and $T_1^{NN,NO}$, since the long acquisition

Table 6.6: Parameters of T_1 estimations in phantoms (Ph. 1-8) acquired on 1.5T MRI scanner. The mean values and standard deviations of the T_1 are averaged over the 5 slices measured by the MOLLI and IR-SE sequence, respectively. The percentage error is computed as a difference between the MOLLI-based T_1 estimations and the ground-truth value.

Mean values

	Ph. 1	Ph. 2	Ph. 3	Ph. 4	Ph. 5	Ph. 6	Ph. 7	Ph. 8
T_1^{pGT}	161.88	316.23	479.32	640.99	796.26	953.85	1190.17	1637.50
$T_1^{scanner}$	151.29	307.09	465.15	610.12	758.90	893.08	1095.97	1449.50
T_1^{NN}	206.44	329.31	509.36	652.76	795.18	985.58	1206.09	1669.73
$T_1^{NN,NO(l_2)}$	166.16	298.50	445.55	591.57	743.83	883.76	1107.72	1562.37
$T_1^{NN,NO(l_w)}$	166.25	302.13	450.41	597.31	749.11	888.78	1114.46	1571.76

Standard deviations

	Ph. 1	Ph. 2	Ph. 3	Ph. 4	Ph. 5	Ph. 6	Ph. 7	Ph. 8
T_1^{pGT}	5.34	5.71	7.64	6.81	9.94	24.24	34.40	27.44
$T_1^{scanner}$	3.29	2.90	2.92	4.64	5.27	8.32	8.96	8.45
T_1^{NN}	4.49	13.56	21.29	25.65	29.86	53.68	73.58	53.25
$T_1^{NN,NO(l_2)}$	3.10	4.25	2.97	6.08	7.37	10.01	13.55	16.61
$T_1^{NN,NO(l_w)}$	3.27	3.77	3.39	6.02	7.68	10.88	16.02	17.65

Percentage error with respect to T_1^{pGT}

	Ph. 1	Ph. 2	Ph. 3	Ph. 4	Ph. 5	Ph. 6	Ph. 7	Ph. 8
$T_1^{scanner}$	6.54	2.89	2.95	4.80	4.69	6.37	7.91	11.45
T_1^{NN}	-27.53	-4.14	-6.27	-1.85	0.13	-3.32	-1.34	-2.00
$T_1^{NN,NO(l_2)}$	-2.65	5.60	7.04	7.71	6.58	7.35	6.93	4.58
$T_1^{NN,NO(l_w)}$	-2.70	4.46	6.03	6.81	5.92	6.82	6.36	4.01

time does not allow to acquire the IR-TSE sequence within a breath-hold. The weighted loss function l_w is used in the NO stage.

The problem (6.11) is solved by the l-BFGS method. Problem (6.16) with regularization term (6.17) is solved using the gradient descent method. The initial estimation of T_1, T_2, M_0

Table 6.7: T_1 estimation in the *in vivo* data acquired on 1.5T MRI scanner. Estimated pre-contrast T_1 relaxation time in blood and myocardium (in ms) in 12 patients.

	$T_1^{scanner}$		T_1^{NN}		$T_1^{NN,NO(l_w)}$	
	Blood	Myoc.	Blood	Myoc.	Blood	Myoc.
Subject 1	1679.62	1038.11	1560.92	1002.88	1706.98	1040.33
Subject 2	1434.97	1042.29	1795.10	1227.71	1495.21	1047.60
Subject 3	1641.16	1066.08	1985.48	1181.34	1733.55	1073.89
Subject 4	1509.47	1087.52	2011.17	1249.89	1651.59	1098.12
Subject 5	1633.87	998.07	1251.67	858.19	1718.34	1019.01
Subject 6	1521.37	1048.03	1642.95	1113.31	1542.41	1061.85
Subject 7	1460.51	1073.14	1741.55	1231.36	1551.21	1097.41
Subject 8	1669.61	1062.34	2169.43	1243.69	1808.20	1090.13
Subject 9	1552.87	1078.71	1833.85	1223.40	1586.91	1071.57
Subject 10	1436.81	1040.10	1771.03	1178.81	1429.03	1048.66
Subject 11	1539.98	1013.48	1557.20	1058.74	1565.40	1004.15
Subject 12	1668.04	1058.65	2103.05	1118.87	1761.15	1073.35

used in the numerical optimization is based on the NN prediction in all cases. The value α^{NN} is used in the NO stage if it does not differ from the expected value by more than 10 degrees. The expected $\alpha = 35°$ value is used otherwise.

Magnetic field 1.5T

The mean pre- and post-contrast T_1 in the myocardium and blood are shown in Tables 6.7 and 6.8, respectively.

The mean difference in the pre-contrast $T_1^{NN,NO(l_w)}$ and $T_1^{scanner}$ was 12 ms for the myocardium and 68 ms for the blood. In the post-contrast cases, where T_1 is shorter, the mean difference in $T_1^{NN,NO(l_w)}$ and $T_1^{scanner}$ remained similar – 16 ms for the myocardium and 45 ms for the blood. In the pre-contrast cases, the blood $T_1^{NN,NO(l_w)}$ was higher than $T_1^{scanner}$ in 11 subjects, and the myocardial T_1 was higher in 10 subjects. In the post-contrast cases, the blood $T_1^{NN,NO(l_w)}$ was higher than $T_1^{scanner}$ in all subjects. The post-contrast myocardial $T_1^{NN,NO(l_w)}$ was higher than $T_1^{scanner}$ in half of the subjects.

The effect of incorporating the spatial regularization term (6.17) in the NO stage is illustrated in Subject 4. The regularization term was included with the weight $\lambda = 5.0 \cdot 10^{-9}$. Four T_1 maps – $T_1^{scanner}$, T_1^{NN}, $T_1^{NN,NO(l_w)}$ and $T_1^{NN,NO(l_w,regul.)}$ – are displayed in Figure 6.10. The NN provides T_1 map with higher values than $T_1^{scanner}$ and significantly more noise. The

Table 6.8: T_1 estimation in the *in vivo* data acquired on 1.5T MRI scanner. Estimated post-contrast T_1 relaxation time in blood and myocardium (in ms) in 12 patients.

	$T_1^{scanner}$		T_1^{NN}		$T_1^{NN,NO(l_w)}$	
	Blood	Myoc.	Blood	Myoc.	Blood	Myoc.
Subject 1	234.03	391.45	249.94	435.60	243.63	386.03
Subject 2	201.92	323.64	236.10	357.49	218.32	361.60
Subject 3	274.18	407.91	308.53	482.67	277.90	401.58
Subject 4	232.51	404.67	283.03	291.59	235.39	371.91
Subject 5	184.53	349.29	195.96	370.01	195.88	373.85
Subject 6	280.50	423.67	310.86	419.82	310.33	408.47
Subject 7	274.14	423.38	329.19	559.35	371.08	426.26
Subject 8	278.61	441.69	303.55	472.47	315.70	429.55
Subject 9	220.66	356.88	268.08	424.10	228.02	388.65
Subject 10	213.21	340.61	238.30	430.78	219.83	365.63
Subject 11	225.25	396.61	296.04	448.60	264.27	404.24
Subject 12	251.93	419.41	280.24	467.90	291.63	418.55

map of $T_1^{NN,NO(l_w)}$ has lower values of blood T_1 and significantly less noise. In the map of $T_1^{NN,NO(l_w,regul.)}$, the noise is reduced to a level similar to $T_1^{scanner}$.

Magnetic field 3T

The mean pre- and post-contrast T_1 in the myocardium and blood of 3 subjects are shown in Tables 6.9 and 6.10, respectively.

In the pre-contrast cases, the values of $T_1^{NN,NO(l_w)}$ in blood and myocardium are higher than $T_1^{scanner}$. The average difference is 81ms in blood and 177ms in the myocardium. In the post-contracts cases, the values of $T_1^{scanner}$ are higher in the myocardium in all subjects, on average by 44ms. The difference in post-contrast blood T_1 is 2ms.

6.5 Discussion

In this chapter, we presented a parameter estimation method that combines machine learning and numerical optimization. This approach was demonstrated on the problem of estimating the T_1 relaxation time from the image data of the MRI MOLLI sequence.

The incorporation of the ML proved beneficial in both accelerating the numerical optimization and obtaining more accurate results, as shown in Table 6.3. This may be due to the fact that

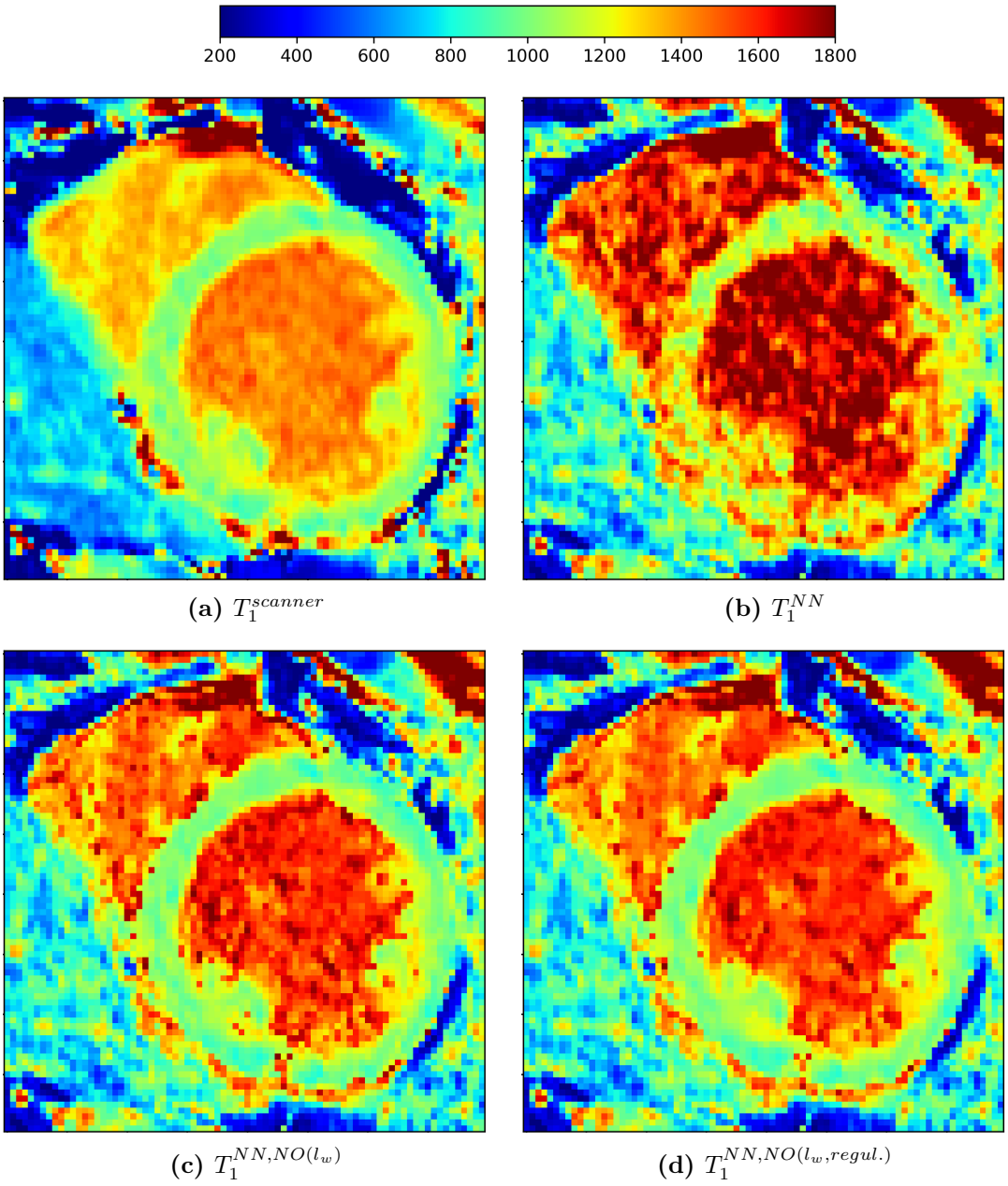

(a) $T_1^{scanner}$ **(b)** T_1^{NN}

(c) $T_1^{NN,NO(l_w)}$ **(d)** $T_1^{NN,NO(l_w,regul.)}$

Figure 6.10: The effect of spatial regularization on T_1 map in Subject 4. Figures (a) and (b) show the T_1 maps obtained by the scanner and NN, respectively. Figure (c) and (d) show the results of the NO stage, without regularization and with regularization term (6.17), respectively.

in some cases we avoid finding the local minimum, however, we note that the global minimum is still not guaranteed. The numerical optimization is needed as it considerably decreases the NN-initialized values of T_1 in both synthetic (Figure 6.7) and in vitro data. In the *in vivo* data, the NN tends to overestimate the T_1 values consistently. This behavior could be caused by the ill-posedness of the problem, as the training dataset may contain similar relaxation curves generated by different combinations of parameters. In the NO stage, the number of free parameters is significantly decreased by substituting the known parameters of the actual MOLLI sequence.

When applied to phantom data, better results were obtained using the loss function l_w. We

Table 6.9: T_1 estimation in the *in vivo* data acquired on 3T MRI scanner. Estimated pre-contrast T_1 relaxation time in blood and myocardium (in ms) in 3 patients.

	$T_1^{scanner}$		T_1^{NN}		$T_1^{NN,NO(l_w)}$	
	Blood	Myoc.	Blood	Myoc.	Blood	Myoc.
Subject 1	1748.97	1188.61	2302.02	1375.18	1817.35	1337.40
Subject 2	1783.30	1236.83	2331.35	1505.52	1859.02	1378.64
Subject 3	1891.98	1277.73	2746.37	1933.13	1993.10	1519.63

Table 6.10: T_1 estimation in the *in vivo* data acquired on 3T MRI scanner. Estimated post-contrast T_1 relaxation time in blood and myocardium (in ms) in 3 patients.

	$T_1^{scanner}$		T_1^{NN}		$T_1^{NN,NO(l_w)}$	
	Blood	Myoc.	Blood	Myoc.	Blood	Myoc.
Subject 1	257.92	481.77	268.24	365.89	253.05	427.34
Subject 2	363.17	600.68	417.79	732.71	365.61	592.55
Subject 3	311.90	512.25	320.85	420.71	320.18	441.99

may conclude, that assigning a higher weight to certain sampling points is suitable for data corrupted by noise and other artifacts, not considered in the simplified mathematical model. In the synthetic data experiment, where no such effects are present, using the weighted loss function was shown to be counterproductive and better accuracy was obtained using loss function l_2.

The synthetic data study also showed (Table 6.2) that the choice of the optimized parameters has a great influence on the accuracy of the resulting estimate of T_1. The most accurate results were obtained by optimizing T_1, T_2, M_0 in the second stage while keeping α fixed on the value predicted by the NN.

On the data from the 1.5T scanner, contrary to the 3T scanner, the difference in the accuracy of $T_1^{scanner}$ and $T_1^{NN,NO(l_w)}$ was shown not to be statistically significant. On both phantom datasets, the increase of percentage error of $T_1^{NN,NO(l_w)}$ with the increasing values of T_1 is not as significant as in $T_1^{scanner}$, which suggests more robust estimates throughout a wide interval of relaxation times.

The observed difference between the estimation using the 1.5T and 3T phantom measurements might be caused by a lower value of SNR that was observed in the MOLLI series measured on a 3T MRI scanner. The relative standard deviation of the measured MOLLI signal, averaged over all phantoms and all sampling points, was approximately twice as high in the case of the signal measured on the 3T scanner. The reason for a lower apparent SNR in 3T phantom measurements could be attributed to the RF interference resulting in uneven distribution of the flip angle throughout the scanning volume.

Furthermore, we observe that the relaxation time provided by the scanner is underestimated in all samples, i.e. in the T_1 range of approximately 190-2000 ms. We may argue that this trend would also hold for *in vivo* measurements with a similar range of values.

On the *in vivo* study, the estimates $T_1^{scanner}$, T_1^{NN} and $T_1^{NN,NO(l_w)}$ in blood and myocardium were compared on data from 1.5T and 3T MRI scanner. The ground-truth values are not available, but given our observation on the phantom study, we may assume our estimates would be higher than $T_1^{scanner}$. On the data from the 1.5T scanner, this was indeed observed in most cases for pre-contrast and for the blood pool post-contrast. On the data from the 3T scanner, this holds for most cases except for post-contrast myocardium. A similar trend was observed in the 3T phantom study, where $T_1^{NN,NO(l_w)}$ was lower than $T_1^{scanner}$ only in the phantom with the T_1 close to the post-contrast myocardium T_1.

We remark the training phase of NN used in the first stage of estimation only needs to be performed once for each type of imaging sequence. Therefore, imaging models with various signal-corrupting effects could be employed in this stage, without increasing the final estimation time. This could increase the robustness of the NN prediction.

Thanks to its variational formulation, the second stage may contain additional constraints, e.g. regularization terms that incorporate some a priori knowledge or additional requirements on the parameter maps. In the present work, we considered a term ensuring the spatial smoothness of the maps. When incorporating the spatial regularization term on the *in vivo* data, the noise in T_1 map was reduced, while all structures in the maps remained distinct.

6.5.1 Limitations

We acknowledge that more effects and MR artifacts could have been taken into account in the simulator. The simplicity of the current model (and the consequent modeling errors) may be the reason for some differences we observed between the synthetic and real data studies. We remark, that the pseudo-ground truth used for phantom validation, may also be affected by artifacts, especially for very short and very long T_1 relaxation times. The studied population is too small to drive complete conclusions about the superiority of the proposed method for the MOLLI data. However, even when using such a simplified model with synthetic data, a specially-designed phantom, and *in vivo* data, we were still able to demonstrate a concept, feasibility, and some advantages of the combined NN and numerical optimization two-stage parameter estimation.

6.6 Conclusions

Estimating parameters in complex biophysical models is a known problem. It often leads to computationally intensive calculations, which tend to fail if wrongly initialized. The initialization by NN predictions has the potential to substantially increase the efficiency of the subsequent optimization problem, particularly if the NN is trained beforehand and not for individual patients.

We remark that the method of *in silico* assessment could be directly employed in designing and evaluating new imaging sequences, e.g. different or a lower number of sampling points in the MOLLI, and possibly could be useful also in other types of exams (such as perfusion MRI). This has the potential to accelerate the exam while controlling the level of the expected error.

While demonstrating the proposed two-stage estimation method on an illustrative problem of estimating the T_1 relaxation time and creating the T_1 map, the method could be applicable for a number of other problems of coupling between magnetic resonance and modeling (including biomechanics or MR fingerprinting methods), particularly when estimating tissue and functional parameters of physiological and clinical interest.

Personal contribution

The author re-implemented the Bloch simulator created by Kateřina Fricková for her diploma thesis [25]. Several new parameters were added to the simulator to make it more aligned with the type of MOLLI sequence used to acquire the data. The author was also responsible for the design and implementation of the estimation method and the computations.

Conclusions and perspectives 7

Each chapter of this thesis contains the conclusions of the work presented. Within each chapter, the results, advantages, and limitations of specific methods were discussed.

In this chapter, we summarize the main achievements presented in this thesis and draw more general conclusions. Finally, potential topics for future research are suggested in each area.

Medical image registration

Accomplished work

In this work, two approaches to medical image registration were presented. In Chapter 2, an optical flow-based method was proposed to register myocardium in images from the MOLLI image series. The MOLLI image series exhibit varying image intensity, which needs to be taken into account in the registration. After the preparatory steps, comprising automatic segmentation of the myocardium and calculation of the signed distance function in both the source and target images, the displacement is determined for each pixel of the source image. Thus, the dimensions of the displacement field are directly related to the dimensions of the images.

This is the main difference between this optical flow approach and the second approach, referred to as mechanical, which was used in Chapters 3 and 4. In the mechanical approach, the registered object is discretized using an independent mesh, instead of a pixel grid of the image. The displacement is then calculated for each point of this mesh. The registered image is obtained by projecting the deformed mesh onto the image domain. While the number of pixels occupied by the object in the image may change significantly as the object deforms, the number of nodes of the mesh remains constant. Each node of the mesh can be tracked in time. This approach is therefore more suitable for the analysis of the deformation field. This is shown in Chapter 4, where the torsion of the left ventricle is determined based on the deformation field extracted from the MRI images series.

In the application described in Chapter 4, the deformed image is generated based on the deformed mesh and image intensity of the input image. In Chapter 3, an alternative approach is proposed, where the imaging model is used to generate the image intensity. The method is tested on synthetic tagged MRI images only.

Perspectives

In the future, the versions of the mechanical approach – the alternative one described in Chapter 3 and the original one used in Chapter 4 should be compared on real tagged MRI data.

In Chapters 3 and 4, only the images with constant intensity were considered. However, with a suitable imaging model, the mechanical approach could be applicable also to images with

varying intensity, such as the MOLLI images. The design of such an imaging model could be considered in future work.

When the optical flow-based method is applied to the distance function, the displacement field is determined only by the shape of the segmented objects. Therefore, no imaging model is needed to cope with the changes in intensity. This approach, however, requires performing segmentation in both the source and target image. The segmentation of the myocardium is done by detecting its inner and outer contours. In the current state, the parameters of the level-set method for edge detection need to be adjusted for each image. Therefore, a more robust segmentation method, possibly including some machine learning components, should be considered in the future.

Image deblurring

Accomplished work

In Chapter 5, the problem of image deblurring was formulated as a PDE constrained minimization problem. It was described, how the solution of the adjoint problem can be used in the minimization. Specifically, the direct computation of the derivative of the solution with respect to the optimized parameters can be avoided. The minimization problem is then solved iteratively by the gradient descent method with the primary and adjoint problem being solved in each iteration.

The use of the method was illustrated on several images with different levels of added blur. The original image was reconstructed in all cases. However, in the case of stronger blurring, some artifacts were present in the reconstructed image.

Perspectives

Comparison with the existing methods for image deblurring has not been performed at present. It can be expected that in general image deblurring the proposed method will not provide better results than the current state of the art machine learning-based methods. However, further analysis might show that the method is suitable for certain types of images.

Also, the presented adjoint formulation can be used to solve other inverse problems, such as finding the initial conditions of mean curvature flow or solving the inverse phase field equation.

Estimation of T_1 relaxation time

Accomplished work

In Chapter 6, the method for T_1 relaxation time estimation based on the MOLLI image series was presented. The proposed method utilized a mathematical model of the MOLLI sequence. The T_1 relaxation time was one of the parameters of the model. The model parameters were optimized to minimize the difference between the signal measured by MRI and generated using the model. The parameter optimization was performed in two stages – using the neural network and numerical optimization. The l-BFGS method and standard gradient descent were used in the second stage.

The method was validated on the synthetic, phantom, and *in vivo* data. The study on synthetic data was used to investigate the effect of the first stage of estimation on the accuracy of the second stage, to examine the sensitivity to noise, and to determine the most efficient setting of the second stage. In a phantom study, the results of the proposed method and the estimate from the MRI scanner were compared with the pseudo-truth values of T_1. The comparison with the MRI scanner estimate was also performed for the *in vivo* data.

Perspectives

Currently, there are two open problems. Firstly, in a phantom experiment on 3T MRI scanner data, the proposed method provided a more accurate estimate of T_1 than the MRI scanner. However, the average error was approximately twice as high as that of the 1.5T MRI scanner data. Secondly, for some phantoms, the second stage optimization reduced the variance of T_1 but also reduced the accuracy compared to the neural network. Both problems may be to some extent attributed to the fact that only local minima are found in the second stage. In the future, we should investigate whether using different optimization methods would eliminate the issues mentioned above. We could try more advanced variants of the gradient descent method, such as ADAM.

We could also consider incorporating additional regularization terms in the second stage. For example, terms that would contain prior knowledge about the expected values of the other tissue parameters. Further validation on MRI data could also lead to a better understanding of the limitations of our model and the adjustments that need to be made to make the simulations more realistic.

Appendices

Additional details on phantom and in-vivo study A

A.1 Parameters of the phantom measurements

The phantoms were imaged on a 3T MRI scanner (MAGNETOM Vida, Siemens Healthineers, Germany) and on a 1.5T MRI scanner (MAGNETOM Avanto fit, Siemens Healthineers, Germany) using head coil. The parameters on 3T system of the spoiled IR-TSE sequence were: turbo factor = 6; slice thickness = 4 mm; TE = 9 ms; TR = 8000 ms; BR = 256; RL = 31; PPF = 1; PPW = 100; FOV = 211 x 211 mm^2; spatial resolution = 0.82 mm (row and column directions); transversal slice orientation; TI = [100, 200, 400, 600, 800, 1000, 1400, 2000, 3510] ms. The parameters of the 5-3-3 MOLLI sequence were: slice thickness = 4 mm; flip angle $\alpha = 35°$, TE = 1.3 ms; TI = [104, 184, 264, 1004, 1084, 1164, 1904, 1984, 2064, 2804, 3704] ms; RR = 900 ms; BR = 240; RL = 36; PPF = 7/8; PPW = 77.5; FOV = 163 x 210 mm^2; spatial resolution = 0.44 mm (row and column directions); transversal slice orientation; L_c = 44; L_t = 99; RR = 900 ms.

The parameters on 1.5T system of the spoiled IR-TSE sequence were: turbo factor = 6; slice thickness = 4 mm; TE = 8.7 ms; TR = 800 ms; BR = 256; RL = 31; PPF = 1 ; PPW = 90.625; FOV = 191 x 211 mm^2; spatial resolution = 0.82 mm (row and column directions); transversal slice orientation; TI = [100, 200, 400, 600, 800, 1000, 1400, 2000, 3510] ms. The parameters of the 5-3-3 MOLLI sequence were: slice thickness = 8 mm; flip angle $\alpha = 35°$, TE = 1.13 ms; TI = [100, 180, 260, 1000, 1080, 1160, 1900, 1980, 2060, 2800, 3700] ms; RR = 900 ms; BR = 256; RL = 36, PPF = 1; PPW = 85.15625; FOV = 306 x 360 mm^2; spatial resolution = 1.4 mm (row and column directions); transversal slice orientation; L_c = 50; L_t = 113; RR = 900 ms.

A.2 Parameters of the in vivo measurements

The parameters of the MOLLI sequence on 1.5T system (12 patients) were: slice thickness = 8 mm; $\alpha = 35°$; TE = 1.13 ms; BR = 256; RL = 36; PPF = 7/8; PPW = 85.15625; FOV = 306 x 360 mm^2; spatial resolution = 1.4 mm (row and column directions); slice orientation: short axis of heart; L_c = 50; L_t = 113.

The parameters of the MOLLI sequence on 3T system (3 patients) were: slice thickness = 8 mm; $\alpha = 35°$; TE = 1.06 ms; BR = 256; RL = 36; PPF = 7/8; PPW = 78.125; FOV = 306 x 360 mm^2; spatial resolution = 0.703 mm (row and column directions); slice orientation: short axis of heart; L_c = 46; L_t = 106.

Table A1: Parameters of the in-vivo data acquired on the 1.5T MRI scanner – *Inversion times* (IT) and *RRs* [ms] of the pre- and post-contrast MOLLI measurements of the subject 1 - 6. The values of RR in the dataset vary from approximately 400 to 2000ms.

Subject 1												
pre	RR	1195	1230	1305	1200	1265	1305	1187	1277	1280	1220	1222
	IT	100	180	260	1295	1410	1565	2495	2675	2870	3682	4902
post	RR	1157	1107	1077	1192	1117	1085	1125	1110	1175	1157	1155
	IT	100	180	260	1258	1287	1338	2405	2423	2450	3623	4780
Subject 2												
pre	RR	845	785	785	887	782	782	785	787	867	855	847
	IT	100	180	260	945	965	1045	1747	1827	1833	2700	3555
post	RR	767	720	767	775	750	735	762	747	747	732	745
	IT	100	180	260	868	1027	1628	1643	1777	2405	3085	3153
Subject 3												
pre	RR	845	845	862	867	850	860	872	840	850	867	870
	IT	100	180	260	945	1025	1122	1813	1875	1982	2685	3553
post	RR	845	875	875	877	852	895	887	857	900	890	897
	IT	100	180	260	945	1055	1135	1822	1908	2033	2710	3600
Subject 4												
pre	RR	647	692	722	667	702	737	690	712	1437	680	672
	IT	100	180	260	747	872	982	1415	1575	1720	2105	2785
post	RR	627	407	630	647	630	610	650	647	605	645	645
	IT	100	180	260	728	890	935	1375	1520	2018	2025	2670
Subject 5												
pre	RR	527	1037	390	907	1102	832	1057	912	1012	852	962
	IT	108	188	268	1198	1325	1845	2428	2986	3485	3508	4498
post	RR	537	455	497	1010	972	1162	1050	1022	1177	1167	1127
	IT	108	188	268	1258	1305	1333	2268	2278	2495	3673	4840
Subject 6												
pre	RR	815	817	807	835	812	842	805	830	842	817	850
	IT	100	180	260	915	998	1750	1810	1875	2592	2707	3435
post	RR	1592	815	802	815	815	807	1605	815	835	817	817
	IT	100	180	260	995	1693	1810	1860	3305	3465	4928	5745

Table A2: Parameters of the in-vivo data acquired on the 1.5T MRI scanner – *Inversion times* (*IT*) and *RRs* [ms] of the pre- and post-contrast MOLLI measurements of the subjects 7 - 12. The values of RR in the dataset vary from approximately 400 to 2000ms.

Subject 7												
pre	*RR*	807	835	845	815	840	842	822	832	845	830	830
	IT	100	180	260	908	1015	1105	1723	1855	1947	2545	3375
post	*RR*	847	832	825	857	830	822	857	827	827	857	850
	IT	100	180	260	948	1013	1085	1805	1843	1907	2660	3518
Subject 8												
pre	*RR*	797	877	855	815	877	855	825	872	850	850	857
	IT	100	180	260	898	1057	1115	1713	1935	1970	2538	3388
post	*RR*	837	907	887	852	910	880	877	905	880	890	900
	IT	100	180	260	938	1088	1148	1790	1998	2028	2668	3558
Subject 9												
pre	*RR*	995	982	935	1025	967	932	1025	932	960	1020	1020
	IT	100	180	260	1095	1163	1195	2120	2127	2130	3145	4165
post	*RR*	1875	950	917	945	997	940	912	970	915	972	977
	IT	100	180	260	1130	1975	2075	2093	2972	3920	3942	4915
Subject 10												
pre	*RR*	745	622	565	615	745	555	600	732	722	545	715
	IT	100	180	260	802	845	1395	1417	1590	2323	2510	3045
post	*RR*	712	642	592	695	627	587	585	617	695	695	695
	IT	100	180	260	813	823	853	1440	1450	1508	2203	2898
Subject 11												
pre	*RR*	1117	1232	1195	1170	1217	1130	1137	1130	1227	2090	1217
	IT	100	180	260	1217	1412	1455	2387	2585	2630	3525	5615
post	*RR*	975	1022	1817	917	1002	992	1947	1785	855	1045	1047
	IT	100	180	260	1075	1203	2205	2957	2998	4783	5835	6880
Subject 12												
pre	*RR*	937	1012	1025	965	1020	1020	970	1025	1010	977	985
	IT	100	180	260	1038	1193	1285	2003	2213	2305	2973	3950
post	*RR*	950	1015	977	987	1015	955	990	927	997	995	997
	IT	100	180	260	1050	1195	1238	2038	2193	2210	3028	4023

Table A3: Parameters of the in-vivo data acquired on the 3T MRI scanner – *Inversion times* and *RRs* [ms] of the pre- and post-contrast MOLLI measurements of 3 the subject (denoted S.1 - S. 3). The values of RR in the dataset vary from approximately 400 to 600 ms.

Subject 1												
pre	*RR*	807	710	655	690	820	652	650	685	797	772	745
	IT	100	180	260	890	908	915	1568	1580	1728	2525	3298
post	*RR*	727	692	632	760	680	625	675	767	755	617	732
	IT	100	180	260	828	872	1532	1552	1588	2355	2782	3110
Subject 2												
pre	*RR*	930	855	845	920	850	847	855	892	855	875	850
	IT	100	180	260	1030	1035	1105	1885	1950	1952	2842	3717
post	*RR*	872	825	845	870	820	832	817	862	835	862	842
	IT	100	180	260	973	1005	1105	1825	1843	1938	2705	3568
Subject 3												
pre	*RR*	782	782	752	792	772	752	787	740	747	807	807
	IT	100	180	260	882	963	1013	1675	1735	1765	2462	3270
post	*RR*	897	765	747	882	752	742	865	845	740	740	832
	IT	100	180	260	997	1728	1748	1880	2745	3235	3238	3590

A.3 Additional results

Table A4: Mean values of the estimated T_1 in phantoms (Ph. 1-8) on 3T MRI. The mean values of the T_1 are evaluated in each of the 5 slices measured by the MOLLI and IR-SE sequence, respectively.

		Ph. 1	Ph. 2	Ph. 3	Ph. 4	Ph. 5	Ph. 6	Ph. 7	Ph. 8
T_1^{pGT}	Slice 1	199.63	396.21	601.83	803.06	1002.82	1195.04	1489.21	2098.31
	Slice 2	198.13	395.54	600.75	800.12	1005.04	1204.61	1498.57	2090.36
	Slice 3	198.28	394.18	599.57	796.05	997.00	1187.85	1480.76	2069.55
	Slice 4	197.06	394.43	597.26	793.52	995.09	1197.53	1483.43	2052.83
	Slice 5	196.62	391.77	591.91	788.36	987.23	1185.72	1466.43	2015.66
$T_1^{scanner}$	Slice	185.17	372.93	555.35	730.01	880.89	987.46	1151.54	1428.67
	Slice 2	186.92	373.31	554.27	717.02	881.85	999.83	1168.40	1418.27
	Slice 3	187.46	374.37	556.36	709.10	874.34	1000.25	1161.40	1415.42
	Slice 4	185.43	373.92	556.17	709.22	879.19	1003.46	1166.01	1423.75
	Slice 5	143.14	363.94	539.52	460.40	766.14	1065.57	1282.07	1413.15
T_1^{NN}	Slice 1	221.89	411.75	642.20	895.66	1357.66	1561.44	1858.42	2766.36
	Slice 2	210.56	413.85	654.71	881.10	1380.45	1538.59	1856.40	2648.32
	Slice 3	216.08	420.88	640.56	922.15	1203.59	1530.59	1846.07	2700.64
	Slice 4	211.20	416.40	639.45	872.35	1266.48	1544.41	1860.94	2770.22
	Slice 5	259.80	378.11	585.43	767.62	1060.34	1201.62	1496.78	2091.51
$T_1^{NN,NO(l_2)}$	Slice 1	197.53	358.21	537.55	712.31	866.72	979.16	1148.69	1988.09
	Slice 2	200.10	358.24	535.20	700.37	866.13	987.98	1161.52	1470.27
	Slice 3	202.21	358.71	536.91	691.77	858.27	988.44	1153.36	1784.14
	Slice 4	200.33	359.98	537.18	697.71	860.52	991.34	1158.49	2116.48
	Slice 5	247.50	360.20	542.11	626.87	834.13	1094.94	1373.20	2001.45
$T_1^{NN,NO(l_w)}$	Slice 1	199.84	374.87	545.76	721.34	892.38	1018.55	1215.86	1727.20
	Slice 2	200.40	372.98	541.82	717.18	890.22	1020.97	1227.76	1637.87
	Slice 3	202.10	375.34	544.19	708.99	880.57	1023.80	1215.98	1675.87
	Slice 4	200.95	375.58	543.39	711.37	880.95	1026.22	1222.99	1654.79
	Slice 5	253.75	378.44	547.93	636.94	860.34	1100.24	1371.30	2113.68

Table A5: Standard deviation of the estimated T_1 in phantoms (Ph. 1-8) on 3T MRI. The standard deviations of the T_1 estimations are evaluated in each of the 5 slices measured by the MOLLI and IR-SE sequence, respectively.

		Ph. 1	Ph. 2	Ph. 3	Ph. 4	Ph. 5	Ph. 6	Ph. 7	Ph. 8
T_1^{pGT}	Slice 1	2.30	4.82	6.79	6.76	6.89	10.13	12.88	25.45
	Slice 2	2.20	5.31	6.70	5.69	7.54	12.08	13.88	27.91
	Slice 3	2.43	4.48	6.76	6.57	9.12	10.22	13.17	25.06
	Slice 4	2.30	4.56	5.93	6.73	7.53	11.68	14.14	26.44
	Slice 5	2.79	4.64	6.52	6.50	7.85	11.13	14.43	24.40
$T_1^{scanner}$	Slice 1	4.50	8.45	13.69	7.69	9.92	14.90	18.58	14.63
	Slice 2	5.46	8.01	14.45	7.87	9.61	13.66	18.24	16.19
	Slice 3	5.30	8.93	12.06	7.99	10.05	14.64	19.15	15.75
	Slice 4	4.44	8.38	10.61	5.76	10.31	15.28	19.33	18.28
	Slice 5	48.74	8.95	11.94	198.29	110.13	16.97	19.01	76.69
T_1^{NN}	Slice 1	17.40	53.07	97.09	62.06	85.37	99.67	87.72	117.85
	Slice 2	23.64	56.02	99.06	84.64	78.62	121.79	77.05	84.52
	Slice 3	20.49	54.92	93.01	73.31	82.49	108.92	77.88	114.10
	Slice 4	18.17	50.23	89.61	66.23	79.00	108.71	100.29	107.97
	Slice 5	86.68	33.78	55.89	207.22	200.73	85.26	128.21	114.57
$T_1^{NN,NO(l_2)}$	Slice 1	7.08	11.24	14.39	19.20	32.47	47.64	58.43	1043.29
	Slice 2	7.13	10.07	15.05	18.84	35.25	47.95	55.43	332.07
	Slice 3	7.21	10.30	11.96	17.11	22.59	53.22	59.02	863.09
	Slice 4	7.02	12.33	11.90	20.29	15.07	50.35	58.68	1099.50
	Slice 5	197.13	11.49	13.49	182.63	128.30	28.09	44.25	138.08
$T_1^{NN,NO(l_w)}$	Slice 1	6.78	20.50	17.05	10.24	13.24	50.20	49.30	313.39
	Slice 2	7.12	20.41	16.59	11.47	11.83	20.40	33.17	127.27
	Slice 3	7.16	17.14	14.72	10.59	12.04	19.01	25.02	134.77
	Slice 4	6.49	17.07	14.30	9.65	13.67	18.94	32.88	190.76
	Slice 5	240.90	32.64	13.82	164.12	125.95	28.92	46.46	227.05

Table A6: Mean values of the estimated T_1 in phantoms (Ph. 1-8) on 1.5T MRI. The mean values of the T_1 are evaluated in each of the 6 slices measured by the MOLLI and IR-SE sequence, respectively.

		Ph. 1	Ph. 2	Ph. 3	Ph. 4	Ph. 5	Ph. 6	Ph. 7	Ph. 8
T_1^{pGT}	Slice 1	163.65	322.35	487.17	652.26	809.72	963.80	1201.39	1685.72
	Slice 2	162.92	317.34	481.89	645.09	799.94	955.51	1194.57	1654.17
	Slice 3	162.25	316.09	478.61	638.95	795.81	953.30	1191.13	1635.60
	Slice 4	161.10	314.72	476.28	637.22	791.87	949.36	1187.73	1622.59
	Slice 5	160.74	313.74	475.71	634.93	789.93	948.39	1180.92	1611.78
	Slice 6	160.61	313.17	476.24	637.47	790.30	952.74	1185.26	1615.12
$T_1^{scanner}$	Slice 1	151.38	308.52	467.43	607.04	758.89	895.23	1102.00	1431.11
	Slice 2	151.38	308.52	467.43	607.04	758.89	895.23	1102.53	1431.11
	Slice 3	150.76	307.89	465.88	612.24	763.39	896.00	1094.84	1464.67
	Slice 4	150.98	306.39	463.53	610.57	756.78	890.66	1093.33	1455.93
	Slice 5	150.98	306.39	463.53	611.55	756.78	890.66	1093.33	1455.93
	Slice 6	152.23	304.84	463.12	612.29	758.68	890.73	1089.81	1458.24
T_1^{NN}	Slice 1	210.00	329.40	511.53	645.48	797.31	1004.48	1213.58	1657.33
	Slice 2	210.00	329.40	511.53	645.48	797.31	1004.48	1209.00	1657.33
	Slice 3	204.01	325.54	508.05	647.53	814.29	981.90	1204.60	1662.64
	Slice 4	205.62	332.53	512.05	660.97	784.71	971.09	1216.04	1690.83
	Slice 5	205.62	332.53	512.05	661.03	784.71	971.09	1216.04	1690.83
	Slice 6	203.41	326.45	500.94	656.09	792.76	980.46	1177.27	1659.42
$T_1^{NN,NO(l_2)}$	Slice 1	165.10	302.82	448.54	597.62	752.43	889.98	1122.62	1605.79
	Slice 2	166.85	297.78	446.91	593.27	744.51	885.95	1113.33	1569.33
	Slice 3	167.64	297.95	445.60	590.59	746.08	886.10	1105.21	1560.84
	Slice 4	166.92	297.63	443.54	588.81	740.72	880.24	1102.77	1549.74
	Slice 5	166.03	297.01	445.82	588.47	738.75	881.42	1104.52	1536.42
	Slice 6	164.43	297.81	442.90	590.68	740.53	878.87	1097.89	1552.08
$T_1^{NN,NO(l_w)}$	Slice 1	165.85	306.48	454.47	603.12	756.47	893.07	1132.31	1616.44
	Slice 2	167.25	301.98	451.67	598.86	750.34	891.58	1118.60	1578.49
	Slice 3	168.03	301.58	450.91	596.29	752.78	890.44	1111.40	1568.29
	Slice 4	166.62	301.49	448.53	595.37	744.89	884.26	1109.20	1560.79
	Slice 5	165.47	300.36	449.62	594.20	744.19	888.40	1111.57	1546.95
	Slice 6	164.28	300.91	447.28	596.04	746.01	884.92	1103.65	1559.62

Table A7: Standard deviations of the estimated T_1 in phantoms (Ph. 1-8) on 1.5T MRI. The standard deviations of the T_1 are evaluated in each of the 6 slices measured by the MOLLI and IR-SE sequence, respectively.

		Ph. 1	Ph. 2	Ph. 3	Ph. 4	Ph. 5	Ph. 6	Ph. 7	Ph. 8
T_1^{pGT}	Slice 1	18.10	5.60	7.84	7.23	10.70	24.13	34.29	30.03
	Slice 2	3.03	5.79	7.90	7.25	9.28	26.04	37.83	26.55
	Slice 3	2.51	5.45	7.02	6.11	10.33	24.99	35.27	26.55
	Slice 4	2.89	5.89	7.73	6.53	9.50	24.17	33.31	27.23
	Slice 5	2.75	5.59	7.59	6.92	9.85	22.84	33.13	27.48
	Slice 6	2.73	5.92	7.79	6.82	10.00	23.28	32.58	26.81
$T_1^{scanner}$	Slice 1	3.47	2.53	3.00	6.64	5.27	7.52	7.61	10.75
	Slice 2	3.47	2.53	3.00	6.64	5.27	7.52	7.94	10.75
	Slice 3	4.03	3.57	3.05	3.56	6.00	7.99	10.16	8.21
	Slice 4	2.73	3.04	2.68	3.52	5.36	9.58	9.26	7.13
	Slice 5	2.73	3.04	2.68	3.96	5.36	9.58	9.26	7.13
	Slice 6	3.29	2.69	3.10	3.53	4.35	7.72	9.53	6.73
T_1^{NN}	Slice 1	4.15	15.16	21.88	20.57	31.53	57.93	64.48	55.93
	Slice 2	4.15	15.16	21.88	20.57	31.53	57.93	64.66	55.93
	Slice 3	5.38	12.71	22.10	26.99	33.32	64.97	80.30	54.28
	Slice 4	3.97	12.65	20.99	28.13	25.92	46.95	80.73	53.98
	Slice 5	3.97	12.65	20.99	28.77	25.92	46.95	80.73	53.98
	Slice 6	5.30	13.05	19.93	28.90	30.94	47.37	70.59	45.42
$T_1^{NN,NO(l_2)}$	Slice 1	6.03	5.00	3.74	12.71	15.90	10.86	15.19	35.76
	Slice 2	2.34	3.00	2.65	9.15	5.84	9.35	10.19	15.27
	Slice 3	3.57	3.79	2.85	3.50	6.61	9.27	15.21	13.66
	Slice 4	2.36	3.93	2.49	3.24	6.26	12.34	13.57	12.92
	Slice 5	2.03	3.81	3.21	3.76	5.10	9.55	13.83	10.91
	Slice 6	2.29	6.00	2.85	4.10	4.52	8.69	13.30	11.11
$T_1^{NN,NO(l_w)}$	Slice 1	5.74	4.64	3.82	11.22	14.93	11.49	17.78	39.19
	Slice 2	2.51	3.09	3.45	8.24	6.24	11.35	12.53	15.77
	Slice 3	4.46	3.58	3.19	4.46	7.82	9.24	17.03	13.55
	Slice 4	2.50	3.61	3.12	3.96	6.35	12.47	14.65	14.18
	Slice 5	2.18	3.50	3.38	4.40	5.56	11.02	17.81	11.07
	Slice 6	2.21	4.16	3.36	3.85	5.17	9.74	16.35	12.16

Bibliography

A

[1] Asner, L., Hadjicharalambous, M., Chabiniok, R., Peresutti, D., Sammut, E., Wong, J., Carr-White, G., Chowienczyk, P., Lee, J., King, A., et al. (2016). Estimation of passive and active properties in the human heart using 3D tagged MRI. *Biomechanics and modeling in mechanobiology*, 15(5):1121–1139.

[2] Aujol, J.-F. and Aubert, G. (2002). *Signed distance functions and viscosity solutions of discontinuous Hamilton-Jacobi Equations*. PhD thesis, INRIA.

[3] Axel, L. and Dougherty, L. (1989). MR imaging of motion with spatial modulation of magnetization. *Radiology*, 171(3):841–845.

B

[4] Benou, A., Veksler, R., Friedman, A., and Raviv, T. R. (2017). Ensemble of expert deep neural networks for spatio-temporal denoising of contrast-enhanced MRI sequences. *Medical image analysis*, 42:145–159.

[5] Bertoglio, C., Moireau, P., and Gerbeau, J.-F. (2012). Sequential parameter estimation for fluid–structure problems: Application to hemodynamics. *International Journal for Numerical Methods in Biomedical Engineering*, 28(4):434–455.

[6] Bittoun, J., Taquin, J., and Sauzade, M. (1984). A computer algorithm for the simulation of any nuclear magnetic resonance (NMR) imaging method. *Magnetic Resonance Imaging*, 2(2):113–120.

[7] Bloch, F. (1946). Nuclear induction. *Physical review*, 70(7-8):460.

[8] Bradley, A. M. (2021). PDE-constrained optimization and the adjoint method. `https://cs.stanford.edu/adjoint_tutorial.pdf`, 2019. Technical report.

[9] Burkhardt, B. E., Velasco Forte, M. N., Durairaj, S., Rafiq, I., Valverde, I., Tandon, A., Simpson, J., and Hussain, T. (2017). Timely pulmonary valve replacement may allow preservation of left ventricular circumferential strain in patients with tetralogy of Fallot. *Frontiers in Pediatrics*, 5:39.

C

[10] Caiazzo, A., Caforio, F., Montecinos, G., Muller, L. O., Blanco, P. J., and Toro, E. F. (2017). Assessment of reduced-order unscented Kalman filter for parameter identification in 1-dimensional blood flow models using experimental data. *International journal for numerical methods in biomedical engineering*, 33(8):e2843.

[11] Caselles, V., Kimmel, R., and Sapiro, G. (1997). Geodesic active contours. *International journal of computer vision*, 22(1):61–79.

[12] Castellanos, D. A., Škardová, K., Bhattaru, A., Berberoglu, E., Greil, G., Tandon, A., Dillenbeck, J., Burkhardt, B., Hussain, T., Genet, M., and Chabiniok, R. (2021). Left ventricular torsion obtained using equilibrated warping in patients with repaired tetralogy of Fallot. *Pediatric Cardiology*, 42(6):1275–1283.

[13] Chabiniok, R., Bhatia, K. K., King, A. P., Rueckert, D., and Smith, N. (2014). Manifold learning for cardiac modeling and estimation framework. In *International Workshop on Statistical Atlases and Computational Models of the Heart*, pages 284–294. Springer.

[14] Chabiniok, R., Moireau, P., Lesault, P.-F., Rahmouni, A., Deux, J.-F., and Chapelle, D. (2012). Estimation of tissue contractility from cardiac cine-MRI using a biomechanical heart model. *Biomechanics and modeling in mechanobiology*, 11(5):609–630.

[15] Chabiniok, R., Škardová, K., Galabov, R., Eichler, P., Gusseva, M., Janoušek, J., Fučík, R., Tintěra, J., Oberhuber, T., and Hussain, T. (2021). Translational cardiovascular modeling: Tetralogy of Fallot and modeling of diseases. In *Modeling Biomaterials*, pages 241–276. Springer.

[16] Clevert, D.-A., Unterthiner, T., and Hochreiter, S. (2015). Fast and accurate deep network learning by exponential linear units (elus). *arXiv preprint arXiv:1511.07289*.

[17] Cookson, A. N., Lee, J., Michler, C., Chabiniok, R., Hyde, E., Nordsletten, D., and Smith, N. (2014). A spatially-distributed computational model to quantify behaviour of contrast agents in MR perfusion imaging. *Medical image analysis*, 18(7):1200–1216.

[18] Cooper, M. A., Nguyen, T. D., Spincemaille, P., Prince, M. R., Weinsaft, J. W., and Wang, Y. (2012). Flip angle profile correction for T1 and T2 quantification with look-locker inversion recovery 2D steady-state free precession imaging. *Magnetic resonance in medicine*, 68(5):1579–1585.

D

[19] Deichmann, R. and Haase, A. (1992). Quantification of T1 values by SNAPSHOT-FLASH NMR imaging. *Journal of Magnetic Resonance (1969)*, 96(3):608–612.

[20] Deng, X. and Denney, T. S. (2004). Three-dimensional myocardial strain reconstruction from tagged MRI using a cylindrical b-spline model. *IEEE Transactions on Medical Imaging*, 23(7):861–867.

[21] Donati, F., Myerson, S., Bissell, M. M., Smith, N. P., Neubauer, S., Monaghan, M. J., Nordsletten, D. A., and Lamata, P. (2017). Beyond Bernoulli: improving the accuracy and precision of noninvasive estimation of peak pressure drops. *Circulation: Cardiovascular Imaging*, 10(1):e005207.

E

[22] Eichler, P., Galabov, R., Fučík, R., Škardová, K., Oberhuber, T., Pauš, P., Tintěra, J., and Chabiniok, R. (2022). Non-newtonian turbulent flow through aortic phantom: Experimental and computational study using magnetic resonance imaging and lattice Boltzmann method. *Under review in Computers & Mathematics with Applications*.

[23] Evans, L. C., Spruck, J., et al. (1991). Motion of level sets by mean curvature. *Journal of Differential Geometry*, 33(3):635–681.

F

[24] Fernandes, F. P., Manlhiot, C., Roche, S. L., Grosse-Wortmann, L., Slorach, C., McCrindle, B. W., Mertens, L., Kantor, P. F., and Friedberg, M. K. (2012). Impaired left ventricular myocardial mechanics and their relation to pulmonary regurgitation, right ventricular enlargement and exercise capacity in asymptomatic children after repair of tetralogy of Fallot. *Journal of the American Society of Echocardiography*, 25(5):494–503.

[25] Fricková, K. (2018). The simulation of bloch equations for quantitative evaluation of relaxation times in magnetic resonance. Master's thesis, Czech Technical University in Prague, Faculty of Nuclear Sciences and Physical Engineering.

[26] Fučík, R., Kovář, J., Škardová, K., Polívka, O., and Chabiniok, R. (2022). A lattice Boltzmann approach to mathematical modeling of myocardial perfusion. *Under review in International Journal for Numerical Methods in Biomedical Engineering*.

G

[27] Gai, N. D., Stehning, C., Nacif, M., and Bluemke, D. A. (2013). Modified look-locker T1 evaluation using Bloch simulations: human and phantom validation. *Magnetic resonance in medicine*, 69(2):329–336.

[28] Gelfand, I. M., Silverman, R. A., et al. (2000). *Calculus of variations*. Courier Corporation.

[29] Genet, M., Stoeck, C. T., Von Deuster, C., Lee, L. C., and Kozerke, S. (2018). Equilibrated warping: Finite element image registration with finite strain equilibrium gap regularization. *Medical image analysis*, 50:1–22.

[30] Geuzaine, C. and Remacle, J.-F. (2009). Gmsh: A 3-D finite element mesh generator with built-in pre-and post-processing facilities. *International journal for numerical methods in engineering*, 79(11):1309–1331.

[31] Geva, T., Sandweiss, B. M., Gauvreau, K., Lock, J. E., and Powell, A. J. (2004). Factors associated with impaired clinical status in long-term survivors of tetralogy of Fallot repair evaluated by magnetic resonance imaging. *Journal of the American College of Cardiology*, 43(6):1068–1074.

H

[32] Hadjicharalambous, M., Asner, L., Chabiniok, R., Sammut, E., Wong, J., Peressutti, D., Kerfoot, E., King, A., Lee, J., Razavi, R., et al. (2017). Non-invasive model-based assessment of passive left-ventricular myocardial stiffness in healthy subjects and in patients with non-ischemic dilated cardiomyopathy. *Annals of biomedical engineering*, 45(3):605–618.

[33] Hadjicharalambous, M., Chabiniok, R., Asner, L., Sammut, E., Wong, J., Carr-White, G., Lee, J., Razavi, R., Smith, N., and Nordsletten, D. (2015). Analysis of passive cardiac constitutive laws for parameter estimation using 3D tagged MRI. *Biomechanics and modeling in mechanobiology*, 14(4):807–828.

[34] Handlovičová, A., Mikula, K., and Sgallari, F. (2003). Semi-implicit complementary volume scheme for solving level set like equations in image processing and curve evolution. *Numerische Mathematik*, 93(4):675–695.

[35] Heinrich, M., Schnabel, J., Gleeson, F., Brady, M., and Jenkinson, M. (2010). Non-rigid multimodal medical image registration using optical flow and gradient orientation. *Medical Image Analysis and Understanding*, pages 141–145.

[36] Hinze, M., Pinnau, R., Ulbrich, M., and Ulbrich, S. (2008). *Optimization with PDE constraints*, volume 23. Springer Science & Business Media.

[37] Holzapfel, G. (2000). Nonlinear solid mechanics: A continuum approach for engineering. *Wiley, Chichester*, 547:27.

[38] Horn, B. K. and Schunck, B. G. (1981). Determining optical flow. *Artificial intelligence*, 17(1-3):185–203.

I

[39] Imperiale, A., Chapelle, D., and Moireau, P. (2021). Sequential data assimilation for mechanical systems with complex image data: application to tagged-MRI in cardiac mechanics. *Advanced Modeling and Simulation in Engineering Sciences*, 8(1):1–47.

J

[40] Jost, J. (2006). *Postmodern analysis*. Springer Science & Business Media.

K

[41] Kingma, D. P. and Ba, J. (2014). Adam: A method for stochastic optimization. *arXiv preprint arXiv:1412.6980*.

[42] Klement, V., Oberhuber, T., and Ševčovič, D. (2016). Application of the level-set model with constraints in image segmentation. *Numerical Mathematics: Theory, Methods and Applications*, 9(1):147–168.

[43] Koehler, S., Hussain, T., Blair, Z., Huffaker, T., Ritzmann, F., Tandon, A., Pickardt, T., Sarikouch, S., Latus, H., Greil, G., et al. (2021). Unsupervised domain adaptation from axial to short-axis multi-slice cardiac MR images by incorporating pretrained task networks. *IEEE Transactions on Medical Imaging*.

[44] Kreyszig, H. and Kreyszig, E. (2011). *Student solutions manual and study guide: for Kreyszig's Advanced engineering mathematics. 1. ODEs, linear algebra, vector calculus, fourier analysis, PDEs for chapters 1-12 of Advanced engineering mathematics*. Wiley.

L

[45] Lee, L. C. and Genet, M. (2019). Validation of equilibrated warping—image registration with mechanical regularization—on 3-D ultrasound images. In *International Conference on Functional Imaging and Modeling of the Heart*, pages 334–341. Springer.

[46] Lim, Y., Bliesener, Y., Narayanan, S., and Nayak, K. S. (2020). Deblurring for spiral real-time MRI using convolutional neural networks. *Magnetic resonance in medicine*, 84(6):3438–3452.

[47] Liu, D. C. and Nocedal, J. (1989). On the limited memory BFGS method for large scale optimization. *Mathematical programming*, 45(1):503–528.

[48] Logg, A. and Wells, G. N. (2010). Dolfin: Automated finite element computing. *ACM Transactions on Mathematical Software*, 37(2).

M

[49] Maes, F., Collignon, A., Vandermeulen, D., Marchal, G., and Suetens, P. (1997). Multimodality image registration by maximization of mutual information. *IEEE transactions on Medical Imaging*, 16(2):187–198.

[50] Makela, T., Clarysse, P., Sipila, O., Pauna, N., Pham, Q. C., Katila, T., and Magnin, I. E. (2002). A review of cardiac image registration methods. *IEEE Transactions on medical imaging*, 21(9):1011–1021.

[51] Mansi, T., Passerini, T., and Comaniciu, D. (2019). *Artificial intelligence for computational modeling of the heart*. Academic Press.

[52] Marquina, A. and Osher, S. (2000). Explicit algorithms for a new time dependent model based on level set motion for nonlinear deblurring and noise removal. *SIAM Journal on Scientific Computing*, 22(2):387–405.

[53] Messroghli, D. R., Radjenovic, A., Kozerke, S., Higgins, D. M., Sivananthan, M. U., and Ridgway, J. P. (2004). Modified Look-Locker inversion recovery (MOLLI) for high-resolution T1 mapping of the heart. *Magnetic Resonance in Medicine*, 52(1):141–146.

N

[54] Nakatani, S. (2011). Left ventricular rotation and twist: why should we learn? *Journal of cardiovascular ultrasound*, 19(1):1–6.

O

[55] Oktay, O., Ferrante, E., Kamnitsas, K., Heinrich, M., Bai, W., Caballero, J., Cook, S. A., De Marvao, A., Dawes, T., O'Regan, D. P., et al. (2017). Anatomically constrained neural networks (ACNNs): Application to cardiac image enhancement and segmentation. *IEEE transactions on medical imaging*, 37(2):384–395.

[56] Oliveira, F. P. and Tavares, J. M. R. (2014). Medical image registration: a review. *Computer methods in biomechanics and biomedical engineering*, 17(2):73–93.

[57] Osher, S. and Sethian, J. A. (1988). Fronts propagating with curvature-dependent speed: algorithms based on hamilton-jacobi formulations. *Journal of computational physics*, 79(1):12–49.

P

[58] Paul, J. and Raveendran, S. (2015). *Understanding Phase Contrast MR Angiography: A Practical Approach with MATLAB examples.*

[59] Peng, D., Merriman, B., Osher, S., Zhao, H., and Kang, M. (1999). A PDE-based fast local level set method. *Journal of computational physics*, 155(2):410–438.

[60] Pereira, S., Pinto, A., Alves, V., and Silva, C. A. (2016). Brain tumor segmentation using convolutional neural networks in MRI images. *IEEE transactions on medical imaging*, 35(5):1240–1251.

[61] Perona, P. and Malik, J. (1990). Scale-space and edge detection using anisotropic diffusion. *IEEE Transactions on pattern analysis and machine intelligence*, 12(7):629–639.

[62] Peyré, G., Péchaud, M., Keriven, R., Cohen, L. D., et al. (2010). Geodesic methods in computer vision and graphics. *Foundations and Trends in Computer Graphics and Vision*, 5(3–4):197–397.

[63] Precup, R. (2013). *Methods in nonlinear integral equations.* Springer Science & Business Media.

Q

[64] Qin, C., Bai, W., Schlemper, J., Petersen, S. E., Piechnik, S. K., Neubauer, S., and Rueckert, D. (2018). Joint learning of motion estimation and segmentation for cardiac MR image sequences. In *International Conference on Medical Image Computing and Computer-Assisted Intervention*, pages 472–480. Springer.

R

[65] Rueckert, D., Sonoda, L. I., Hayes, C., Hill, D. L., Leach, M. O., and Hawkes, D. J. (1999). Nonrigid registration using free-form deformations: application to breast MR images. *IEEE transactions on medical imaging*, 18(8):712–721.

S

[66] Satish, P., Srikantaswamy, M., and Ramaswamy, N. K. (2020). A comprehensive review of blind deconvolution techniques for image deblurring. *Traitement du Signal*, 37(3).

[67] Schlemper, J., Caballero, J., Hajnal, J. V., Price, A. N., and Rueckert, D. (2017). A deep cascade of convolutional neural networks for dynamic MR image reconstruction. *IEEE transactions on Medical Imaging*, 37(2):491–503.

[68] Schroeder, W., Martin, K. M., and Lorensen, W. E. (1998). *The visualization toolkit an object-oriented approach to 3D graphics*. Prentice-Hall, Inc.

[69] Sermesant, M., Delingette, H., Cochet, H., Jaïs, P., and Ayache, N. (2021). Applications of artificial intelligence in cardiovascular imaging. *Nature Reviews Cardiology*, pages 1–10.

[70] Sethian, J. A. (1996). *Level Set Methods: Evolving Interfaces in Geometry, Fluid Mechanics, Computer Vision, and Materials Scie*. Cambridge university press.

[71] Sethian, J. A. et al. (1990). Numerical algorithms for propagating interfaces: Hamilton-jacobi equations and conservation laws. *Journal of differential geometry*, 31(1):131–161.

[72] Shao, J., Ghodrati, V., Nguyen, K.-L., and Hu, P. (2020). Fast and accurate calculation of myocardial T1 and T2 values using deep learning Bloch equation simulations (DeepBLESS). *Magnetic resonance in medicine*, 84(5):2831–2845.

[73] Shao, J., Liu, D., Sung, K., Nguyen, K.-L., and Hu, P. (2017). Accuracy, precision, and reproducibility of myocardial T1 mapping: A comparison of four T1 estimation algorithms for modified look-locker inversion recovery (MOLLI). *Magnetic resonance in medicine*, 78(5):1746–1756.

[74] Shao, J., Nguyen, K.-L., Natsuaki, Y., Spottiswoode, B., and Hu, P. (2015). Instantaneous signal loss simulation (InSiL): an improved algorithm for myocardial T1 mapping using the MOLLI sequence. *Journal of Magnetic Resonance Imaging*, 41(3):721–729.

[75] Shao, J., Rapacchi, S., Nguyen, K.-L., and Hu, P. (2016). Myocardial T1 mapping at 3.0 Tesla using an inversion recovery spoiled gradient echo readout and Bloch equation simulation with slice profile correction (BLESSPC) T1 estimation algorithm. *Journal of Magnetic Resonance Imaging*, 43(2):414–425.

[76] Simard, P. Y., Steinkraus, D., Platt, J. C., et al. (2003). Best practices for convolutional neural networks applied to visual document analysis. In *The International Conference on Document Analysis and Recognition*, volume 3.

[77] Škardová, K., Oberhuber, T., Tintěra, J., and Chabiniok, R. (2021). Signed-distance function based non-rigid registration of image series with varying image intensity. *Discrete & Continuous Dynamical Systems - S*, 14(3):1145–1160.

[78] Škardová, K., Rambausek, M., Chabiniok, R., and Genet, M. (2019). Mechanical and imaging models-based image registration. In *ECCOMAS Thematic Conference on Computational Vision and Medical Image Processing*, pages 77–85. Springer.

[79] Sussman, M. S., Yang, I. Y., Fok, K.-H., and Wintersperger, B. J. (2016). Inversion group (IG) fitting: A new T1 mapping method for modified look-locker inversion recovery (MOLLI) that allows arbitrary inversion groupings and rest periods (including no rest period). *Magnetic resonance in medicine*, 75(6):2332–2340.

T

[80] Tobon-Gomez, C., De Craene, M., Mcleod, K., Tautz, L., Shi, W., Hennemuth, A., Prakosa, A., Wang, H., Carr-White, G., Kapetanakis, S., et al. (2013). Benchmarking framework for myocardial tracking and deformation algorithms: An open access database. *Medical image analysis*, 17(6):632–648.

V

[81] van der Hulst, A. E., Delgado, V., Holman, E. R., Kroft, L. J., de Roos, A., Hazekamp, M. G., Blom, N. A., Bax, J. J., and Roest, A. A. (2010). Relation of left ventricular twist and global strain with right ventricular dysfunction in patients after operative "correction" of tetralogy of Fallot. *The American journal of cardiology*, 106(5):723–729.

W

[82] Wang, J., Mao, W., Qiu, M., Smith, M. B., and Constable, R. T. (2006). Factors influencing flip angle mapping in MRI: RF pulse shape, slice-select gradients, off-resonance excitation, and b0 inhomogeneities. *Magnetic Resonance in Medicine: An Official Journal of the International Society for Magnetic Resonance in Medicine*, 56(2):463–468.

[83] Wang, V. Y., Lam, H., Ennis, D. B., Cowan, B. R., Young, A. A., and Nash, M. P. (2009). Modelling passive diastolic mechanics with quantitative MRI of cardiac structure and function. *Medical image analysis*, 13(5):773–784.

[84] Welch, B. L. (1947). The generalization of 'STUDENT'S' problem when several different population varlances are involved. *Biometrika*, 34(1-2):28–35.

X

[85] Xanthis, C. G., Bidhult, S., Kantasis, G., Heiberg, E., Arheden, H., and Aletras, A. H. (2015). Parallel simulations for QUAntifying RElaxation magnetic resonance constants (SQUAREMR): an example towards accurate MOLLI T1 measurements. *Journal of Cardiovascular Magnetic Resonance*, 17(1):1–15.

Z

[86] Zeng, D. Y., Shaikh, J., Holmes, S., Brunsing, R. L., Pauly, J. M., Nishimura, D. G., Vasanawala, S. S., and Cheng, J. Y. (2019). Deep residual network for off-resonance artifact correction with application to pediatric body MRA with 3D cones. *Magnetic resonance in medicine*, 82(4):1398–1411.